

ИНСТИТУТ ЗА ФИЗИКУ			
ПРИМЉЕНО: 31-10-2024			
Рад.јед.	б р о ј	Арх.шифра	Прилог
0801-	1972/1		

Научном већу Института за физику у Београду

Адреса: Прегревица 118, 11080 Београд, Србија

Предмет: Молба за покретање поступка за стицање звања **НАУЧНИ САРАДНИК**

С обзиром да испуњавам све критеријуме прописане од стране Министарства за науку, технолошки развој и иновације за стицање звања **НАУЧНИ САРАДНИК**, молим Научно веће Института за физику у Београду да покрене поступак за мој избор у звање.

У прилогу достављам:

1. Мишљење руководиоца групе са предлогом чланова комисије за избор у звање,
2. Стручну биографију,
3. Преглед научне активности,
4. Елементе за квалитативну анализу научног доприноса,
5. Елементе за квантитативну анализу научног доприноса,
6. Списак објављених радова и њихове копије,
7. Податке о цитираности радова (Scopus),
8. Решење о претходном избору у звање,
9. Потврду о одбрањеној докторској дисертацији.

У Београду,

30.10.2024


др Иван Трапарић

ИНСТИТУТ ЗА ФИЗИКУ

ПРИМЉЕНО: 31-10-2024			
Рад.јед.	б р о ј	Арх.шифра	Прилог
0801-1972/2			

Мишљење руководиоца групе са предлогом чланова комисије за избор у звање научни сарадник – кандидат др Иван Трапарић

Др Иван Трапарић, рођен 14.9.1996. године у Требињу је 18.10.2024. године успешно одбранио своју докторску дисертацију под насловом „Примена машинског учења и вештачке интелигенције у спектроскопији плазме“ на Физичком факултету Универзитета у Београду. Ментори докторске дисертације су били доц. др Маријана Гавриловић Божовић са Факултета инжењерских наука и др Миливоје Ивковић, научни саветник Института за физику у Београду.


Поред тога, др Иван Трапарић је активни учесник пројекта NOVA2LIBS4fusion који се финансира у оквиру позива ИДЕЈЕ Фонда за науку Републике Србије. У Институту за физику је запослен од априла 2021. године прво у звању истраживач приправник, а од новембра 2023. године у звању истраживач сарадник. Током израде докторске дисертације, кандидат је објавио више научних радова у високо ранжираним иностраним научним часописима. Из приложеног материјала, кандидат др Иван Трапарић испуњава све услове предвиђене Законом о науци и истраживањима и Правилником о стицању истраживачких и научних звања Министарства науке, технолошког развоја и иновација Републике Србије за избор у звање научни сарадник, те предлажем Научном већу Института за физику у Београду да покрене избор др Ивана Трапарића у поменуто звање.

За чланове комисије предлажем:

1. др Миливоје Ивковић, научни саветник Института за физику у Београду
2. др Биљана Станков, научни сарадник Института за физику у Београду
3. др Мирослав Кузмановић, редовни професор Факултета за физичку хемију Универзитета у Београду

У Београду,

30.10.2024.



др Миливоје Ивковић

Руководилац лабораторије за спектроскопију плазме и ласере

Стручна биографија – Иван Трапарић

Иван Трапарић рођен је у Требињу, БиХ, 14.9.1996. године где је завршио основну и средњу школу. На основне студије Физичког факултета Универзитета у Београду уписује се 2015. године на смер *Примењена и компјутерска физика*. Основне студије завршава у редовном року 2019. године са средњом просечном оценом 9.43. Исте године уписује мастер студије на Физичком факултету Универзитета у Београду на смеру *Теоријска и експериментална физика*. Мастер студије је завршио са средњом просечном оценом 10, а мастер рад одбранио са оценом 10. Мастер рад под насловом „Вакуум ултраљубичаста спектроскопија Лајманове серије јонизованог атома хелијума“ је урађен у Лабораторији за спектроскопију плазме и ласере на Институту за физику у Београду, под руководством др Миливоја Ивковића.

На Институту за физику у Београду је запослен од априла 2021. као студент докторских студија у звању истраживач приправник. Током докторских студија, бавио се или се бави вакуум ултраљубичастом спектроскопијом електричних гасних пражњења, применом машинског учења и вештачке интелигенције у оптичкој емисионој спектроскопији плазме и унапређивањем метода и побољшања граница детекције појединих елемената у спектроскопији ласерски индукованих плазми. У последње време, бави се и применом вештачке интелигенције у вакуум ултраљубичастој спектроскопији фузионих плазми. У току основних студија је учествовао на две летње школе из области физике фузионих плазми. Прва летња школа организована је у Београду, у организацији *Фузоине образовне мреже (ФОМ)*. Током ове летње школе, имао је прилику да путем интернета присуствује експериментима на токамаку GOLEM у Прагу, а тема истраживања била је експериментална физика *runaway* електрона. Друга летња школа је била на Институту за физику плазме Чешке академије наука и уметности у Прагу, где су рађени експерименти на токамаку COMPASS. Овде је имао прилику да две недеље учествује у истраживању експерименталне групе која се бави нестабилностима на ивици плазме.

До сада је објавио шест радова у часописима са СЦИ листе, од којих су три објављена у врхунском међународном часопису (категорија M21) а остала три у међународном часопису категорије M23. Свој досадашњи рад презентовао је на шест међународних конференција (SPIG 2020, SPIG 2022, SPIG 2024, XIV SCSSA, SLSP 6 и ICSLS 2024). На међународној конференцији *14th Serbian Conference on Spectral Line Shapes in Astrophysics* одржаној у Бајној Башти у јуну ове године је одржао кратко позивно предавање. Учесник је пројекта NOVA2LIBS4fusion који се финансира у оквиру програма ИДЕЈЕ Фонда за науку Републике Србије. Према индексној бази Scopus његови радови цитирани су 7 пута а Хиршов фактор износи $h = 2$.

Преглед научне активности

Научна активност др Ивана Трапарића је првенствено у области дијагностике плазме методом оптичке емисионе и вакуум ултраљубичасте (ВУВ) спектроскопије, применама машинског учења у спектроскопији плазме, те методама унапређена аналитичких перформанси спектроскопије ласерски индукованог пробоја.

Сходно овоме, рад кандидата се може класификовати у следеће категорије:

1. Примена машинског учења у спектроскопији плазме
2. Истраживања у области спектроскопије ласерски индукованог пробоја

Кандидат је до сада објавио 6 научних радова, а од тога 2 рада од претходног избора у звање (новембар 2023. године) до данас.

Примена машинског учења у спектроскопији плазме

Примена машинског учења присутна је у свим областима науке генерално, па је тако своју примену нашло и у спектроскопији плазме. Један од историјски најстаријих области којима се Лабораторија за спектроскопију плазме и ласере бави јесте одређивање густине електрона коришћењем различитих особина спектралних линија које испољавају Штарков ефекат (полуширина линије, растојање између дозвољених и забрањених компоненти итд.). У том смислу, у оквиру рада на докторској дисертацији кандидат је развио модел заснован на машинском учењу чији је циљ био предвиђање полуширине емитоване спектралне линије за улазне параметре плазме: густина електрона, температура електрона, емитер, наелектрисање емитера, ефективни јонизациони потенцијал горњег нивоа, енергије горњег и доњег енергетског нивоа, главни и орбитални квантни бројеви оба нивоа, укупни угаони момент оба нивоа и енергија јонизације емитера. Поред могућности брзе процене Штаркове полуширине, испитане су и регуларности Штарковог ефекта дуж спектралне серије неутралног атома литијума. Резултати ових истраживања објављени су у два рада у иностраним научним часописима:

1. Stark spectral line broadening modeling by machine learning algorithms

Аутори: I. Tapalaga, I. Traparić, N. Trklja Boca, J. Purić, I. P. Dojčinović

Часопис: *Neural Computing and Applications* **34**, 6349-6358, 2022, **M21, IF 6.0**

DOI: 10.1007/s00521-021-06763-4

2. New perspectives in the analysis of Stark width regularities and systematic trends

Аутори: Z. Majlinger, I Traparić

Часопис: *Contrib. Astron. Obs. Skalnaté Pleso* **53**, 58 – 71, 2023, **M23, IF 0.3**

DOI: 10.31577/caosp.2023.53.3.58

Машинско учење је такође примењено и у класификацији звезда на основу снимљеног спектра у видљивој области и ови резултати су објављени у раду

1. **The usage of perceptron, feed and deep feed forward artificial neural networks on the spectroscopy data: astrophysical & fusion plasmas**

Аутори: NM Sakan, I Traparic, VA Sreckovic, M Ivkovic

Часопис: *Contrib. Astron. Obs. Skalnaté Pleso* **52**, 97 – 104, 2022, **M23, IF 0.4**

DOI: 10.31577/caosp.2022.52.3.97

Потом, урађено је испитивање могућности обучавања модела машинског учења на постојећој бази снимљених спектра стандардних узорака нерђајућих челика у циљу квантитативне анализе у спектроскопији ласерски индукованог пробоја. Наиме, како би се избегло трошење времена на прављење базе за обучавање, са истом апаратуром и при истим условима снимљени су спектри тест узорака и резултати су објављени у раду:

1. Determination of austenitic steel alloys composition using laser-induced breakdown spectroscopy (LIBS) and machine learning algorithms

Аутори: I Traparic, M Ivkovic

Часопис: *The European Physical Journal D* **77**, 30, 2023, **M23, IF 1.6**

DOI: 10.1140/epjd/s10053-023-00608-6

Конечно, машинско учење примењено је у сврху генерације и моделовања спектра волфрама емитованог у области ВУВ спектра у опсегу таласних дужина од 4 до 7 nm. У овом делу спектра, колизионо радијативни модели развијени раније нису у могућности да Спектри су снимљени у хелиотрону ЛХД (енг. *Large Helical Device*) у Јапану. Рад је послат у часопис и тренутно је у процесу рецензије.

Истраживања у области спектроскопије ласерски индукованог пробоја

У току реализације пројекта ИДЕЈЕ кандидат је учествовао у унапређењу постојећих метода спектроскопије ласерски индукованог пробоја (енг. *LIBS – Laser Induced Breakdown Spectroscopy*) у циљу анализе и карактеризације првог зида фузионог реактора. С тим у вези, прво је испитана граница детекције бабра у легури волфрам – бакар која представља идеалан прелазни материјал са чистог волфрама на неку од легура као што је легура CuCrZr од које се праве цеви за хлађење првог зида реактора. Прелазни материјал је потребан јер због изложености првог зида јаким топлотним флуксевима долази до напрснућа материјала првог зида чиме се угрожавају саме цеви за хлађење и безбедан рад фузионог реактора. Због тога, ЛИБС техника је искоришћена за демонстрацију одређивања процента бабра у узорку као и количине аблираног материјала. Резултати су објављени у раду:

1. LIBS depth-profile analysis of W/Cu functionally graded material

Аутори: M Ivkovic, J Savovic, Biljana D Stankov, M Kuzmanovic, I Traparic

Часопис: *Spectrochimica Acta Part B: Atomic Spectroscopy* **213**, 106874, 2024, **M21, IF 3.2**

DOI: 10.1016/j.sab.2024.106874

Други проблем који је размотрен у овом пројекту јесу технике раздвајања Балмер алфа линија водоникових изотопа. Овај проблем је веома актуелан јер се развија метода процене концентрације трицијума у првом зиду реактора *in-situ* методом, која би дала брзу, једноставну и поуздану процену концентрације трицијума у првом зиду нуклеарног реактора. Метода која је примењена је демонстрирана на графитној мети на коју је накапана одређена концентрација тешке воде. Мета је изложена ласерском импулсу ТЕА СО₂ ласера различитих енергија, а снимање спектра је вршено у контролисаној атмосфери аргона и хелијума коришћењем спектрометра високе резолуције и iCCD камере. Добијени резултати приказани су у раду:

1. Resolving studies of Balmer alpha lines relevant to the LIBS analysis of hydrogen isotope retention

Аутори: I Traparic, D Rankovic, BD Stankov, J Savovic, M Kuzmanovic, M Ivkovic

Часопис: *Spectrochimica Acta Part B: Atomic Spectroscopy* **221**, 107050, 2024, **M21, IF 3.2**

DOI: 10.1016/j.sab.2024.107050

Елементи за квалитативну процену научног доприноса кандидата

1. Значај научних резултата

Иван Трапарић дао је свој допринос у различитим областима физике јонизованих гасова и плазме. Главна област истраживања кандидата била је примена машинског учења у спектроскопији плазме, где је постигао запажене резултате.

У оквиру истраживања везаних за примену машинског учења, први пут је успешно применио машинско учење у сврху анализирања Штарковог ефекта. Тачно су предвиђене регуларности дуж спектралних серија неутралног атома литијума, а модел је успешно предвидео и сатурацију полуширине услед Штарковог ефекта која настаје услед Дебајевог екранирања емитера. Такође, демонстрирано је и да модел може јако ефикасно да да процену Штаркове полуширине за било који емитер са одступањем од 20 % у односу на експериментална мерења, што је у складу са семи класичним пертурбационим моделом (енг. *SCP – Semiclassical Perturbation Theory*) Сахал Брешо и Димитријевића на чијим резултатима је исти и обучаван.

Такође, услед доступности опреме у Лабораторији за спектроскопију плазме и ласере, снимљена је тест база под истим условима као и база за потребе упоредног такмичења (енг. *benchmarking*) на ЛИБС 2022 међународној конференцији. Идеја је била да се по први пут проба метод обучавања модела на бази која снимљена са истим инструментом у другој лабораторији, а да се потом обучени модел искористи за квантитативну анализу снимљених узорака у сопственој лабораторији. Резултати овог истраживања демонстрирају да је овај метод остварив, али како би примена машинског учења до краја заживела у ЛИБС квантитативној анализи, потребна је стандардизација методе што је и дискутовано у раду.

Коначно, кандидат је дао и велики допринос у експерименталној поставци, реализацији експеримента и тумачењу резултата у оквиру пројекта ИДЕЈЕ. Овде је демонстрирана могућност раздвајања Балмер алфа линија водоника и деутеријума коришћењем спектроскопије ласерски индукваног пробоја на ниском притиску. Добијени однос сигнал/шум и резолуција са којом су ове линије раздвојене сугерише да је ова метода погодна за раздвајање Балмер алфа линија деутеријума и трицијума у сврху процене концентрације уграђеног трицијума у први зид реактора.

2. Параметри квалитета часописа

Др Иван Трапарић је током своје каријере објавио шест радова у међународним часописима, од тога два рада од претходног избора у звање. Квалитет објављених радова може се проценити на основу квалитета часописа у којима су ови радови објављени:

- 2 рада у врхунском међународном часопису *Spectrochimica Acta Part B: Atomic Spectroscopy* (M21, IF 3.2)
- 1 рад у врхунском међународном часопису *Neural Computing and Applications* (M21, IF 6.0 (2022))
- 1 рад у међународном часопису: *The European Physical Journal D* (M23, IF 1.6)
- 2 рада у међународном часопису: *Contributions of the Astronomical Observatory Skalnaté Pleso* (M23, 0.4)

Укупан импакт фактор публикованих радова кандидата је **14.80**.

	ИФ	М	СНИП
Укупно	14.80	33	5.175
Усредњено по чланку	2.46	5.5	0.862
Усредњено по аутору	1.23	2.75	0.431

3. Позитивна цитираност кандидата

Према Scopus бази података ([Scopus link](#)) радови др Ивана Трапарића цитирани су 7 пута без ауоцитата са укупним h – фактором 2.

4. Нормирање броја коауторских радова, патената и техничких решења

Два рада др Ивана Трапарића спадају у експерименталне радове у природно – математичким наукама па се радови са 7 коаутора узимају са пуном тежином. Како на свим радовима број коаутора не прелази овај број, оба рада улазе са пуном тежином.

Остала четири рада представљају нумеричке симулације у области природно – математичких наука те се радови са 5 коаутора узимају са пуном тежином. Број коаутора на овим радовима такође не прелази овај број, па сви радови улазе са пуном тежином.

5. Учешће на пројектима, потпројектима и пројектним задацима

Др Иван Трапарић већ око годину дана активно учествује као члан пројектног тима на пројекту NOVA2LIBS4fusion који се финансира у оквиру позива ИДЕЈЕ Фонда за науку Републике Србије.

6. Предавања по позиву на конференцијама, друга предавања и активности

Др Иван Трапарић одржао је два предавања по позиву на међународним конференцијама

1. I. Traparić, *Stark Broadening Modeling with ML and AI Algorithms*, XIV Serbian Conference on Spectral Line Shapes in Astrophysics, 19 – 23 June 2023, Bajna Bašta, Serbia
2. I. Traparić, *Application of Machine Learning and Artificial Intelligence in Plasma Spectroscopy*, 32nd SPIG, 26 – 30 August 2024, Belgrade, Serbia

Поред тога, учествовао је на следећим међународним конференцијама и стручним школама:

1. SLSP 6 – *Spectral Line Shapes in Plasmas 6*, 2022, Јер, Француска
2. SPIG 2020 – *Syposium of Physics of Ionized Gases*, онлајн
3. SPIG 2022 – *Syposium of Physics of Ionized Gases*, 2022, Београд, Србија
4. SPIG 2024 – *Syposium of Physics of Ionized Gases*, 2024, Београд, Србија
5. XIV SCCLSA – *Serbian Conference on Spectral Line Shapes in Astrophysics*, 2023, Бајна Башта, Србија
6. ICSLS – *International Conference on Spectral Line Shapes*, 2024, Отсу, Јапан

7. Рецензије у међународним часописима

Др Иван Трапарић био је рецензент два рада у *Applied Spectroscopy* (М22, ИФ 2.2). Потврда је преузета са сајта *Publons* и дата је у прилогу у наставку.

8. Ангажман у настави

Др Иван Трапарић је три године држао наставу физике на међународном програму Интернационалне матуре (енг. IB DP – International Baccalaureate Diploma Programme) у десетој гимназији „Михало Пупин“ у Београду.

Елементи за квантитативну анализу научног доприноса кандидата

Остварени резултати (Табела 1):

Табела 1. Остварени резултати

Категорија	М бодова по раду	Број радова	Број радова за нормирање	Укупно М бодова	Укупно М бодова са нормирањем
M21	8	3	0	24	24
M23	3	3	0	9	9
M33	1	4	0	4	4
M34	0.5	6	0	3	3
M70	6	1	0	6	6
			Укупно	46	46

Поређење са минималним квантитативним условима за избор у звање научни сарадник (Табела 2.)

Табела 2. Минимални услови

	Минимално	Остварени резултати	Остварени резултати са нормирањем
Укупно	16	46	46
M10+M20+M31+M32+M33+M41+M42	10	37	37
M11+M12+M21+M22+M23	6	33	33

Списак научних радова кандидата

M21:

1. Tapalaga, I., **Traparić, I.**, Trklja Boca, N., Purić, J., Dojčinović, I.P., *Stark spectral line broadening modeling by machine learning algorithms*. Neural Comput & Applic **34**, 6349–6358 (2022). <https://doi.org/10.1007/s00521-021-06763-4>
2. M Ivkovic, J Savovic, Biljana D Stankov, M Kuzmanovic, **I Traparic**, *LIBS depth-profile analysis of W/Cu functionally graded material*, Spectrochim. Acta B **213** (2024) 106874, <https://doi.org/10.1016/j.sab.2024.106874>
3. **I Traparic**, D Rankovic, Biljana D Stankov, J Savovic, M Kuzmanovic, M Ivkovic, *Resolving studies of Balmer alpha lines relevant to the LIBS analysis of hydrogen isotope retention*, Spectrochim. Acta B **221** (2024) 107050, <https://doi.org/10.1016/j.sab.2024.107050>

M23:

4. **Traparić, I.**, Ivković, M. *Determination of austenitic steel alloys composition using laser-induced breakdown spectroscopy (LIBS) and machine learning algorithms*. Eur. Phys. J. D **77**, 30 (2023). <https://doi.org/10.1140/epjd/s10053-023-00608-6>
5. NM Sakan, **I Traparic**, VA Sreckovic, M Ivkovic, *The usage of perceptron, feed and deep feed forward artificial neural networks on the spectroscopy data: astrophysical & fusion plasmas*, Contrib. Astron. Obs. Skalnaté Pleso **52**, 97-104, 2022, <https://doi.org/10.31577/caosp.2022.52.3.97>
6. Z Majlinger, **I Traparic**, *New perspectives in the analysis of Stark width regularities and systematic trends*, Contrib. Astron. Obs. Skalnaté Pleso **53**, 58-71, 2023, <https://doi.org/10.31577/caosp.2023.53.3.58>

M33:

1. **I. Traparić** and M. Ivković, VUV SPECTROSCOPY OF THE He II - LYMAN SERIES FOR ELECTRON DENSITY ESTIMATION, Publ. Astron. Obs. Belgrade No. **99** (2020), 197 – 200
2. Nenad M. Sakan, Milica L. Vinić, Vladimir A. Srećković, **Ivan R. Traparić** and Milivoje R. Ivković, APPLICATION OF ARTIFICIAL NEURAL NETWORK IN THE ANALYSIS OF THE SPECTRA FROM LASER ABLATION COMBINED WITH FAST PULSE DISCHARGE, Publ. Astron. Obs. Belgrade No. **102** (2022), 223 – 226
3. Irinel Tapalaga, **Ivan Traparić**, Nora Trklja Boca, Jagoš Purić and Ivan P. Dojčinović, Modeling of Stark Spectral Line Broadening by Machine Learning Algorithms, Publ. Astron. Obs. Belgrade No. **102** (2022), 243 – 246
4. **I. Traparić**, M. Jovanović, M. Kuzmanović and M. Ivković, Elemental Analysis of Austenitic Steel by Calibration-Free LaserInduced Breakdown Spectroscopy (CF-LIBS), Publ. Astron. Obs. Belgrade No. **102** (2022), 137 – 140

M34:

1. **Ivan Traparić**, Application of Machine Learning and Artificial Intelligence in Plasma Spectroscopy, Publ. Astron. Obs. Belgrade No. **103** (2024), 113
2. **Ivan Traparić**, Biljana Stankov and Milivoje Ivković, DETECTION OF RHENIUM IN TUNGSTEN USING LIBS WITH ADDITIONAL FAST PULSE DISCHARGE, Publ. Astron. Obs. Belgrade No. **103** (2024), 152
3. **Ivan Traparić**, Biljana Stankov, Nikola Vujadinović, Milica Vinić and Milivoje Ivković, INFLUENCE OF THE ABLATION ANGLE CHANGE ON SPECTRAL LINE INTENSITIES IN LIBS EXPERIMENTS, Publ. Astron. Obs. Belgrade No. **103** (2024), 153
4. **Ivan Traparić**, STARK BROADENING MODELING WITH ML AND AI ALGORITHMS, XIV Serbian Conference on Spectral Line Shapes in Astrophysics Bajina Bašta, Serbia, Book of Abstracts, Eds. Luka Č.Popović, Nataša Bon, Edi Bon and Sylvie Sahal-Bréchet, 2023, 56.

M70:

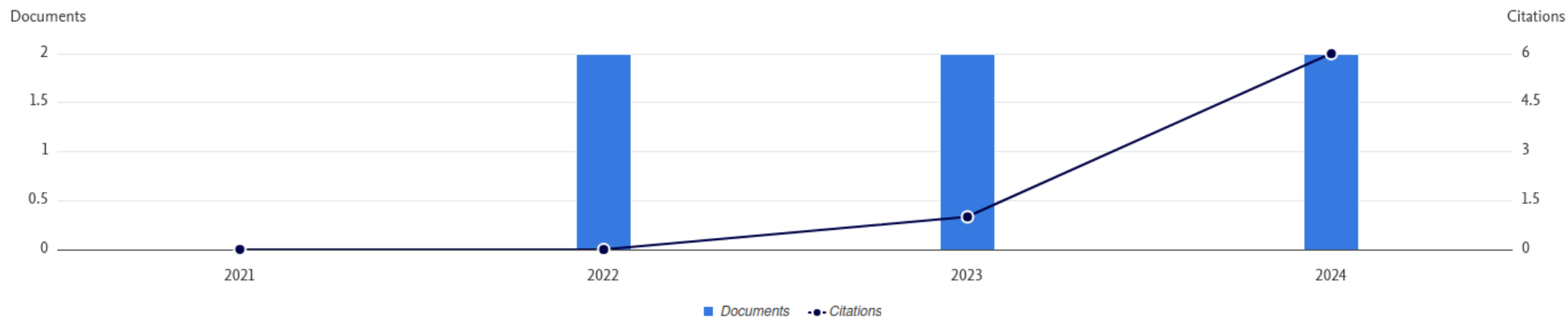
1. **Ivan Traparić**, „Primena mašinskog učenja i veštačke inteligencije u spektroskopiji plazme“, Doktorska disertacija, Fizički fakultet, Univerzitet u Beogradu, 2024

Citation overview

Traparić, Ivan

4 Documents 7 Citations 2 h-index

Date range: [2021](#) to [2024](#) Exclude self citations of selected author Exclude self citations of all authors Exclude book citations Hide documents with 0 citations [?](#) [Export](#)



Sort by [Date \(newest\)](#)

Documents	Year	<2021	2021	2022	2023	2024	Subtotal	>2024	Total
Total		0	0	0	1	6	7	0	7
1 LIBS depth-profile analysis of W/Cu functionally graded material	2024	0	0	0	0	2	2	0	2
2 Determination of austenitic steel alloys composition using laser-induced breakdown spectroscopy (LIBS) and machine learning a...	2023	0	0	0	1	2	3	0	3
3 Stark spectral line broadening modeling by machine learning algorithms	2022	0	0	0	0	0	0	0	0
4 The usage of perceptron, feed and deep feed forward artificial neural networks on the spectroscopy data: astrophysical & fusion p...	2022	0	0	0	0	2	2	0	2

Refine results

Quick filters

- Verified reviews
- Publicly displayed reviews
- Reviews with content
- Community reviews
- Web of Science Core Collection publications

Journals



Journal Research Field (ESI)

2 peer review records of 2 manuscripts

Date reviewed: newest first ▾

< 1 of 1 >

A Study of Spectral Signal Effect for Self-Holes in Metal Additive Manufacturing Components Using Laser-Induced Breakdown Spectroscopy (LIBS)

Applied Spectroscopy

Aug 14, 2023    [Edit](#) [Delete](#)

Recurrent Neural Networks for Prediction of Aluminum Alloy Concentrations in Laser Induced Breakdown Spectroscopy

Applied Spectroscopy

May 8, 2023    [Edit](#) [Delete](#)



Resolving studies of Balmer alpha lines relevant to the LIBS analysis of hydrogen isotope retention

I. Traparic^a, D. Rankovic^b, B.D. Stankov^a, J. Savovic^c, M. Kuzmanovic^b, M. Ivkovic^{a,*}

^a Institute of Physics, University of Belgrade, 11080 Belgrade, Serbia

^b Faculty of Physical Chemistry, University of Belgrade, 11158 Belgrade, Serbia

^c Vinca Institute of Nuclear Sciences, University of Belgrade, 11000 Belgrade, Serbia

ARTICLE INFO

Keywords:

Hydrogen isotopes
Balmer alpha lines
LIBS, hydrogen isotope retention
Plasma-facing components

ABSTRACT

Utilizing Laser-Induced Breakdown Spectroscopy (LIBS) for detecting deuterium and tritium retention in fusion devices poses a significant challenge due to the experimental limitations in resolving hydrogen isotope Balmer alpha lines (H_{α} , D_{α} , and T_{α}). This study utilizes the Rayleigh criterion to distinguish T_{α} and D_{α} lines by determining the maximum line widths and corresponding plasma parameters. Experimental validation was performed through LIBS analysis of heavy water-doped graphite/silica gel targets in both argon and helium atmospheres to assess the predicted plasma parameters and line profile shapes. The optimization of laser pulse energy, gas pressure, delay, and gate times aimed at achieving fully resolved lines based on the intensity, width, and the dip between deuterium and hydrogen Balmer alpha lines. By fine-tuning these experimental parameters, the study successfully achieved a dip of less than 10 % between the H_{α} and D_{α} lines with a satisfactory signal-to-noise ratio, demonstrating the feasibility of fully resolving the T_{α} and D_{α} lines. These findings underscore the potential of LIBS in enhancing the detection of deuterium and tritium retention in fusion devices.

1. Introduction

Resolving the challenges surrounding energy production stands at the forefront of modern science and technology. Nuclear fusion is a clean and sustainable energy production that holds the promise of addressing global energy demands. A fusion reactor uses deuterium (D) and tritium (T) as fuels to produce inert gas helium, high-speed neutrons, and vast amounts of energy without producing long-lived radioactive waste. Despite its immense potential, the complexity and costliness of fusion reactors necessitate collaborative efforts on an international scale, exemplified by the joint endeavor to construct the International Thermonuclear Experimental Reactor (ITER) among participating nations such as the EU, USA, Japan, Russia, China, India, and South Korea [1].

The development and maintenance of nuclear fusion reactors are vital to sustain the promise of clean and efficient energy production. Amidst the complex operational challenges faced by fusion reactors, attention must be given to the impact on plasma-facing components (PFCs), exposed to various stresses, requiring meticulous material composition monitoring and particularly critical hydrogen isotope retention studies. In a nuclear fusion reactor, PFC faces intense plasma radiation, thermal loads, and neutron fluxes, leading to structural

material damage. Thermal loads may cause re-crystallization, cracks, melting, and dust formation. Plasma exposure leads to sputtering, hydrogen isotope retention, and helium-induced morphology changes. Potential defects and transmutations may appear under neutron action. Because of this, in-situ real-time material analysis is essential to prevent an unexpected failure. Monitoring hydrogen isotope retention in PFCs is particularly important as it may affect fuel efficiency, plasma density, and the density of neutral hydrogen in the plasma boundary, essential for the safe operation of nuclear fusion installations [2]. Consequently, hydrogen isotope retention studies play a key role in PFC diagnostics [2–6].

Numerous research papers focus on various methodologies for PFC characterization [7,8]. Two currently significant techniques for the ex-situ characterization of fusion-relevant materials are accelerator-based Ion Beam Analysis (IBA) and Thermal Desorption Spectroscopy (TDS) [3,9–13]. IBA encompasses setups like Nuclear Reaction Analysis (NRA) and Elastic Recoil Detection Analysis (ERDA) crucial for quantifying light isotopes due to their sensitivity and selectivity. Additionally, TDS offers insights by analyzing demounted (from the reactor) material samples using a quadrupole mass spectrometer with an enclosed ion source to evaluate hydrogen isotope desorption behavior. However, TDS

* Corresponding author.

E-mail address: ivke@ipb.ac.rs (M. Ivkovic).

<https://doi.org/10.1016/j.sab.2024.107050>

Received 10 June 2024; Received in revised form 13 September 2024; Accepted 16 September 2024

Available online 21 September 2024

0584-8547/© 2024 Elsevier B.V. All rights are reserved, including those for text and data mining, AI training, and similar technologies.

cannot provide information on the depth distribution of fuel concentrations. Radiofrequency Glow Discharge Spectrometry (RF-GDOES) proves effective for depth profiling of PFCs, as demonstrated in studies such as the analysis of deuterium in tungsten [2].

Laser Induced Breakdown Spectroscopy holds a prominent position among techniques applied for PFCs analysis within fusion devices. Its analytical capabilities have been extensively documented in many books and review articles [14–20]. LIBS is a minimally invasive non-contact technique suitable for multi-element analysis, including depth profiling, without requiring sample preparation. The technique is adaptable for vacuum or low-pressure gas environments and excels in remote in situ analysis. Notably, LIBS allows for on-site analysis without the need to dismantle or cut samples from the reactor, reducing costs and eliminating issues related to PFC replacement due to structural non-uniformity. Moreover, LIBS offers versatility in analyzing various reactor components beyond those that are easily disassembled. Review articles [21–23] provide an overview of the current state of LIBS development for fusion applications. Various LIBS systems were used for diverse characterization objectives, such as identifying elemental composition, depth profiling, deposited layer thickness, or spatial analysis. The efficiency of LIBS as a remote online diagnostics tool was demonstrated by analyzing multilayer structures, simulating the surface of a PFC covered with deposited impurity layers [24]. Specifically tailored LIBS configurations optimized for vacuum operation showcased promising results, including a compact system integrated onto the robotic arm of the Frascati Tokamak Upgrade (FTU) for ITER-relevant sample analysis [25], demonstrating improved spectral resolution in double-pulse (DP-LIBS) over single-pulse (SP-LIBS) configurations. Notably, the exceptional sensitivity of LIBS to lighter elements has been found application in hydrogen isotope retention investigations [26–35]. At Experimental Advanced Superconducting Tokamak (EAST) [26], a remote in situ laser-induced breakdown spectroscopic (RIS-LIBS) system has been developed for the determination of PFC composition (fuel retention, impurity deposition, and deposited layer thickness) [26]. Isotope lines D_α and H_α were identified but only partially resolved. The limit of detection of H/D was estimated to be about 200 ppm in the lithium layer on the first wall [27] applied LIBS for in-situ probing of D retention and Li deposition on a W-PFC surface after being exposed to D plasmas in a tokamak. Deuterium retention inside both pure and lithiated tungsten was investigated, and it was found that the D_α and H_α signals of lithiated W are significantly more intense than those of pure W. LIBS was also applied for in-situ diagnostics of the Li-H/D co-deposition on the first wall of EAST [28]. The results showed that the D_α and H_α signal intensities disappeared after the third laser shot, which was explained by the greater depth of the nanosecond laser ablation than the thickness of the deposited impurity layer. Additionally, femtosecond laser filamentation-induced breakdown spectroscopy combined with chemometrics methods was used to quantify deuterium content in water samples [29]. Filamentation was found to suppress spectral broadening, and well-resolved peaks of H_α and D_α were obtained. Burger et al. [30] studied the segregation of species and spectral line broadening in D_2O - H_2O plasma produced by single- and double-pulse nanosecond laser ablation in air. It was found that species segregation for laser-produced plasma formed in the air does not significantly impact the ability to distinguish D_α and H_α Balmer lines for the SP-LIBS and DP-LIBS. Fantoni et al. [31] studied the resolving of H_α and D_α lines using double pulse configuration with Nd:YAG lasers having energy of 170 mJ at 1.06 μm to irradiate, in vacuum, Mo target co-deposited with W, Al, and D using vacuum arc deposition method. With a 300 ns delay between pulses, H_α and D_α lines are almost resolved according to the Rayleigh criteria, thus enabling line intensity determination using fitting with Pseudo Voigt functions.

Kautz et al. [32,33] obtained an even better resolution by using fs Ti-sapphire laser (800 nm, 35 fs, 5 mJ) to irradiate H and D loaded Zircaloy-4 targets. In 10 Torr of He, using a gate of 2 μs , FWHM of hydrogen lines from 0.08 to 0.05 nm was obtained for delays from 1 to 26 μs [33]. Using

an ns laser and different pressures of Ar, a slightly greater FWHM was obtained. Later [34], using the same fs laser irradiation of the Zircaloy-4 target with incorporated D or T in 26 Torr of Ar, the hydrogen Balmer alpha lines are clearly resolved from the D_α or T_α . Lowering gas pressure, the line width goes even below 0.08 nm, but the line intensity drops even faster, thus limiting the possibility for resolving D_α from T_α .

Recently [35], the analysis of the parameters influencing resolving and recordings of the fully resolved D_α and H_α lines are obtained in 30 Torr of Ar at delays of 60 μs , but without indicating other experimental conditions.

Achieving direct Laser-Induced Breakdown Spectroscopy (LIBS) analysis of hydrogen isotopes remains a formidable challenge due to the high electron density in laser-induced plasma, intensifying Stark broadening and hindering the clear distinction of closely spaced spectral lines of different H isotopes.

This research aims to enhance the resolution and sensitivity of LIBS for detecting hydrogen isotopes in fusion-relevant materials. The initial focus involved a theoretical exploration to ascertain the maximum line widths for resolving hydrogen Balmer alpha D_α and T_α lines and to determine their real intensity. Parameters such as maximum temperature, electron number density, and instrumental width in conjunction with peak intensity ratios were meticulously assessed. In addition, the influence of the applied approximations on maximum line widths was evaluated.

The experimental verification of obtained results, i.e., generation of plasma condition necessary to resolve hydrogen isotopes Balmer lines, was performed using an earlier proposed [36] CO_2 laser-based LIBS under a low-pressure helium and argon atmosphere. Different graphite targets incorporated with heavy water (D_2O) were analyzed, including the silica gel-doped wet graphite targets.

2. Theoretical considerations

In this section, the requirements for resolving Balmer alpha lines of hydrogen isotopes were analyzed and calculated. Special attention was devoted to calculating the requirements for resolving the tritium Balmer alpha line. This is necessary since tritium control and retention studies are critical for the safety operation of fusion power plants due to the possibility of tritium permeation into the coolant and the difficulties associated with its recovery [37].

However, as tritium is radioactive and its determination is experimentally challenging, laboratory studies of hydrogen retention primarily rely on analyzing deuterium content. A key parameter in applying isotopically resolved LIBS for retention studies is the relation between line broadening and the isotopic shifts. Compared to other Balmer series lines, the Balmer alpha lines, besides being the most intense visible hydrogen line, have lesser Stark broadening than isotopic shifts, so they are commonly selected for hydrogen retention studies. Namely, H_β and D_β lines cannot be resolved under typical LIBS plasma conditions ($N_e = 10^{22} \text{ m}^{-3}$ and $T_e = 10.000 \text{ K}$) since the isotopic shift for the Balmer beta H_β - D_β lines is 0.13 nm [38], while the Stark widths of these lines are 1 nm (according to the computer simulation (CS) calculations [39]). Contrary, under the same plasma conditions, the Stark width of the Balmer alpha lines is 0.23 nm [39], while the isotopic shift for H_α - D_α is 0.18 nm and 0.23 nm for H_α - T_α [38]. The main task of our research was to enhance the sensitivity of LIBS for the detection of hydrogen isotopes. For that purpose, optimal plasma conditions must be found under which hydrogen lines broadening is reduced, peak separation improved, and emission signal increased.

2.1. Determination of the critical FWHM for resolving hydrogen isotope lines

The first step in the analysis was to determine the limiting values of the spectral line widths necessary for resolving the H-D-T lines. From the spectroscopic point of view, lines are resolved if they fulfill the Rayleigh

criterion [29]. Therefore, the theoretical analysis of the overall line profiles (when all three isotopes are present in plasma) was performed to determine the maximum width of spectral lines that satisfy the Rayleigh criterion.

It is shown that the fitting of the hydrogen Balmer series lines with one, two, 4, 6, or seven Lorentzian excellent matches theoretical Stark profiles [40]. This and the fact that fitting the overall hydrogen profiles with one or sum of the Voigt function [40–42] also gives an excellent matching is a clear consequence of the fine structure of these lines. Since each fine structure component can be presented by the Voigt function, the resulting overall profile also has the Voigt shape [43]. Of course, such an approximation can be applied only above the fine structure limit [44]. On the contrary, it is unclear how such a fitting with several Voigt profiles can be easily applied for electron number density diagnostics.

Therefore, in many applications hydrogen profiles were fitted with a single Voigt profile. Determination of the full half width at half maximum, FWHM by such fitting procedure is adequate and is used in this work. On the contrary, deconvolution to determine Stark contribution by equalizing it with Lorentzian contribution to the overall line width may lead to significant errors [45]. More details about this approximation in determining electron density will be discussed in Section 2.3.

First, H_{α} , D_{α} , and T_{α} spectral lines, having the same intensity and line width, were generated using the Voigt approximation, which treats each peak as a sum of fractional contributions of the Gaussian and Lorentzian shapes:

$$w_V = 0.5346 \cdot w_L + \sqrt{0.2169 \cdot w_L^2 + w_G^2} \quad (1)$$

where w_V , w_L , and w_G are the full width at half maximum (FWHM) of the Voigt, Lorentz, and Gaussian profiles, respectively [46].

The Gaussian contribution is taken as the combination of the instrumental (w_i) and the Doppler broadening (w_D) [47]:

$$w_G = \sqrt{w_i^2 + w_D^2} \quad (2)$$

$$w_D = 7.16 \times 10^{-7} \lambda (T/M)^{1/2} \quad (3)$$

where T and M are the temperature and mass of the radiating atom in atomic mass units, and λ is the central wavelength in nm.

The estimated maximum line width (critical FWHM) for which the hydrogen isotope lines can be resolved is shown in Fig. 1. According to Rayleigh's criterion, assuming that the hydrogen isotope line intensities are the same, the critical FWHM to separate the H_{α} peak from the blended D_{α}/T_{α} lines is 0.18 nm (Fig. 1a), and 0.054 nm to resolve the D_{α}

from T_{α} line (Fig. 1b). It should be stressed that even when D_{α}/H_{α} line pair is resolved, the information about T_{α} may be lost entirely. In addition, if one wants to resolve D_{α}/T_{α} line pair, the dip between the D_{α} and H_{α} lines should be 10 % or less of the smaller line peak intensity.

Resolved deuterium and hydrogen lines were obtained in LIBS spectra of samples with different deuterium concentrations, confirming that the critical FWHM for H_{α}/D_{α} line separation is attainable [29–36]. It is much harder to attain the minimum peak width necessary to separate the $D_{\alpha} - T_{\alpha}$ line pair. In addition, the critical FWHM for resolving lines depends on the assumed peak intensities' ratio, R . Dependence of, determined, (critical for D_{α} and T_{α} lines resolving according to the Rayleigh criterion) FWHM dependence on a line intensity ratio in the range from 0.1 to 1 is presented in Table 1. The critical FWHM depends on the assumed ratio between D_{α} and T_{α} line intensities, R , regardless of which line is more intense, i.e., there was no difference between critical FWHM values obtained for intensity ratios of 0.5 and 2. Therefore, Table 1 presents only the values for intensity ratios between 0.1 and 1. To simplify procedure for critical FWHM determination, lines were approximated by Voigt profiles using the same line width for all lines.

As illustrated in Table 1, the determined critical FWHM of Voigt profiles for resolving D_{α} and T_{α} lines go from 0.027 to 0.054 nm, depending on the line intensity ratio. The results in Table 1 suggest that as the intensity ratio between these two lines decreases, it becomes more challenging to resolve D_{α} and T_{α} lines experimentally.

The dependence of determined critical FWHM on the assumed ratio of peak intensities of the Balmer alpha lines can be, besides in Table 1, presented by eq. (4), which enables easy calculation of the maximum FWHM necessary for resolving studied lines, for the estimated value of R :

$$FWHM_{cr} = 0.0599 - 0.0388 \times \exp(-1.765 \times R) \quad (4)$$

2.2. Critical plasma parameters for resolving hydrogen isotope lines

Resolving hydrogen isotope lines requires detecting a spectral signal at reduced electron density with corresponding narrower line widths. In other words, plasma parameters (T and N_e) must be optimized to ensure the conditions necessary to decrease electron density without a

Table 1

Critical FWHM for resolving D_{α} and T_{α} for different intensity ratios.

Line intensity ratio (R)	0.1	0.3	0.5	0.67	0.8	1
Critical FWHM	0.027	0.038	0.044	0.047	0.050	0.054

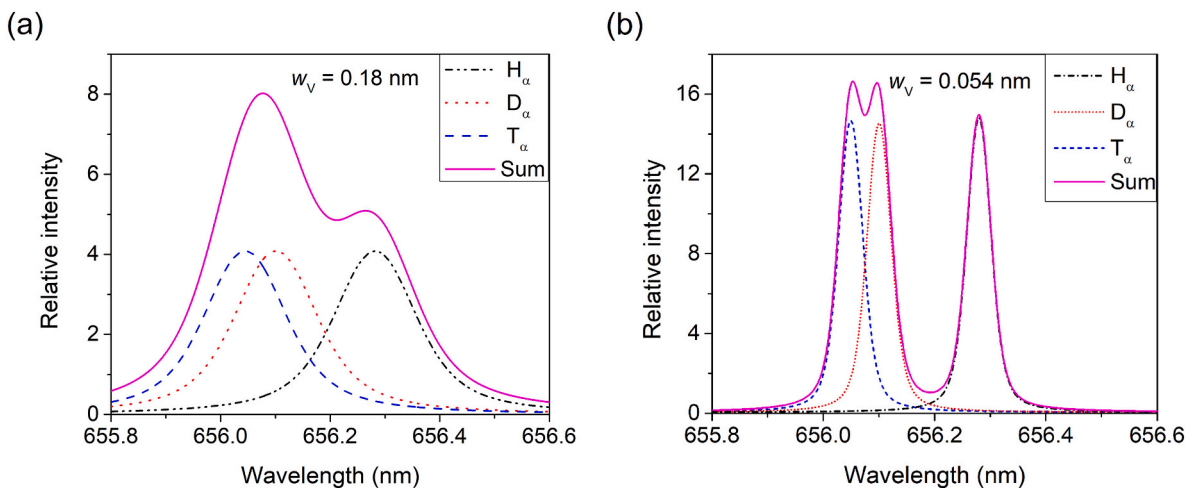


Fig. 1. Voigt approximation of hydrogen spectral lines having equal line widths and intensities and critical FWHM for resolving (a) H_{α} and D_{α} and (b) D_{α} and T_{α} peaks.

significant decrease in light emission intensity.

Electron density from the width of the H_α can be determined using different approaches since much work was devoted to studying this line. For example, it is shown [48] that using Griem theory, there is a considerable difference between electron densities determined from Balmer alpha and Balmer beta line widths. Having in mind the high accuracy of the H_β line theory, electron density can be determined using the correction factor between theories of the H_α and H_β widths.

In this work, according to the approximation that the Stark profile of the H_α line at electron densities greater than 10^{21} m^{-3} is close to Lorentzian [45], the eq. (1) was used to obtain Stark broadening contribution to overall line width, assuming $w_L = w_S$. Then, eq. (5) [39] was used to calculate N_e :

$$N_e [\text{m}^{-3}] = 10^{23} \cdot (w_S [\text{nm}] / 1.098)^{1.47135} \quad (5)$$

Fig. 2 shows the maximum values of plasma parameters (T and N_e), under which critical FWHM for T_α , D_α resolving is obtained, estimated for different values of the instrumental FWHM parameter, w_i . Plasma parameters were calculated for two critical line width values corresponding to two values of R spectral line intensity ratios. Upon approaching the limit value of $N_e = 1.2 \times 10^{21} \text{ m}^{-3}$ as shown in Fig. 2a, it becomes impossible to obtain the parameters (T and w_i) required to resolve both the D_α and T_α , when $R = 1$. Additionally, it is observed that for an electron density of approximately $4 \times 10^{20} \text{ m}^{-3}$ and temperature less than 6000 K, (corresponding to LIBS plasma at later evolution times), the instrumental FWHM should be less than 0.027 nm to resolve the T_α and D_α lines. Also, with equal peak intensities, if the temperature is higher than 10,000 K and N_e greater than $4 \times 10^{20} \text{ m}^{-3}$, the instrumental width must be smaller than 0.02 nm. As shown in Fig. 2b, for an N_e lower than $1 \times 10^{20} \text{ m}^{-3}$ and a minimal instrumental width of less than 0.01 nm, the temperature cannot exceed 3000 K.

2.3. Validity of approximations used for simulation of line profiles

Several approximations were used to determine critical, i.e., maximal FWHM and plasma parameters necessary to resolve hydrogen isotope Balmer alpha lines. Therefore, the validity of these approximations and their influence on determined parameters will be analyzed.

2.3.1. Approximation of line profiles with Voigt function

The validity check of the Voigt approximation, in the determination of the plasma conditions required for resolving studied lines, was performed by comparing estimated parameters with those obtained using

the Computer Simulation model of hydrogen spectral line profiles (CS tables) given by Gigos et al. [39]. Previous studies [45] have confirmed the validity of approximating hydrogen Balmer alpha line shapes using the Voigt function. Conversely, determining the width by fitting hydrogen lines with the Voigt function, even by fixing the Gaussian contribution to the line width, can lead to significant errors at low electron densities. Therefore, the calculation of plasma parameters was performed using relation (5) [39,45] to improve their accuracy.

The difference in calculated values for the instrumental width $w_i = 0.01 \text{ nm}$, and $w_i = 0.027 \text{ nm}$ respectively, (0.027 CS and 0.01 CS), was illustrated in Fig. 2 a,b, respectively. Error bars, included for these data in Fig. 2, indicate uncertainty of used formula. The slight variation between these values can be attributed to the contribution of a Doppler broadening mechanism because Voigt profiles were generated assuming identical widths of all three lines. For example, in the Voigt approximation, all three lines have a width of 0.054 nm, whereas the precise values are 0.0598 nm for H_α , 0.052 nm for D_α , and 0.049 nm for T_α .

2.3.2. Consistency in the assumption of the same stark widths and shifts

Different Stark widths of Balmer alpha lines of hydrogen and deuterium were reported [49]. The author measured the Stark-broadened line profiles of H_α and D_α in a wall-stabilized argon arc at an electron density of $N_e = 1.4 \times 10^{22} \text{ m}^{-3}$ and found the half width of D_α to be about 15 % smaller than the width of H_α . It was found that only about 5 % of the measured 15 % difference between the experimental H_α and D_α profiles can be explained by differences in Doppler widths and inaccuracies in reproducing the exact electron density, while the major portion ($\approx 10\%$) must be attributed to ion dynamic effects. In reference [49], for the evaluation of N_e through the Stark broadening of the D_α line, the numerical factor of 0.9 was introduced in relation (5) to account for the reduced Stark broadening of the D_α compared to the H_α line.

Our study of the necessary conditions for resolving the H_α , D_α , and T_α peaks assumed the same values for FWHM of these lines. Therefore, the impact of disregarding the influence of the reduced mass on the line profile was examined using CS tables [39]. The analysis was performed for four values of a reduced mass of 0.5, 0.8, 1, and 2, corresponding (in case of equal gas and electron temperatures) to different plasma compositions: pure hydrogen, hydrogen-helium, hydrogen-argon, and a mixture of argon with deuterium or all three hydrogen isotopes, respectively. It was concluded that ion dynamics affects the line shapes, resulting in the observed difference in line widths. As a result, observed differences could impact the precision of estimated widths and plasma conditions for separating D_α and T_α peaks in the studied range of densities. Namely, according to the CS simulation results, a dip between

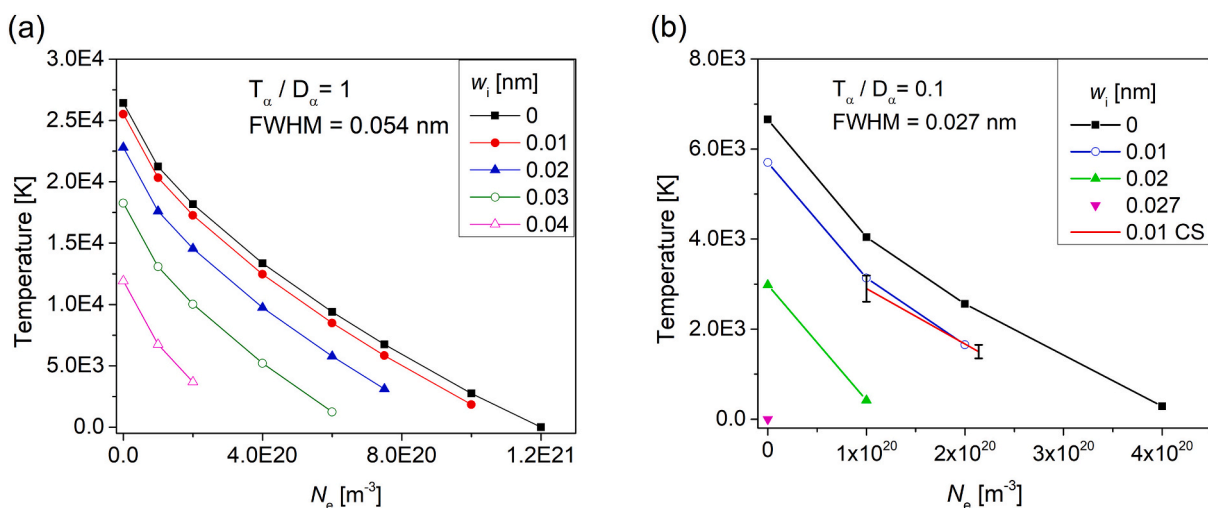


Fig. 2. Relationship of the maximal electron temperature versus the electron density corresponding to different values of the instrumental FWHM calculated for two critical line width values: a) critical FWHM = 0.054 nm, $T_\alpha/D_\alpha = 1$, and b) critical FWHM = 0.027 nm, $T_\alpha/D_\alpha = 0.1$.

lines increases with the increase of the reduced mass, which positively influences the conditions for resolving the hydrogen isotope lines. But, neglecting the influence of reduced mass on the line shapes by analyzing theoretical profiles for pure hydrogen only loosens the criteria for maximal FWHM for other μ . In addition, the hydrogen and deuterium spectral line profiles analyzed and experimentally tested in this work correspond to plasma with a simultaneous presence of hydrogen isotopes. On the contrary, in reference [49], measurements were performed for two experimental conditions (with a small percentage of the H or D added to Ar) having different reduced masses, which caused the stated difference in the hydrogen and deuterium line width.

3. Experimental methods and materials

Requirements for line resolution, analyzed in Chapter 2, were experimentally tested using the LIBS setup described in Section 3.1. Emission spectra were recorded using the spectrometer, the resolution of which is analyzed in Section 3.2. The selection of targets and their preparation procedures are described in Section 3.3. To verify the requirements for plasma parameters estimated in Chapter 2, temperature and electron number density diagnostics were performed. These results are described in Section 3.4.

3.1. Experimental setup

The breakdown on a solid target was generated using the modified carbon dioxide TEA laser (Tachisto 215G) operated at $10.6\ \mu\text{m}$, with a repetition rate of 1 Hz. The duration of the main laser pulse was 80 ns with a tail lasting $2\ \mu\text{s}$ (see inset in Fig. 3). The targets were placed within the vacuum chamber mounted on the x-y table (Isel-automation 230,510). The chamber was vacuumed and filled with a continuous argon or helium gas flow at the desired pressure. The laser beam was focused perpendicular to the target surface using a ZnSe lens (L , $f_1 = 100\ \text{mm}$), as illustrated in Fig. 3. Fast imaging was conducted through a lateral window of the vacuum chamber, capturing the plasma image and projecting it onto the entrance slit of a spectrometer. This process utilized an optical fiber settled at 15 degrees and equipped with a collimator (SolarLas PS2) for precise light transmission. For recordings of line shapes, a spectrometer (Sol Instruments MS7504i) was employed, outfitted with an iCCD camera (Andor Technology, model DH734I-18F-63 featuring 1024×1024 pixels, with a size of $13 \times 13\ \mu\text{m}$ and an 18 mm diameter intensifier). The iCCD was controlled using a pulse generator (DG-535, Stanford Research Systems), triggered optically by the occurrence of plasma on the target. A fast photodiode (PD) oriented towards the target was utilized to convert the light signal into electrical

and trigger the DDG. Line shape recordings were performed with full vertical binning and different gate widths at various delay times. The acquisition gate width was varied between 15 ns and $70\ \mu\text{s}$. If not stated otherwise, the gate time was $5\ \mu\text{s}$. The shorter acquisition widths at earlier delays were favorable for tracking fast-changing plasma. Signals were recorded over ten accumulations to mitigate the influence of shot-to-shot variations.

3.2. Instrument selection and determination of instrumental profile

The initial step in experimental evaluation of the criteria for resolving hydrogen isotope Balmer alpha lines involved examining the spectrometer's resolution, i.e., determining the instrumental half-width. Namely, the instrumental half-width must be smaller than the values shown in Table 1. The shape and width of the instrumental profile of the MS 7504i spectrometer were determined by measuring radiation from the Ne pen lamp. The instrumental width (diffraction grating with 1800 groves/mm and a $15\ \mu\text{m}$ wide entrance slit of spectrometer) was determined to be $w_i = 0.03\ \text{nm}$. Thus, it was concluded that the spectrometer was suitable for resolution studies of hydrogen isotope Balmer alpha lines.

3.3. Preparation and testing of targets

The second task was selecting and preparing the targets that could serve as substitutes for the hydrogen isotope-enriched components of the plasma fusion reactor. The material selected for the present study was graphite because of its importance for fusion technology [50,51]. Two preparation procedures were used to obtain graphite targets with embedded D_2O . In the first case, a controlled amount of the D_2O was applied with a micropipette to the surface of a tablet made from spectroscopically pure graphite powder. In this way, graphite targets with a gradient concentration of hydrogen along the sample thickness were produced. These targets were suitable for depth analysis of hydrogen retention, i.e., recording LIBS spectra in which the intensity ratio of hydrogen over deuterium Balmer alpha lines changes with the number of laser shots.

In the second case, tablets were made from graphite powder doped with D_2O and mixed with silica gel (SiO_2). The silica gel was added to prevent a decrease in water content during vacuuming. Before mixing with D_2O -doped graphite, SiO_2 was ground to a fine powder and dried in an oven at $110\ ^\circ\text{C}$ for 20 h to eliminate previously accumulated moisture. The best consistency of the tablets was achieved by mixing the graphite and silica gel powders in the proportion of 3:1. After pressing (10 tons hydraulic press for 30 min), the tablets were dried at $120\ ^\circ\text{C}$ for

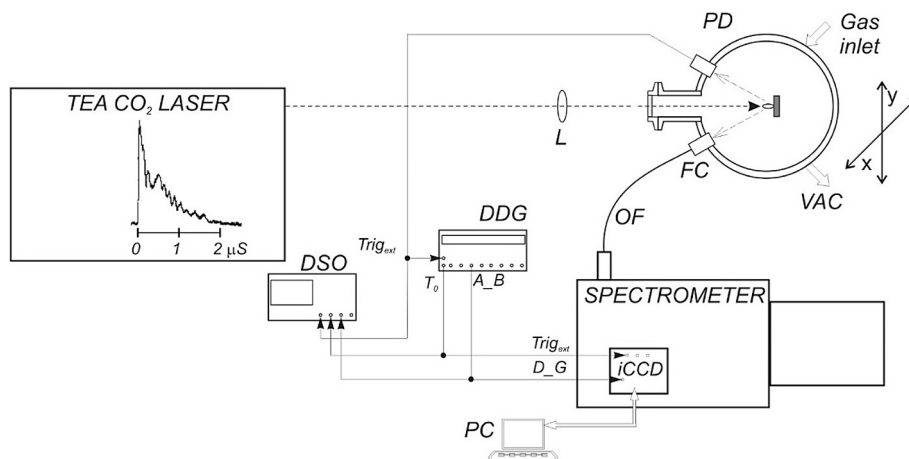


Fig. 3. Experimental setup: L-lens, PD-photodiode, OF-optical fiber, FC-focusing collimator, VAC-vacuum outlet, DSO-digital storage oscilloscope and DDG-digital delay generator.

6 h and stored in a desiccator to prevent moisture absorption. Targets prepared with this procedure had a homogeneous water distribution, as confirmed by LIBS spectra. The intensity ratio of the H α and C II lines remained almost unchanged with increasing number of applied laser shots. The heavy water-doped graphite/silica gel targets were used in all further experiments.

3.4. Plasma diagnostics

The plasma parameter measurements were conducted to experimentally validate the conclusions drawn from the results depicted in Fig. 2. Electron number density was evaluated from the measurement of wavelength separation (s) between peaks of allowed ($2p\ 3P^{\circ} - 4d\ 3D$) and forbidden ($2p\ 3P^{\circ} - 4d\ 3F^{\circ}$) component of the He I 447.1 nm line, using the relation (6) [52], with T_e in K, s in nm and N_e in m^{-3} :

$$\log_{10}(N_e) = 21.5 + \log_{10} \left[\left(\frac{s}{0.1479} \right)^{b(T_e)} - 1 \right]$$

$$b(T_e) = 1.46 \times \frac{8380}{T_e^{1.2}} \quad (6)$$

From the spectra presented in Fig. 4 a, the separation between peaks was determined: $s = 0.206$ nm for shorter delay/gate times ($0.5\ \mu s / 5\ \mu s$) and 0.155 nm for longer delay/gate times ($5.5\ \mu s / 50\ \mu s$). The estimated N_e for shorter and longer delay/gate times were 2.5×10^{21} and $2.7 \times 10^{20}\ m^{-3}$, respectively.

In addition, N_e was determined from the parameters of the He I 492.2 nm line ($2p\ ^1P^{\circ} - 4d\ ^1D$) with forbidden component ($2p\ ^1P^{\circ} - 4f\ ^1F^{\circ}$ and $2p\ ^1P^{\circ} - 4p\ ^1P^{\circ}$) using the relation (7) [53], with T_e in K, s in nm, and N_e in m^{-3} :

$$\log_{10}(N_e) = 21.3065 + \left(\frac{1}{0.8766} \right) \log_{10} \left[\left(\frac{s}{0.131187} \right)^{b(T_e)} - 1 \right]$$

$$b(T_e) = 1.25 + \frac{994}{T_e} \quad (7)$$

Using the separation values $s = 0.203$ nm and 0.146 nm determined from Fig. 4 b, the calculated electron number density was $N_e = 1.5 \times 10^{21}$ and $2.2 \times 10^{20}\ m^{-3}$ for shorter and longer delay/gate times, respectively. From data presented in Fig. 4, for separation between forbidden (F) and allowed (A) components ($s = 0.203$ nm and 0.146 nm) and their intensities ratios ($F/A = 0.196$ and 0.044) the following N_e values were obtained by interpolation of the data according to unified theory (BCS) [54]: 2.03×10^{21} , 3×10^{20} , 1.5×10^{21} and $3.66 \times 10^{20}\ m^{-3}$, which are in reasonable agreement with values obtained from the calculations based on approximative formulas [52,53].

The gas temperature was determined by comparing the synthetic and

recorded spectra of the sequence $\Delta\nu = 0$ of the C₂ molecule Swan system at 515 nm. Fig. 5a shows a part of the $\Delta\nu = 0$ sequence of the C₂ molecule Swan system spectrum, obtained in an Ar atmosphere at reduced pressure (10 millibars) between the band heads (0–0) and (1–1). Spectra were obtained with different delay times (5, 10, and 15 μs), with a gate of 5 μs . As can be seen from the picture, the resolution of the spectrograph and the plasma conditions allow for obtaining spectra with a well-developed rotational structure, where the lines of the R and P branches are well-separated. Due to the decrease of plasma temperature with time, the band intensities obtained for different delay times decrease rapidly with increasing time. In general, the emission of molecular bands is characteristic of the peripheral plasma parts and/or later times of development of the laser-induced plasma: with increasing temperature, the intensity of the emission increases, but at the same time, the concentration of molecules decreases due to dissociation. The maximum emission intensity of the Swan system is usually reached at a temperature around 6700 K [55].

When the rotational structure of molecular band spectra is well resolved, it can be used to determine the temperature of heavy particles. The (0–0) band of the Swan system is very suitable for that purpose: the C₂ molecule has a sufficiently high dissociation energy (6.2 eV) and a sufficiently low excitation energy (2.4 eV) to obtain very intense spectra, and on the other hand, the structure of the energy levels is such that the components of rotational structures can also be separated using a medium-resolution spectrograph. Fig. 5 b shows a detail of the C₂ band spectrum synthesized for different temperatures, with a Gaussian profile corresponding to the instrumental profile of the spectrograph. The Pghoper program [56] was used to synthesize the spectra. The intensity ratio of R components and band head does not depend on temperature, so both synthesized and experimental spectra can be normalized to the intensity of the R component. This way of normalization is better than normalization using the (0–0) band head because of its potential self-absorption. As shown in Fig. 5 b, the intensity ratios of the R and P components of the (0–0) band strongly depend on temperature, so they can be used to estimate plasma temperature.

By comparing the normalized experimental and synthesized spectra, the temperature was estimated for different delay times: for a delay of 5 μs , a temperature value of 5000 K was determined, with an error of 10 %. With the delay time increase, a clear trend of temperature decrease was observed, from 4500 K for a delay of 10 μs to a temperature of about 3500 K for a delay of 20 μs . The intensities were significantly lower for delay times longer than 10 μs , considerably increasing the determination error.

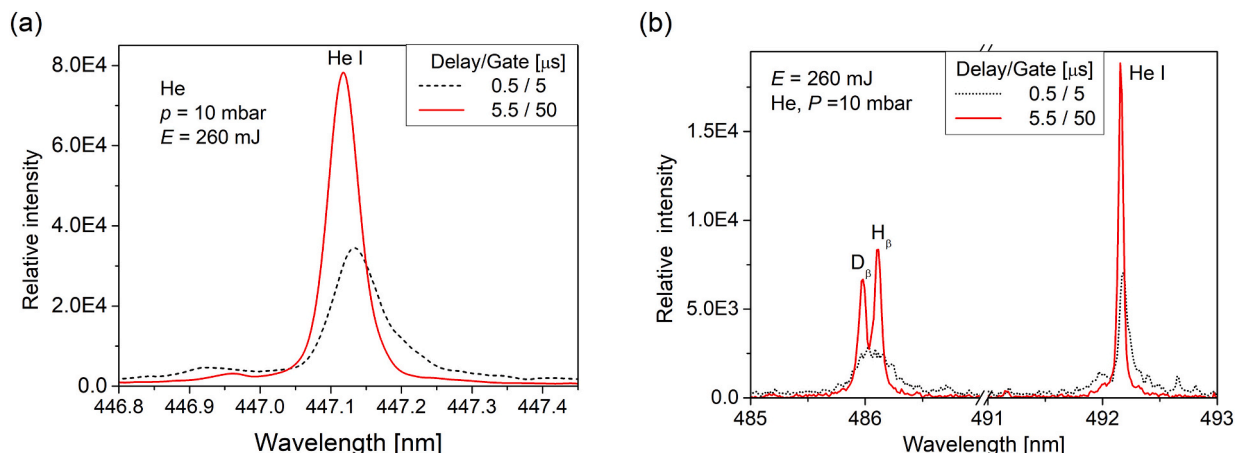


Fig. 4. Examples of the N_e diagnostics: (a) Shape of the He I line at 447.1 nm and (b) Shapes of the hydrogen isotope Balmer beta lines and He I line at 492.2 nm.

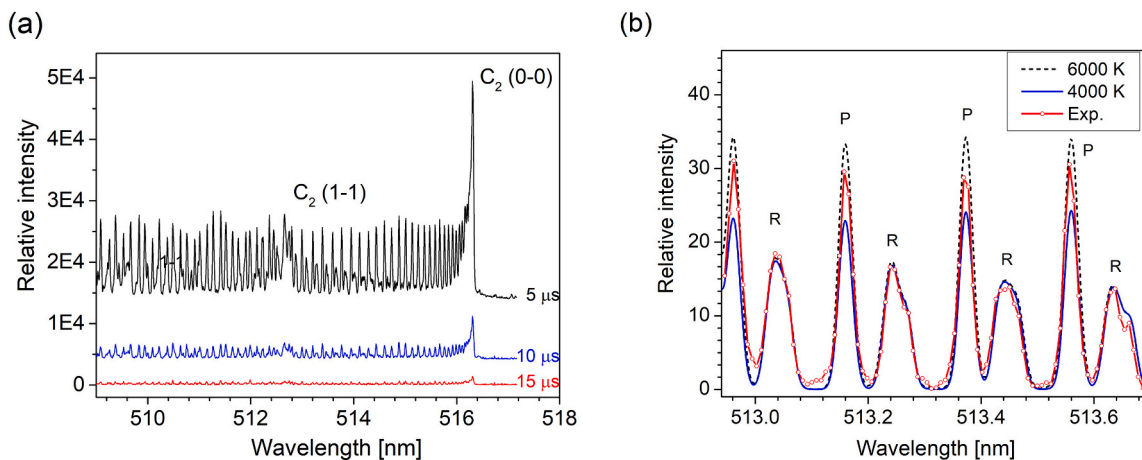


Fig. 5. (a) Experimentally obtained spectra of the Swan band ($\Delta\nu = 0$ sequence) for different delay times. (b) Synthesized normalized spectra for temperatures of 4000 and 6000 K and experimental spectrum for a delay time of 5 μs (part of the (0-0) band).

4. Results

The analysis outlined in Chapter 2 has shown that a necessary requirement for resolving hydrogen isotope lines is employing a spectroscopic instrument with minimal instrumental width and generating plasma with parameters (N_e and T) falling within the limits indicated in Fig. 2. The LIBS operation is commonly performed in air and spectral lines are recorded with some delay period to the laser pulse, to avoid the influence of continuum radiation, i.e., acquisition starts when lines of the studied elements appear in spectra and last, until their intensity becomes comparable to noise.

Typical temperature and electron number density values for laser-induced plasmas are around $T = 15,000$ K and $N_e = 10^{23}$ m^{-3} (or above) [14–20]. The value of N_e is almost two orders of magnitude greater than the values shown in Fig. 2. The plasma induced by Nd:YAG laser in Ar at reduced pressure is characterized by a lower N_e but still far above the values required to resolve the Balmer alpha line. For example, the H_α line measured in tungsten plasma induced in He atmosphere at 10 mbar had FWHM of around 0.5 nm [57], i.e., almost ten times greater than requested for resolving studied lines. In LIBS detection of hydrogen in molybdenum within mixtures of argon and nitrogen at atmospheric pressure it is observed that the width of the H_α line decreases (for the same delay), with shorter duration of plasma, i.e., emission intensities decrease faster than in pure argon [58]. The resolving of the H_α and D_α was obtained using double-pulsed LIBS (with ps and fs lasers) or laser-induced filamentation LIBS. However, the line widths were too wide to resolve D_α and T_α , like the line profiles shown in Fig. 1a.

Resolving D_α and T_α lines is the most critical task for LIBS analysis of hydrogen isotope retention, bearing in mind that the isotope shift

between D_α and T_α is 0.0598 nm, while between H_α and D_α is 0.1785 nm. The targets used in this study did not contain tritium. Nonetheless, the analysis presented in Section 2 (Fig. 1 b) demonstrates that when the H_α and D_α are distinctly resolved, and the dip between these lines accounts for less than 10 % of the intensity of the smaller peak, the requirements for resolving D_α and T_α are met.

In this work, we investigated the potential of LIBS based on TEA CO₂ laser for obtaining well-resolved hydrogen Balmer alpha lines. Experimental parameters were optimized by recording LIBS spectra of heavy water-doped graphite/silica gel targets under different experimental conditions. Three laser energies were used in this study, namely 260 mJ, 320 mJ and 420 mJ. Targets were irradiated in Ar and He atmosphere at different gas pressures (3–80 mbar), and spectra were recorded with variable delay (0.5–15 μs) and gate times (5–50 μs).

The characteristic dependence of the line profiles on delay time at He pressure of 30 mbar are shown in Fig. 6 a, and on He gas pressure at a delay time of 15 μs in Fig. 6 b. Each spectrum is a sum of 10 accumulated laser shots applied at the same spot on the target.

Based on Fig. 6, it can be inferred that ionized carbon lines start to emerge in the spectra during the initial phase of plasma evolution and persist for less than 5 μs . It should be stressed that the width of the C II lines ($3s^2s - 3p^2p^0$) at 657.8 nm and 658.29 nm, recorded at the beginning of the plasma evolution, was 0.033 nm, which confirms that w_i is equal to or slightly less than the stated value. In addition, since the overall width is not greater than the instrumental width, we may conclude that the contribution of the other line-broadening mechanisms was negligible. Further, in the time window 0.5 μs – 5 μs , the N_e value was around 10^{21} m^{-3} since a Stark width of these lines, according to theory [59], is around 0.1 nm at $N_e = 10^{23}$ m^{-3} .

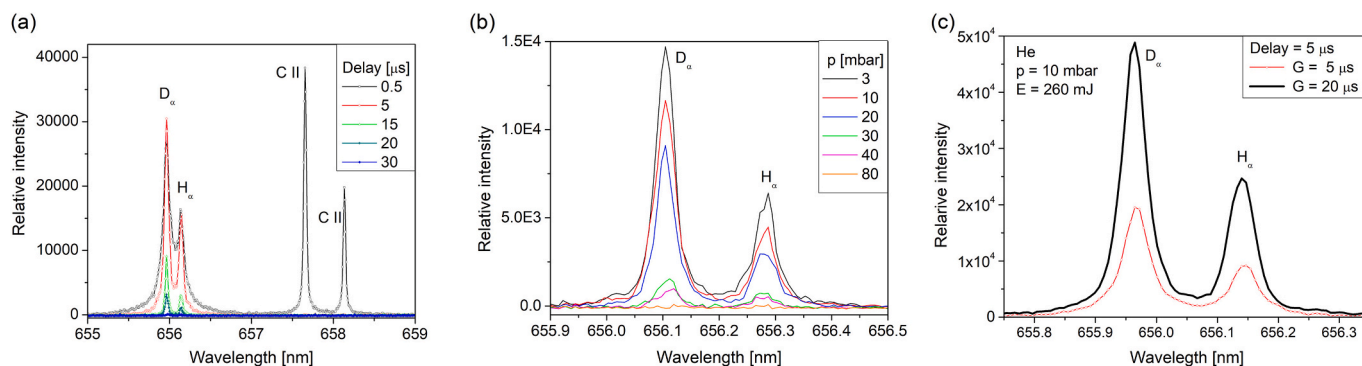


Fig. 6. Variation of line shapes: (a) with delay time at He pressure of 30 mbar and (b) on gas pressure at a delay of 15 μs . The influence of gate time on spectra (c) recorded in He at 10 mbar. All spectra were recorded using the laser energy of 260 mJ. Gate time for (a) and (b) was 5 μs . Delay for (c) was 5 μs .

After a few microseconds, the spectral lines of surrounding gas (He or Ar) and those of hydrogen become more pronounced, thus enabling adequate resolving of the Balmer alpha line from the closely spaced spectral lines of the target material. This fact is significant for studying hydrogen isotope retention in tungsten targets because the presence of the spectral line of W I at 656.32 nm or Be II line at 656.45 nm can make it difficult to separate it from the hydrogen Balmer alpha line. Furthermore, the Balmer alpha lines were not fully resolved at short delay times, see Fig. 6 a, indicating a preference for analysis at delays longer than 15 μs . Fig. 6 also shows that the dip between H_{α} and D_{α} lines decreases with increasing pressure. For pressure higher than 10 mbar, lines are fully resolved. Unfortunately, the intensities of Balmer lines diminish swiftly as the pressure and delay times increase. Hence, the primary objective of this study was to identify experimental parameters where line intensities significantly exceed the noise level and fulfill conditions required for resolution. As the plasma evolves, the line width decreases, indicating improved resolution. However, this decrease in width is accompanied by a decrease in intensity, which presents a drawback. Therefore, when the line width aligns with the instrumental resolution, the remaining signal can be captured by widening the gates for data collection. As an illustration, the spectra recorded in He at 10 mbar, using laser energy of 260 mJ and delay time of 15 μs for gate values of 20 μs and 5 μs , are shown in Fig. 6c.

In argon, under the same experimental conditions as for He gas, the intensity and shape of the hydrogen isotope Balmer alpha lines are considerably different due to the changes in electron number density, electron temperature, and different temporal and space evolution of plasma. The recorded line shapes for a laser energy of 420 mJ and a gate time of 5 μs are shown in Fig. 7a for various delay times.

Considerably greater electron number densities are obtained in LIBS with Ar compared to He. Consequently, the resolution of lines at the beginning of the plasma evolution is of poorer quality (Fig. 7a). However, plasma emission in Ar lasts longer, and for longer time delays (at 50 μs) well-resolved lines of sufficient intensity can also be obtained, see Fig. 7a. The line shapes obtained under same laser energy and gate time parameters, but under varying pressure, are depicted in Fig. 7b, for delay time of 0.5 μs .

As a figure of merit, which will clearly describe the quality of resolving of hydrogen lines, the dip between lines seems to be the most appropriate. The dip was defined as the minimum intensity between lines (presented as a percentage of the lowest peak intensity). Considering that determining the line widths requires fitting, it is clear that dip is a more adequate parameter. Namely, a dip may, without any other procedure, give a reasonable estimate of how far one is from the optimal conditions for resolving not only the H_{α} and D_{α} line, but also for resolving the deuterium and tritium Balmer alpha lines. Fig. 8 shows the

dependence of the dip between hydrogen isotope lines versus studied parameters: laser energy, gas type and pressure, and delay times. For comparison, the line widths are also shown in the same figure.

In Fig. 8, it is evident that the dip value's dependency on gas pressure and laser energy is most notable during the initial stages of plasma evolution. However, as delay times progress, the line width approaches or matches the instrumental width, leading to dip changes among lines comparable to the measurement uncertainty. It is plausible to infer that employing a spectrometer of higher resolution would yield smaller dip and FWHM values, particularly at longer delays.

In argon (Ar), the dip increases with both pressure and laser energy due to the higher electron number density, resulting in an increase in the Stark width of the spectral line. Conversely, when using helium (He) as the surrounding gas, the increment in electron density is less pronounced, leading to a dip that remains nearly unaffected by changes in pressure and laser energy, under studied conditions.

Hydrogen isotope retention studies depend not only on resolving Balmer alpha lines but also on studied line peak intensities. Therefore, we presented the results for lines fitting in the form of peak intensity versus determined FWHM for all experimental parameters. In Fig. 9, gas pressure was used as a parameter, while data for various delay times are presented and labeled for each data point. On the same graph, the critical FWHM value of 0.054 nm (Chapter 2) for resolving D and T Balmer alpha lines having equal intensities is presented as a thick vertical line. The experimental points on the left side of the vertical line display plasma parameters where the line separation was deemed satisfactory. The vertical dotted line presents the value of the minimal instrumental width of the spectrometer. The red arrow indicates the data point for which optimal intensity and resolution of spectral lines were obtained.

Fig. 9 shows that resolved hydrogen isotope Balmer alpha lines can be obtained in both gases, but the line's intensity and signal-to-noise ratios is better in He than in Ar. In addition, at various line peak intensities, the dip between studied D_{α} and H_{α} lines is less than 10 % (see Fig. 8), i.e., line widths much less than 0.054 nm (see Fig. 9) can be obtained, which guarantees, according to the analysis presented in Chapter 2, resolving of D_{α} and T_{α} lines. At optimal conditions for resolving lines, the intensity is much lower than at the beginning of plasma evolution, see Fig. 10a, but still adequate for determining their intensities with high accuracy, see Fig. 10b.

5. Conclusion

This study examined the resolution of hydrogen isotope Balmer alpha lines, a crucial aspect for tritium retention investigations using LIBS. Key highlights of the study included determining the critical line

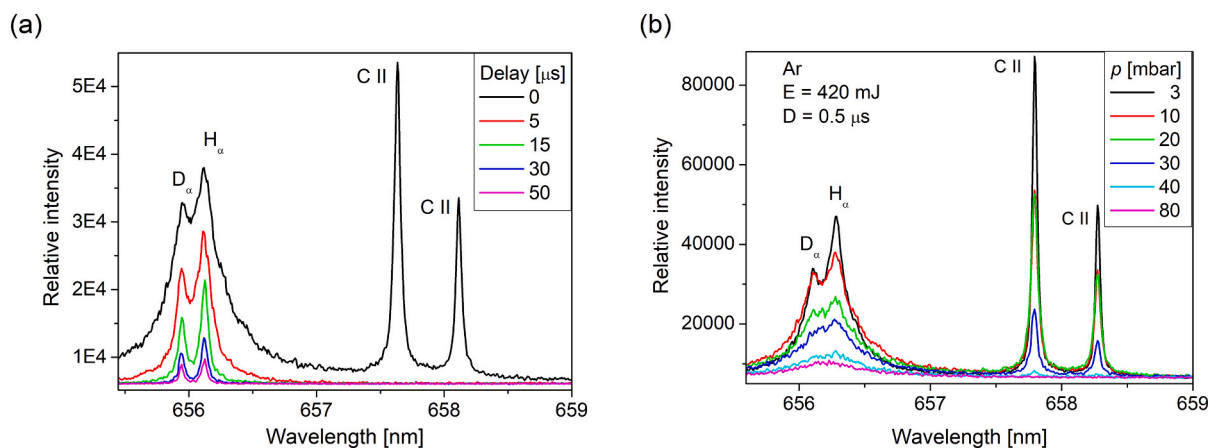


Fig. 7. Figure (a) illustrates the variation of line shapes with delay time at an argon pressure of 10 mbar, while figure (b) shows the influence of gas pressure at a delay of 0.5 μs . The laser energy and gate time used for these measurements were 420 mJ and 5 μs , respectively.

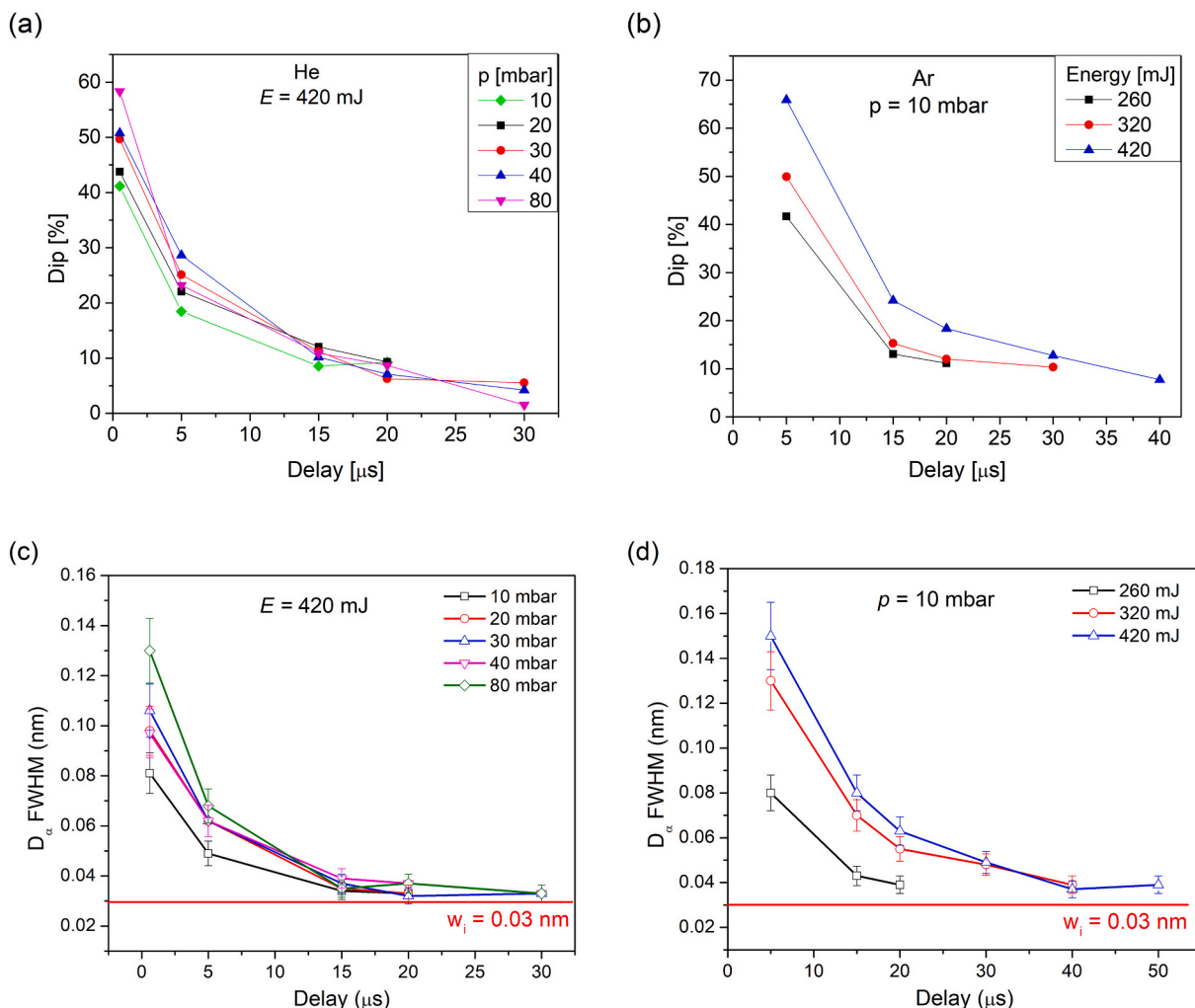


Fig. 8. Dip between H_{α} and D_{α} lines expressed in the percentage of the lower peak intensity versus delay for a different: (a) He gas pressure, (b) laser energy in Ar at 10 mbar. FWHM of the H_{α} and D_{α} lines at conditions: c) same as a) and d) same as b). All data are recorded using a gate time of 5 μ s.

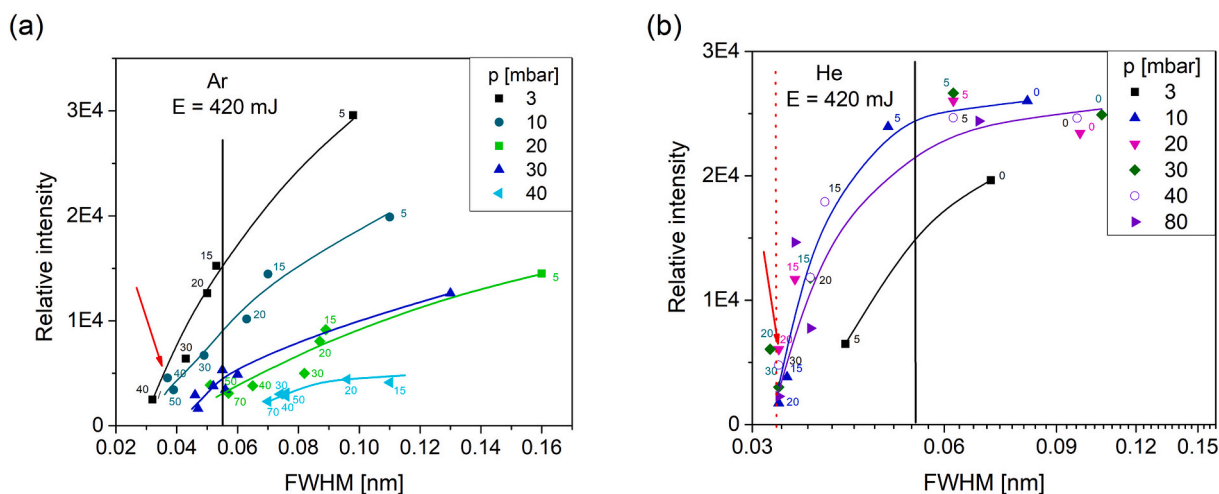


Fig. 9. Dependence of spectral line peak intensity on FWHM for different gas pressures of (a) Ar and (b) He at laser energy 420 mJ. A vertical line represents the maximum spectral line width (0.054 nm) for resolving D_{α} and T_{α} with equal peak intensity. Labels represent the values of delay time for each data point.

width ($FWHM_{cr}$) for resolving deuterium (D_{α}) and tritium (T_{α}) lines by applying Rayleigh criteria and Voigt profile approximations for hydrogen lines. The estimated $FWHM_{cr}$ ranged between 0.054 nm for

equal peak intensities ($R = 1$) and 0.027 nm for $R = 0.1$. An approximate formula for calculating $FWHM_{cr}$ dependency on R was proposed. The study emphasized that fulfilling necessary conditions for resolving D_{α}

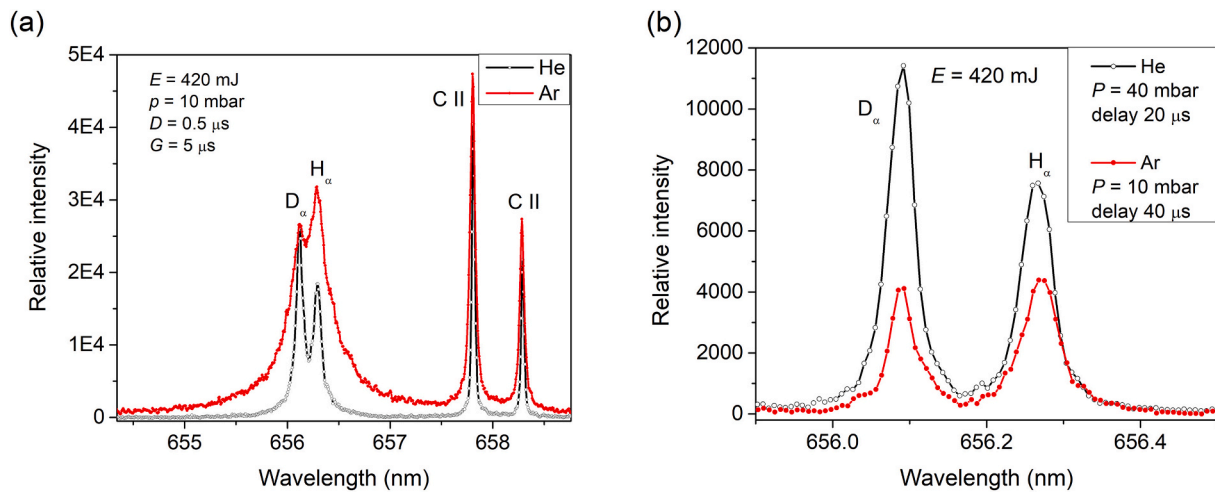


Fig. 10. Comparison of the Balmer alpha line shapes at (a) the beginning of the plasma evolution and at (b) optimal conditions: for He at 40 mbar at a delay 20 μ s and for Ar at 10 mbar at a delay 40 μ s.

and T_{α} required full resolution of H_{α} and D_{α} lines while ensuring the dip between these lines was less than 10 % of the smaller peak intensity.

Experimental validation of the determined conditions essential for resolving T_{α} and D_{α} was conducted using a LIBS setup employing a TEA CO_2 laser and recording plasma emission through an iCCD camera mounted on the spectrometer's exit slit with an instrumental width of 0.03 nm. Tests on hydrogen isotope retention in plasma-facing components were carried out using graphite samples doped with heavy water (D_2O) mixed with silica gel. Plasma parameters were assessed by determining electron number density from the separation between peaks of He I components and inferring temperature from the measured and synthetic segments of the C_2 molecule sequence $\Delta\nu = 0$. In the time frame of 0.5 μ s – 5 μ s, the electron number density was approximately 10^{21} m^{-3} , with plasma temperature around 5000 K and 3500 K for delays of 5 μ s and 20 μ s, respectively.

Spectra of hydrogen and deuterium Balmer alpha lines were obtained using different laser energies under varying experimental conditions in Ar or He atmospheres, impacting line resolution differently. Optimal conditions for plasma induced in He and Ar were identified concerning laser energy, gas pressure, and delay times, resulting in better intensities and signal-to-noise ratios. Resolving D_{α} and H_{α} lines with a dip below 10 % of the smaller peak intensity under optimal conditions showcased the potential for obtaining fully resolved T_{α} and D_{α} lines in both gas atmospheres.

Enhancement of the line intensities by using longer gate times (for recordings when at given delay time, the line width approaches instrumental width) is demonstrated.

CRediT authorship contribution statement

I. Traparic: Writing – review & editing, Investigation, Formal analysis. **D. Rankovic:** Investigation, Formal analysis. **B.D. Stankov:** Investigation, Formal analysis. **J. Savovic:** Writing – review & editing, Visualization, Formal analysis. **M. Kuzmanovic:** Writing – review & editing, Formal analysis. **M. Ivkovic:** Writing – review & editing, Writing – original draft, Supervision, Methodology, Conceptualization.

Declaration of competing interest

The authors declare that they have no known competing financial interests or personal relationships that could have appeared to influence the work reported in this paper.

Data availability

Data will be made available on request.

Acknowledgements

The research was funded by the Ministry of Science, Technological Development and Innovations of the Republic of Serbia, Contract numbers: 451-03-68/2022-14/200024 and 451-03-65/2024-03/200146, and supported by the Science Fund of the Republic Serbia, Grant no. 7753287 “NOVA2LIBS4fusion”. This work was carried out under the project: “Laser induced breakdown spectroscopy for determination of LHD wall composition” (NIFS21KLPP087) within the agreement between NIFS and the University of Belgrade. The authors thank Stanko Milanovic for technical assistance in preparation and setting up the experiment.

References

- [1] Fusion Energy and ITER. https://research-and-innovation.ec.europa.eu/research-area/energy/fusion-energy_en, 2024.
- [2] L. Qiao, X. Zhang, R. He, H. Zhang, E. Fu, P. Wang, Experimental measurement of deuterium concentration and depth profiling in tungsten by radio frequency glow discharge optical emission spectroscopy, *Spectrochim. Acta Part B At. Spectrosc.* 173 (2020) 105975, <https://doi.org/10.1016/j.sab.2020.105975>.
- [3] C. Cupak, E. Pitthan, M.V. Moro, M. Fellingner, D. Primetzhofer, F. Aumayr, Retention of deuterium in beryllium: a combined investigation using TDS, ERDA and EBS, *Nucl. Mater. Energy.* 33 (2022) 101249, <https://doi.org/10.1016/j.nme.2022.101249>.
- [4] M. Yajima, S. Masuzaki, N. Yoshida, M. Tokitani, T. Otsuka, Y. Oya, Y. Torikai, G. Motojima, Investigation on tritium retention and surface properties on the first wall in the large helical device, *Nucl. Mater. Energy.* 27 (2021) 100906, <https://doi.org/10.1016/j.nme.2021.100906>.
- [5] J. Roth, E. Tsitrone, T. Loarer, V. Philipps, S. Brezinsek, A. Loarte, G.F. Counsell, R. P. Doerner, K. Schmid, O.V. Ogorodnikova, R.A. Causey, Tritium inventory in ITER plasma-facing materials and tritium removal procedures, *Plasma Phys. Control. Fusion.* 50 (2008) 103001, <https://doi.org/10.1088/0741-3335/50/10/103001>.
- [6] A.P. Zakharov, A.E. Gorodetsky, V.K. Alimov, S.L. Kanashenko, A.V. Markin, Hydrogen retention in plasma-facing materials and its consequences on tokamak operation, *J. Nucl. Mater.* 241–243 (1997) 52–67, [https://doi.org/10.1016/S0022-3115\(97\)80030-X](https://doi.org/10.1016/S0022-3115(97)80030-X).
- [7] L. Cai, Z. Wang, C. Li, X. Huang, D. Zhao, H. Ding, Development of an in situ diagnostic system for mapping the deposition distribution on plasma facing components of the HL-2M tokamak, *Rev. Sci. Instrum.* 90 (2019), <https://doi.org/10.1063/1.5082630>.
- [8] W. Gonzalez, W. Biel, P. Mertens, M. Tokar, O. Marchuk, C. Linsmeier, Conceptual studies on spectroscopy and radiation diagnostic systems for plasma control on DEMO, *Fusion Eng. Des.* 146 (2019) 2297–2301, <https://doi.org/10.1016/j.fusengdes.2019.03.176>.
- [9] M. Rubel, P. Petersson, E. Alves, S. Brezinsek, J.P. Coad, K. Heinola, M. Mayer, A. Widdowson, The role and application of ion beam analysis for studies of plasma-facing components in controlled fusion devices, *Nucl. Instruments Methods Phys.*

- Res. Sect. B Beam Interact. with Mater. Atoms. 371 (2016) 4–11, <https://doi.org/10.1016/j.nimb.2015.09.077>.
- [10] M. Mayer, S. Möller, M. Rubel, A. Widdowson, S. Charisopoulos, T. Ahlgren, E. Alves, G. Apostolopoulos, N.P. Barradas, S. Donnelly, S. Fazinić, K. Heinola, O. Kakuee, H. Khodja, A. Kimura, A. Lagoyannis, M. Li, S. Markelj, M. Mudrinic, P. Petersson, I. Portnykh, D. Primetzhofer, P. Reichart, D. Ridikas, T. Silva, S. M. Gonzalez de Vicente, Y.Q. Wang, Ion beam analysis of fusion plasma-facing materials and components: facilities and research challenges, Nucl. Fusion 60 (2020) 025001, <https://doi.org/10.1088/1741-4326/ab5817>.
- [11] Y. Oya, H. Fujita, C. Hu, Y. Uemura, S. Sakurada, K. Yuyama, X. Li, Y. Hatano, N. Yoshida, H. Watanabe, Y. Nobuta, Y. Yamauchi, M. Tokitani, S. Masuzaki, T. Chikada, Effect of impurity deposition layer formation on D retention in LHD plasma exposed W, Nucl. Mater. Energy. 9 (2016) 84–88, <https://doi.org/10.1016/j.nme.2016.07.005>.
- [12] V.K. Alimov, M. Yajima, S. Masuzaki, M. Tokitani, Analysis of mixed-material layers deposited on the toroidal array probes during the FY 2012 LHD plasma campaign, Fusion Eng. Des. 147 (2019) 111228, <https://doi.org/10.1016/j.fusengdes.2019.06.001>.
- [13] Y. Oya, C. Hu, H. Fujita, K. Yuyama, S. Sakurada, Y. Uemura, S. Masuzaki, M. Tokitani, M. Yajima, Y. Hatano, T. Chikada, Development of H, D, T simultaneous TDS measurement system and H, D, T retention behavior for DT gas exposed tungsten installed in LHD plasma campaign, Fusion Sci. Technol. 71 (2017) 351–356, <https://doi.org/10.1080/15361055.2017.1291039>.
- [14] A.W. Miziolek, V. Palleschi, I. Schechter, eds. Laser-Induced Breakdown Spectroscopy (LIBS), Cambridge University Press, Cambridge, 2006, <https://doi.org/10.1017/CBO9780511541261>.
- [15] D.A. Cremers, L.J. Radziemski, Handbook of laser-induced breakdown spectroscopy, Wiley (2013), <https://doi.org/10.1002/9781118567371>.
- [16] P.J. Singh, S.N. Thakur (Eds.), Laser-Induced Breakdown Spectroscopy, Elsevier, 2020, <https://doi.org/10.1016/C2018-0-03938-9>.
- [17] R. Noll, Laser-Induced Breakdown Spectroscopy, Springer Berlin Heidelberg, Berlin, Heidelberg, 2012, <https://doi.org/10.1007/978-3-642-20668-9>.
- [18] S. Musazzi, U. Perini, eds. Laser-Induced Breakdown Spectroscopy, Springer, Berlin Heidelberg, Berlin, Heidelberg, 2014, <https://doi.org/10.1007/978-3-642-45085-3>.
- [19] D.W. Hahn, N. Omenetto, Laser-induced breakdown spectroscopy (LIBS), part I: review of basic diagnostics and plasma—particle interactions: still-challenging issues within the analytical plasma community, Appl. Spectrosc. 64 (2010) 335A–336A, <https://doi.org/10.1366/000370210793561691>.
- [20] D.W. Hahn, N. Omenetto, Laser-induced breakdown spectroscopy (LIBS), part II: review of instrumental and methodological approaches to material analysis and applications to different fields, Appl. Spectrosc. 66 (2012) 347–419, <https://doi.org/10.1366/11-06574>.
- [21] C. Li, C.-L. Feng, H.Y. Oederji, G.-N. Luo, H.-B. Ding, Review of LIBS application in nuclear fusion technology, Front. Phys. 11 (2016) 114214, <https://doi.org/10.1007/s11467-016-0606-1>.
- [22] G.S. Maurya, A. Marín-Roldán, P. Veis, A.K. Pathak, P. Sen, A review of the LIBS analysis for the plasma-facing components diagnostics, J. Nucl. Mater. 541 (2020) 152417, <https://doi.org/10.1016/j.jnucmat.2020.152417>.
- [23] H.J. van der Meiden, S. Almaviva, J. Butikova, V. Dwivedi, P. Gasior, W. Gromelski, A. Hakola, X. Jiang, I. Jögi, J. Karhunen, M. Kubkowska, M. Laan, G. Maddaluno, A. Marín-Roldán, P. Paris, K. Piip, M. Pisarcik, G. Sergienko, M. Veis, P. Veis, S. Brezinsek, T. EUROfusion WP PFC team, Monitoring of tritium and impurities in the first wall of fusion devices using a LIBS based diagnostic, Nucl. Fusion. 61 (2021) 125001, <https://doi.org/10.1088/1741-4326/ac31d6>.
- [24] S. Almaviva, L. Caneve, F. Colao, R. Fantoni, G. Maddaluno, Remote-LIBS characterization of ITER-like plasma facing materials, J. Nucl. Mater. 421 (2012) 73–79, <https://doi.org/10.1016/J.JNUCMT.2011.11.050>.
- [25] S. Almaviva, L. Caneve, F. Colao, V. Lazić, G. Maddaluno, P. Mosetti, A. Palucci, A. Reale, P. Gasior, W. Gromelski, M. Kubkowska, LIBS measurements inside the FTU vessel mock-up by using a robotic arm, Fusion Eng. Des. 157 (2020) 111685, <https://doi.org/10.1016/j.fusengdes.2020.111685>.
- [26] D. Zhao, C. Li, Z. Hu, C. Feng, Q. Xiao, R. Hai, P. Liu, L. Sun, D. Wu, C. Fu, J. Liu, N. Farid, F. Ding, G.-N. Luo, L. Wang, H. Ding, Remote in situ laser-induced breakdown spectroscopic approach for diagnosis of the plasma facing components on experimental advanced superconducting tokamak, Rev. Sci. Instrum. 89 (2018), <https://doi.org/10.1063/1.5024848>.
- [27] C. Li, X. Wu, C. Zhang, H. Ding, G. de Temmerman, H.J. van der Meiden, Study of deuterium retention on lithiated tungsten exposed to high-flux deuterium plasma using laser-induced breakdown spectroscopy, Fusion Eng. Des. 89 (2014) 949–954, <https://doi.org/10.1016/J.FUSENGDES.2014.04.071>.
- [28] P. Liu, D.Y. Zhao, L.Y. Sun, C.L. Fu, J.M. Liu, C. Li, R. Hai, C.F. Sang, Z.H. Hu, Z. Sun, J.S. Hu, L. Wang, J.L. Chen, Y.F. Liang, G.N. Luo, H. Ding, In situ diagnosis of Li-wall conditioning and H/D co-deposition on the first wall of EAST using laser-induced breakdown spectroscopy, Plasma Phys. Control. Fusion. 60 (2018) 085019, <https://doi.org/10.1088/1361-6587/aae83>.
- [29] G. Li, H. Hou, P. Ran, Y. Zhao, Z. Zhong, Calibration-free quantitative analysis of D/H isotopes with a fs-laser filament, J. Anal. At. Spectrom. 35 (2020) 1320–1329, <https://doi.org/10.1039/D0JA00062K>.
- [30] M. Burger, P.J. Skrodzki, L.A. Finney, J. Hermann, J. Nees, I. Jovanovic, Isotopic analysis of deuterated water via single- and double-pulse laser-induced breakdown spectroscopy, Phys. Plasmas 25 (2018), <https://doi.org/10.1063/1.5042665>.
- [31] R. Fantoni, S. Almaviva, L. Caneve, F. Colao, G. Maddaluno, P. Gasior, M. Kubkowska, Hydrogen isotope detection in metal matrix using double-pulse laser-induced breakdown-spectroscopy, Spectrochim. Acta B At. Spectrosc. 129 (2017) 8–13, <https://doi.org/10.1016/j.sab.2016.12.008>.
- [32] E.J. Kautz, E.C.E. Rönnebro, A. Devaraj, D.J. Senior, S.S. Harilal, Detection of hydrogen isotopes in zircaloy-4 via femtosecond LIBS, J. Anal. At. Spectrom. 36 (2021) 1217–1227, <https://doi.org/10.1039/D1JA00034A>.
- [33] E.J. Kautz, A. Devaraj, D.J. Senior, S.S. Harilal, Hydrogen isotopic analysis of nuclear reactor materials using ultrafast laser-induced breakdown spectroscopy, Opt. Express 29 (2021) 4936, <https://doi.org/10.1364/OE.412351>.
- [34] S.S. Harilal, A.K. Shaik, E.J. Kautz, A. Devaraj, A.M. Casella, D.J. Senior, Detection of tritium using ultrafast laser-induced breakdown spectroscopy, J. Anal. At. Spectrom. 39 (2024) 699–703, <https://doi.org/10.1039/D3JA00439B>.
- [35] S. Harilal, E.J. Kautz, Analysis of hydrogen and lithium isotopes using laser-induced breakdown spectroscopy, in: C.R. Phipps, V.E. Gruzdev (Eds.), High-Power Laser Ablation VIII, SPIE, 2024, p. 14, <https://doi.org/10.1117/12.3015929>.
- [36] K.H. Kurniawan, T.J. Lie, M.M. Suliyanti, R. Hedwig, M. Pardeed, D.P. Kurniawan, Y. Kusumoto, K. Kagawa, Quantitative analysis of deuterium using laser-induced plasma at low pressure of helium, Anal. Chem. 78 (2006) 5768–5773, <https://doi.org/10.1021/ac060633h>.
- [37] C.W. Forsberg, S. Lam, D.M. Carpenter, D.G. Whyte, R. Scarlat, C. Contescu, L. Wei, J. Stempin, E. Blandford, Tritium control and capture in salt-cooled fission and fusion reactors: status, challenges, and path forward, Nucl. Technol. 197 (2017) 119–139, <https://doi.org/10.13182/NT16-101>.
- [38] A. Kramida, Y. Ralchenko, J. Reader, N.A. Team, NIST At. Spectra Database (2024), <https://doi.org/10.18434/T4W30F> (ver. 5.11).
- [39] M.A. Gigosos, M.Á. González, V. Cardenoso, Computer simulated Balmer-alpha, -beta and -gamma stark line profiles for non-equilibrium plasmas diagnostics, Spectrochim. Acta B At. Spectrosc. 58 (2003) 1489–1504, [https://doi.org/10.1016/S0584-8547\(03\)00097-1](https://doi.org/10.1016/S0584-8547(03)00097-1).
- [40] A. Díaz-Soriano, J.M. Alcaraz-Pelegriña, A. Sarsa, M.S. Dimitrijević, C. Yubero, A simple and accurate analytical model of the stark profile and its application to plasma characterization, J. Quant. Spectrosc. Radiat. Transf. 207 (2018) 89–94, <https://doi.org/10.1016/j.jqsrt.2017.12.027>.
- [41] A. Díaz-Soriano, M.S. Dimitrijević, J.M. Alcaraz-Pelegriña, A. Sarsa, C. Yubero, Simple and analytical function for the stark profile of the H α line and its application to plasma characterization, J. Quant. Spectrosc. Radiat. Transf. 217 (2018) 111–115, <https://doi.org/10.1016/j.jqsrt.2018.05.031>.
- [42] A. Ortiz-Mora, A. Díaz-Soriano, A. Sarsa, M.S. Dimitrijević, C. Yubero, A practical method for plasma diagnosis with Balmer series hydrogen lines, Spectrochim. Acta Part B At. Spectrosc. 163 (2020) 105728, <https://doi.org/10.1016/j.sab.2019.105728>.
- [43] C.O. Laux, T.G. Spence, C.H. Kruger, R.N. Zare, Optical diagnostics of atmospheric pressure air plasmas, Plasma Sources Sci. Technol. 12 (2003) 125–138, <https://doi.org/10.1088/0963-0252/12/2/301>.
- [44] H. Ehrlich, Experimental study of Balmer- α stark broadening, Z. Für Naturforsch. A. 34 (1979) 188–191, <https://doi.org/10.1515/zna-1979-0210>.
- [45] N. Konjević, M. Ivković, N. Sakan, Hydrogen Balmer lines for low electron number density plasma diagnostics, Spectrochim. Acta B At. Spectrosc. 76 (2012) 16–26, <https://doi.org/10.1016/j.sab.2012.06.026>.
- [46] J.J. Olivero, R.L. Longbotham, Empirical fits to the voigt line width: a brief review, J. Quant. Spectrosc. Radiat. Transf. 17 (1977) 233–236, [https://doi.org/10.1016/0022-4073\(77\)90161-3](https://doi.org/10.1016/0022-4073(77)90161-3).
- [47] H.R. Griem, Principles of plasma spectroscopy, in: fast electr. Opt. Meas., Springer Netherlands, Dordrecht, 1986: pp. 885–910. doi:https://doi.org/10.1007/978-94-017-0445-8_34.
- [48] Z. Mijatović, S. Djurović, L. Gavanski, T. Gajo, A. Favre, V. Morel, A. Bultel, Plasma density determination by using hydrogen Balmer H α spectral line with improved accuracy, Spectrochim. Acta Part B At. Spectrosc. 166 (2020) 105821, <https://doi.org/10.1016/j.sab.2020.105821>.
- [49] S. Almaviva, L. Caneve, F. Colao, G. Maddaluno, R. Fantoni, Accessory laboratory measurements to support quantification of hydrogen isotopes by in-situ LIBS from a robotic arm inside a fusion vessel, Spectrochim. Acta Part B At. Spectrosc. 181 (2021) 106230, <https://doi.org/10.1016/j.sab.2021.106230>.
- [50] Y. Yu, J. Hu, Y. Zhao, X. Gao, J. Li, ICRF (ion cyclotron range of frequencies) discharge cleaning with toroidal and vertical fields on east, Plasma Phys. Control. Fusion. 53 (2011) 015013, <https://doi.org/10.1088/0741-3335/53/1/015013>.
- [51] S. Brezinsek, C.P. Dhard, M. Jakubowski, Plasma–surface interaction in the stellarator W7-X: conclusions drawn from operation with graphite plasma-facing components, Nucl. Fusion. 62 (2022) 016006, <https://doi.org/10.1088/1741-4326/ac3508>.
- [52] M. Ivković, M.A. Gonzalez, S. Jovičević, M.A. Gigosos, N. Konjević, A simple line shape technique for electron number density diagnostics of helium and helium-seeded plasmas, Spectrochim. Acta B At. Spectrosc. 65 (2010) 234–240, <https://doi.org/10.1016/j.sab.2010.03.003>.
- [53] M. Ivković, M.A. Gonzalez, N. Lara, M.A. Gigosos, N. Konjević, Stark broadening of the He I 492.2 nm line with forbidden components in dense low-temperature plasma, J. Quant. Spectrosc. Radiat. Transf. 127 (2013) 82–89, <https://doi.org/10.1016/j.jqsrt.2013.04.030>.
- [54] A.J. Barnard, J. Cooper, E.W. Smith, Stark broadening tables for He I $\lambda 4922\text{Å}$, J. Quant. Spectrosc. Radiat. Transf. 15 (1975) 429–437, [https://doi.org/10.1016/0022-4073\(75\)90062-X](https://doi.org/10.1016/0022-4073(75)90062-X).
- [55] A. de Giacomo, J. Hermann, Laser-induced plasma emission: from atomic to molecular spectra, J. Phys. D: Appl. Phys. 50 (2017) 183002, <https://doi.org/10.1088/1361-6463/aa6585>.
- [56] C.M. Western, PGOPHER: a program for simulating rotational, vibrational and electronic spectra, J. Quant. Spectrosc. Radiat. Transf. 186 (2017) 221–242, <https://doi.org/10.1016/j.jqsrt.2016.04.010>.

- [57] B. Stankov, M. Gavrilovic Bozovic, J. Savovic, M. Ivkovic, Spectroscopic characterization of laser-induced plasma on doped tungsten, in: *Publ. Astron. Obs. Belgrade* 102, 2022, pp. 239–242. ISBN:978–86–82296-02-7.
- [58] I. Jögi, J. Ristkok, J. Raud, J. Butikova, K. Mizohata, P. Paris, Laser induced breakdown spectroscopy for hydrogen detection in molybdenum at atmospheric pressure mixtures of argon and nitrogen, *Fusion Eng. Des.* 179 (2022) 113131, <https://doi.org/10.1016/j.fusengdes.2022.113131>.
- [59] N. Larbi-Terzi, S. Sahal-Bréchet, N. Ben Nessib, M.S. Dimitrijević, Stark-broadening calculations of singly ionized carbon spectral lines, *Mon. Not. R. Astron. Soc.* 423 (2012) 766–773, <https://doi.org/10.1111/j.1365-2966.2012.20968.x>.



LIBS depth-profile analysis of W/Cu functionally graded material

M. Ivkovic^{a,*}, J. Savovic^b, B.D. Stankov^a, M. Kuzmanovic^c, I. Traparić^a^a Institute of Physics, University of Belgrade, Belgrade 11080, Serbia^b Vinca Institute of Nuclear Sciences, University of Belgrade, Belgrade 11000, Serbia^c Faculty of Physical Chemistry, University of Belgrade, Belgrade 11158, Serbia

ARTICLE INFO

Keywords:

Laser-induced breakdown spectroscopy, LIBS
W/Cu composite
Functionally graded material, FGM
Quantitative analysis
Depth-profile analysis

ABSTRACT

A feature of Laser-Induced Breakdown Spectroscopy (LIBS), the ability to perform depth profiling, has been exploited to analyze a tungsten-copper functionally graded material (FGM), considered a relevant candidate for components in a nuclear fusion reactor. The proposed method relies on establishing correlations between the depth of ablation craters and the number of laser pulses, along with the accompanying LIBS spectra acquired by varying a number of laser pulses. LIBS measurements were performed using a Q-switched Nd:YAG laser at 532 nm with 100 mJ/pulse energy under reduced Ar pressure. The ablation craters were analyzed using optical profilometry. The copper concentration at each specific depth was assessed using a univariate calibration curve constructed with intensity ratios of Cu I 521.82 nm and W I 522.47 nm spectral lines. The calibration samples were pure W and homogenous W/Cu composite samples with different Cu content (10.9% - 35.3%) whose composition was determined by X-ray fluorescence. The proposed method exhibits potential applicability for quantitative analysis of multilayered materials.

1. Introduction

Functionally Graded Materials (FGM) have innovative properties and multifunctional characteristics that conventional homogeneous materials cannot achieve. In its simplest form, FGM consists of a singular material on one surface, a distinct material on the opposing surface, and an intermediary layer characterized by a gradual variation in structure, composition, and morphology spanning micron-level dimensions between the two materials. A desired function can be achieved by selecting the transition profile of FGM. Therefore, the FGM must be classified separately from conventional homogeneous composites and nanocomposite materials [1–3]. The applications of FGM are extensive and include engineering, aerospace, chemical plants, electronics, energy conversion, optics, nuclear energy, and even biomaterials [4,5]. Depending on the application, various properties, such as thermal (expansion coefficient, conductivity, stability, temperature distribution, response under transient heating), electric (conductivity, dielectric properties), elastic (deformation, strength, Young's elastic modulus), or some other can have one-, two- or three-dimensional variation in the fraction of its components.

Due to their distinctive characteristics, materials with property gradation offer significant advantages for application in nuclear fusion

reactors. For example, functionally graded materials are relevant candidates for the interlayer between W plasma-facing components (PFCs) and CuCrZr heat sinks [6–15]. The challenge posed by a substantial difference in the coefficient of thermal expansion between these two materials, resulting in thermal stress on PFC, can be mitigated by introducing a transition layer consisting of a material characterized by a low thermal expansion rate, high thermal conductivity, and favorable thermomechanical properties. Promising candidates for joining layers of W to CuCrZr are W/Cu composites and W/Cu functionally graded composites [13,14]. The suitability of these materials is reflected in the ability to finely tune their macroscopic properties (microstructure and phase distribution) to attain the desired characteristics.

As an in-situ, non-contact, minimally invasive technique sensitive to light elements, with the limit of detection down to ppm (or even to ppb in some cases), laser-induced breakdown spectroscopy (LIBS) is a promising tool for analyzing plasma-facing components in fusion devices [16]. Various LIBS configurations, using either single pulse (SP-LIBS) or double pulse (DP-LIBS), have been used to explore the optimization of the technique for monitoring compositional alterations in PFCs. These changes may arise due to impurity deposition, erosion, or fuel retention [17–23]. Also, the effect of laser parameters (energy and duration of laser pulse, wavelength) and the effect of atmospheric

* Corresponding author.

E-mail address: ivke@ipb.ac.rs (M. Ivkovic).<https://doi.org/10.1016/j.sab.2024.106874>

Received 26 June 2023; Received in revised form 8 December 2023; Accepted 29 January 2024

Available online 1 February 2024

0584-8547/© 2024 Elsevier B.V. All rights reserved.

conditions on the emission, mass ablation, and plasma parameters have been extensively studied [24–27]. LIBS possesses a competitive advantage over alternative techniques designed for in-depth elemental analysis due to its in-situ and remote analysis capability, which is especially important when analysis has to be performed in hostile environments like nuclear reactors.

This paper presents the research findings on the potential of LIBS for in-depth profiling of W/Cu functionally graded material using a medium-resolution spectrometer. A conventional nanosecond LIBS system was used, and the samples were analyzed under the Ar atmosphere at reduced pressure. The proposed method is based on the correlation of the depth of the ablation craters and gathered LIBS spectra for different number of accumulated laser pulses. The ablation craters were analyzed using optical profilometry. The copper content at each depth was estimated from the constructed calibration curve. For concentration calibration, homogenous W/Cu samples whose composition was determined by X-ray fluorescence were used. Subsequently, a univariate calibration curve was developed utilizing the line intensity ratios of Cu I 521.82 nm and W I 522.47 nm lines.

The proposed approach is also amenable to the analysis of elemental composition and the determination of individual layer thickness in multilayered materials.

2. Experimental

2.1. Samples

A set of tungsten-copper alloys W93Cu7, W90Cu10, W80Cu20, W70Cu30, and pure W in the form of tablets (diameter 10 mm, thickness 1 mm) were obtained from HUBEI FOTMA MACHINERY CO LTD, Wuhan, P. R. China. Since W/Cu samples' trade names represent a rough percentage of the main constituents, the precise composition of the samples was determined using X-ray fluorescence (XRF) analysis. These samples were used as calibration samples for LIBS analysis. A W/Cu functionally graded material (W/Cu FGM), i.e., tungsten with a gradient concentration of copper along the sample thickness direction, was used for LIBS depth-profile analysis. A W/Cu FGM sample was a disc with a 6 mm diameter and thickness of 1 mm.

2.2. XRF spectrometry

A portable XRF Niton XL3t970 GOLDD analyzer (Thermo Fisher Scientific) was used to analyze the composition of W/Cu standards. The instrument is equipped with an X-ray tube, working at a maximum of 50 kV, 200 μ A, and a high-performance semi-conductor detector with a resolution of 185 eV. The spot diameter at the measurement point is

about 3 mm. Depending on the application, the analytical range covers up to 30 elements, from sulfur to uranium. The analysis was carried out using a General Metal Mode calibration (includes elemental analysis of Ba, Sb, Sn, In, Cd, Pd, Ag, Mo, Nb, Zr, Se, Bi, Pb, Pt, Br, Au, Hg, Ta, Hf, Zn, Cu, Ni, Co, Fe, Mn, Cr, V, Ti) for a total time of 60 s (30 s Main filter and 15 s for Low and High filters).

2.3. LIBS setup

Fig. 1a shows a sketch of the focusing head for the basic single-pulse LIBS setup used in this work. A setup consists of the laser (1) mounted on the platform (2) movable vertically (0–380 mm) by the column (3) connected to the second fixed platform (4). The focusing head (5) carries a dichroic bending mirror at 45 degrees, a green diode laser (6) for indicating the position of a focal point, and a focusing mirror mount (which has the possibility for fine focal distance adjustment with accuracy of 10 μ m and the range of ± 10 mm). A laser source (1) was Nd:YAG Quantel Q-smart 450 laser ($\lambda = 532$ nm; energy 100 mJ; 6 ns pulses, frequency 10 Hz). The change in the laser energy density was obtained by varying the distance between the sample and lens with a 10 cm focal length.

The shape, position, and size of the laser beam spot on the target were monitored using the endoscopic camera (8) equipped with six white light-emitting diodes for illumination. The camera has a diameter of 7 mm and a 5 m long light guide connected to the computer. The resolution of the camera is 640 \times 480 pixels.

Fiber optic cable ($\varnothing = 400$ μ m) led the plasma emission collected by the light collector, i.e., fiber adapter Solar LS FA-2 (9), to the entrance of the imaging spectrometer Shamrock 303 Andor. The imaging spectrometer was equipped with the ICCD camera Andor iStar DH720. The camera working in full vertical binning mode (FVB) was triggered at various delays and gate times determined by a digital delay generator (SRS DG535) using the signals from the ICCD camera computer interface and Q switch trigger from the laser (controlled by the remote laser controller) by the help of the digital storage oscilloscope and computer software. Spectral sensitivity calibration of a Shamrock spectrometer system with an Andor iStar DH720 ICCD camera was performed with a calibrated tungsten lamp in the 300–800 nm wavelength range. Instrumental width (w_i) was experimentally determined by fitting a profile of the spectral line emitted from a low-pressure mercury lamp. For entrance slit width of 20 μ m, w_i was 0.11 nm.

A small vacuum chamber (based on KF40 Tee, see Fig. 1b) carrying target was settled on the carrier (Thorlabs, Pitch and roll platform) (7) with the manually adjustable angle, connected to the Thorlabs XY stepper motor translation stage controlled by the computer. After the chosen number of laser pulses, n , the target position (10) was changed to

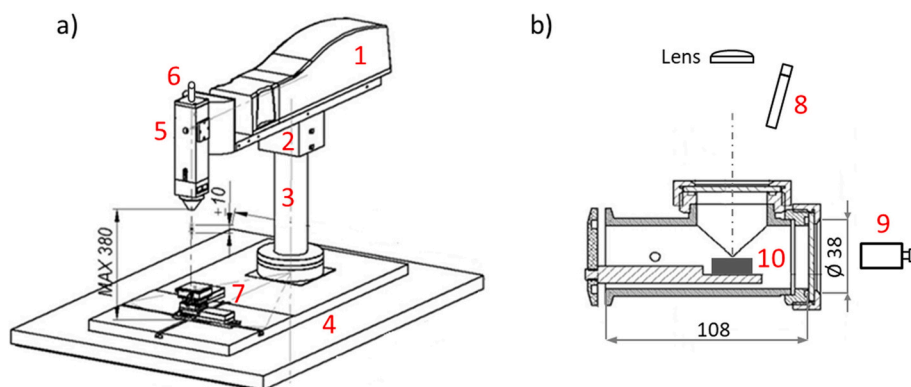


Fig. 1. a) Sketch of the focusing head for the single-pulse LIBS setup showing dimensions and range of the focal point adjustment. Legend: (1) laser, (2) platform, (3) movable column, (4) fixed platform, (5) focusing head, (6) green diode laser, (7) XY translation stage; b) Technical drawing of the vacuum chamber. Legend: (8) endoscopic camera, (9) light collector, i.e., fiber adapter, (10) target. (For interpretation of the references to colour in this figure legend, the reader is referred to the web version of this article.)

expose the “fresh” target surface. The target position was fixed when the task was to determine the ablation depth as a function of the number of applied laser shots. The appropriate gas pressure inside the chamber was adjusted using regulation and needle valves and monitored by the manometer, led to the chamber using appropriate tubing, and evacuated by the vacuum pump. All measurements reported in this work were recorded under reduced Ar pressure.

2.3.1. Profilometry analysis

The Zygo New View 7100 Scanning White Light Interferometer (optical Surface profiler) was used for fast, non-contact 3D measurement of surface morphology. The profilometer’s vertical scan range is 150 μm , with the extended scan range up to 20 mm. Vertical resolution is <0.1 nm, while the lateral resolution is objective dependent and ranges from 0.36 to 9.5 μm . A data scan rate is user-selectable (camera and scan mode dependent) and goes up to 26 $\mu\text{m}/\text{s}$. RMS repeatability is <0.01 nm. The step height accuracy is $\leq 0.75\%$, while repeatability is $\leq 0.1\%$. The profilometer is equipped with the program (Zygo corporation, Metro Pro) that was used for measuring crater depths from two-dimensional (2D) profiles and their three-dimensional (3D) visualization.

3. Results and discussions

3.1. XRF spectroscopy

The composition of the W/Cu calibration standards was determined by XRF analysis. A part of the obtained XRF spectra is presented in Fig. 2. The elemental composition obtained by XRF is summarised in Table 1. Samples also contain trace levels of other elements, such as Ti, Mn, Fe, and Co. The measurement accuracy (element dependent) was typically 2% - 5% of the reported weight percent value. Concentration values obtained by XRF were used to construct the calibration curve.

3.2. LIBS analysis

A critical problem with the application of LIBS for the elemental (quantitative) analysis of W and W-alloys is the low reproducibility of the spectral line intensities caused by different grain sizes in a tungsten structure [28]. The line intensities also depend on grain distribution, causing differences in measured intensities during target irradiation at different angles [29]. In addition, explosive boiling occurs at temperatures greater than critical [30–32]. For example, threshold laser intensity for phase explosion in tungsten under interaction with Nd:YAG laser at 355 nm was estimated to be $6 \times 10^{10} \text{ W cm}^{-2}$ [31].

Our first step was to study the influence of different experimental parameters (e.g., gas pressure, laser energy, beam size, the number of accumulated pulses, and delay time) on the reproducibility of the

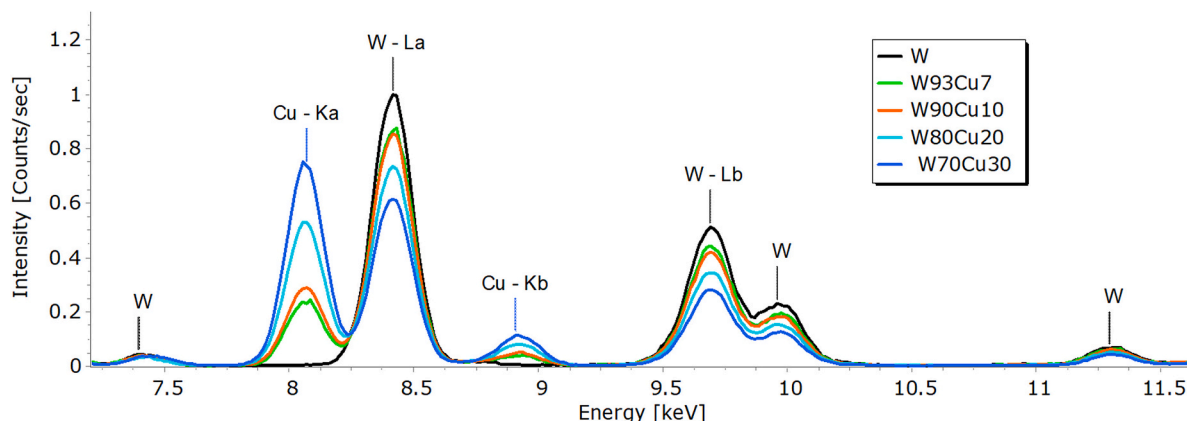


Fig. 2. Segment of the XRF spectra of W and W/Cu samples used as calibration standards for LIBS.

Table 1

Results of the XRF analysis of W/Cu calibration samples.

Trade name	Concentration (wt%)*					Other elements
	Cu	W	Zn	Ni	Cr	
W	–	100	–	–	–	–
W93Cu7	10.9	87	1.6	0.47	–	0.03
W90Cu10	12.9	84	1.9	0.56	0.23	0.41
W80Cu20	24.3	72	2.8	0.78	–	0.12
W70Cu30	35.3	59	3.0	1.5	0.11	1.09

measured spectral line intensities. All LIBS measurements reported in this study were done in an argon atmosphere, as it was shown that the inert background gas provides almost uniform spatial distributions of plasma temperature and densities [33,34].

3.2.1. Optimization of the LIBS experimental parameters

The influence of Ar pressure on the spectral emission intensity was studied within the pressure range spanning from vacuum conditions to 1 atm. Fig. 3 shows that, in the analyzed pressure range, the highest signal-to-noise ratio (SNR) of spectral lines was obtained at 10 mbar, hence this pressure was chosen as optimal.

The influence of delay time on the intensity of Cu I 521.82 nm and W 522.47 nm lines is illustrated in Fig. 4 (a), while the SBR and signal-to-noise ratio (SNR) for a copper 521.82 nm line is illustrated in Fig. 4 (b).

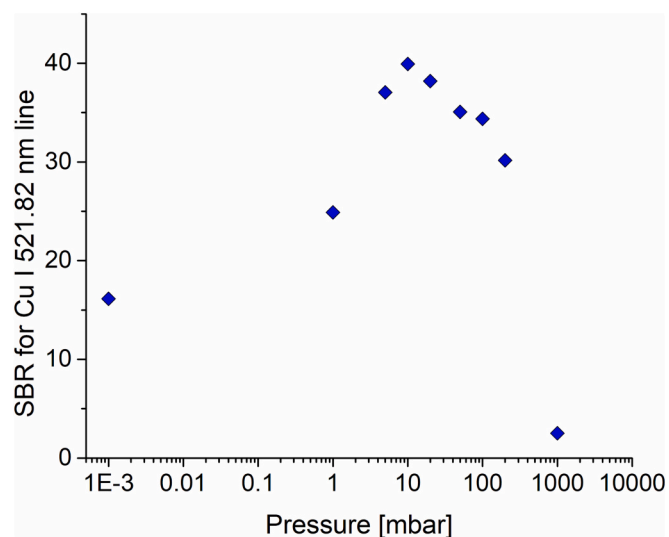


Fig. 3. The influence of Ar pressure on the signal-to-background ratio of Cu 521.82 nm line.

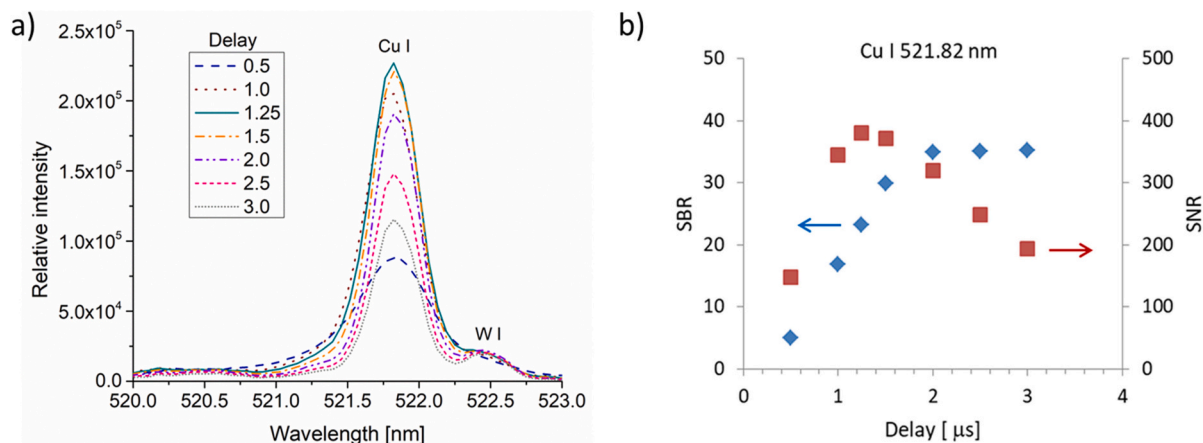


Fig. 4. (a) LIBS spectra of W93Cu7 showing Cu I 521.82 nm and W I 522.47 nm lines recorded for different gate delay times. Laser energy 100 mJ, gate 20 ns, spot diameter 1 mm. Each spectrum represents an average of ten measurements consisting of 10 accumulated consequent laser shots. (b) The SNR and the SBR of Cu I 521.82 nm line, as a function of the delay time.

The highest SBR and SNR values were obtained for a delay time of around 1.5–2 μs.

The laser pulse energy threshold required for creating plasma usable for spectrochemical analysis was determined to be 30 mJ. As shown in Fig. 5, the intensity of W and Cu demonstrated a proportional increase with elevated laser energy. Nevertheless, when the beam is focused on the target and the laser energy surpasses 50 mJ, the ratio of line intensities (Cu I 521.82 nm / W I 522.47 nm) remains constant. Uniform evaporation of both components was achieved at energies exceeding 50 mJ, resulting in a constant line intensity ratio at higher laser pulse energies. A laser energy of 100 mJ was chosen for further LIBS measurements to enhance emission intensity, thereby improving the precision of intensity measurements and increasing the ablated mass compared to a pulse energy of 50 mJ (for the same spot diameter).

The spot size required optimization to ensure that the spot diameter remains significantly larger than the sample grain size. The spot size was optimized by adjusting the focus, specifically by varying the lens-to-sample distance to define the surface that would be ablated. Due to the granulation of the material, the minimal preferable spot size should be above 100 μm. A spot size of 1 mm eliminated a problem with inhomogeneous grain size distribution and reduced spectral intensity

fluctuations.

The minimum number of laser shots needed to obtain reproducible spectral line intensities was determined to be 10. For the laser pulse energy of 100 mJ, the spot size of 1 mm, and 100 shots (average of ten measurements of 10 accumulated consequent laser shots), the relative standard deviation of the intensity ratio of the selected Cu and W lines was around 5%.

Because the measured line intensities may vary due to the interaction of the plasma with the crater walls, the plasma confinement, or plasma cooling by the crater walls, the influence of crater depth on the measured LIBS intensity was also investigated. Fig. 6 (a) shows spectra recorded for a sequence (1–800) of laser shots applied to the same spot on the W90Cu10 target. The effect of the crater depth on the intensity of Cu I 521.82 nm and W I 522.47 nm line and Cu/W intensity ratio is shown in Figs. 6 (b–d). The variation of the line intensities is more pronounced than the variation of the Cu/W intensity ratio. After the 100th shot at the same position, the influence on the measured Cu/W intensity ratio is significant, i.e., it decreases with a further increase of the crater depth. A possible explanation for such behavior could be a more significant effect of the changed plasma parameters (caused by crater walls) on the intensity of the line with lower excitation energy.

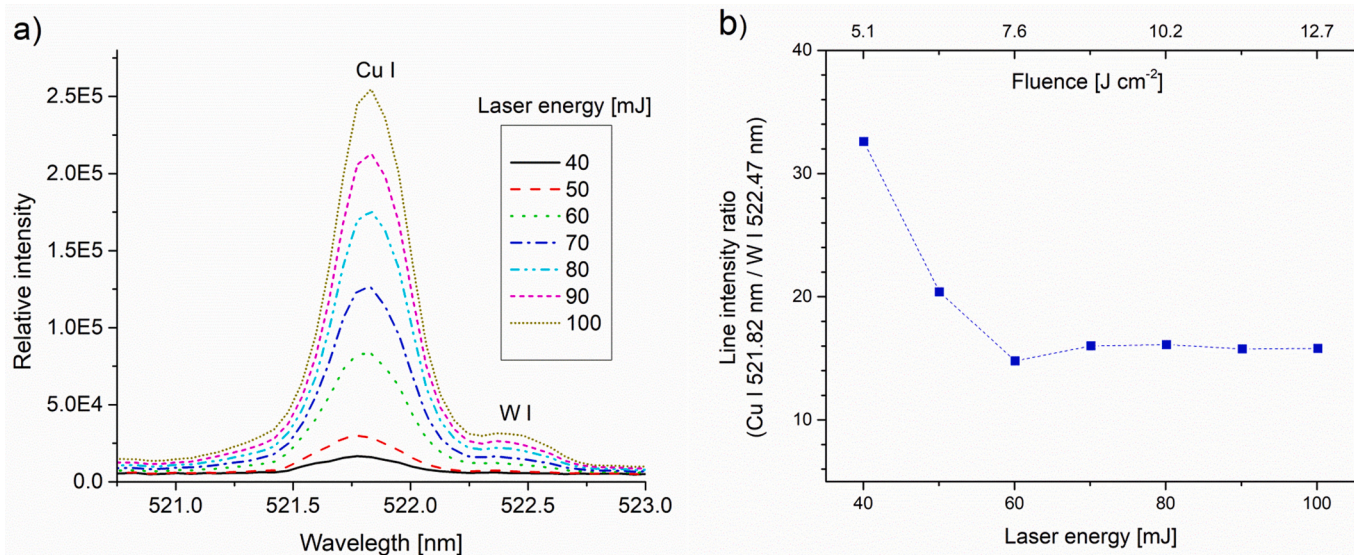


Fig. 5. (a) Effect of laser pulse energy on the LIBS emission of Cu I 521.82 nm and W 522.47 nm line. (b) The influence of pulse energy and fluence on the Cu/W line intensity ratio. Target W93Cu7; delay 1.5 ms; gate 20 ns; spot diameter 1 mm.

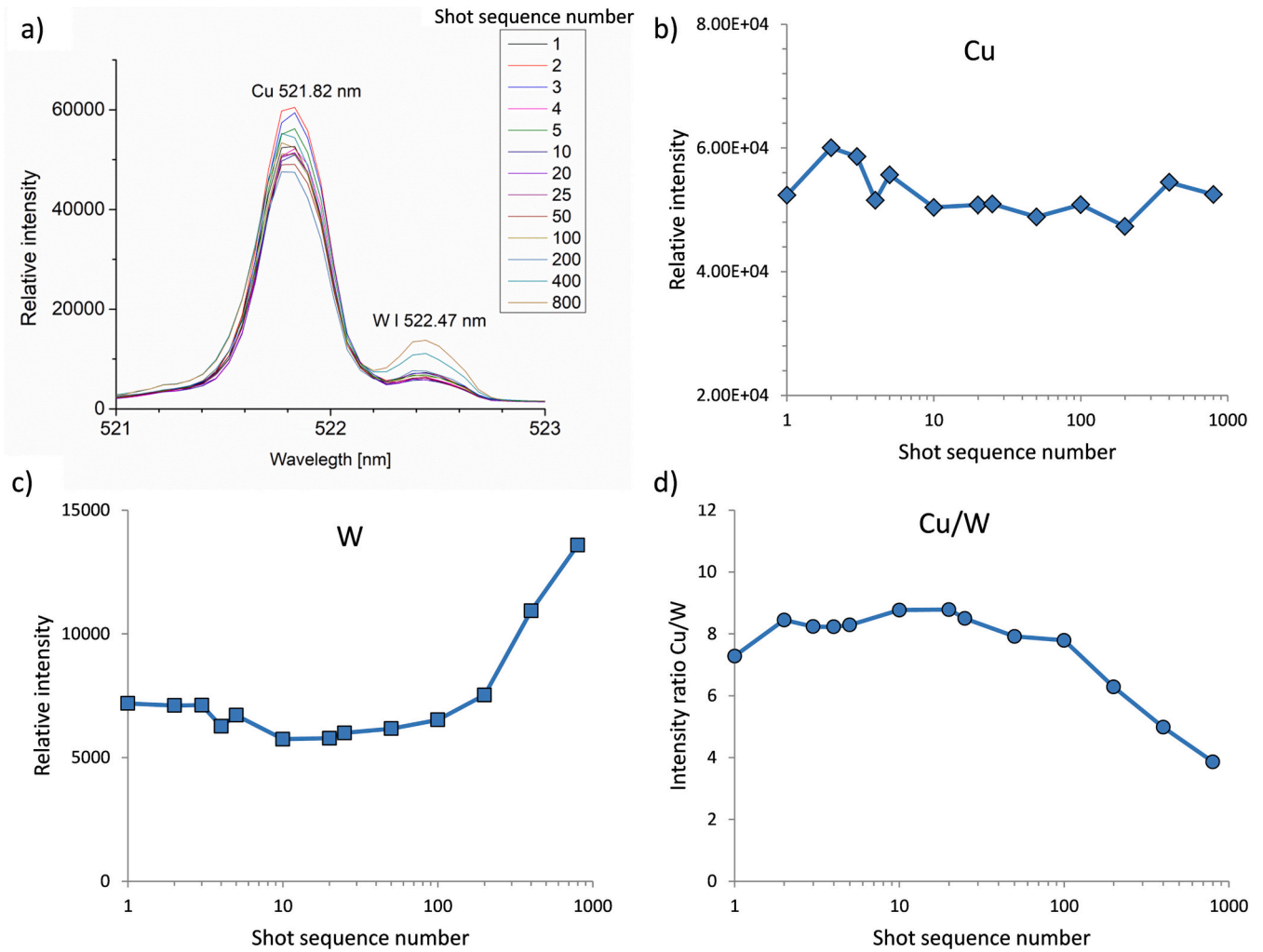


Fig. 6. (a) LIBS spectra recorded for a sequence (1–800) of laser shots applied to the same spot on the W90Cu10 target. (b-d) The effect of the crater depth on the intensity of Cu I 521.82 nm and W I 522.47 nm line and Cu/W intensity ratio.

Therefore, the influence of crater depth on the measured Cu/W intensity ratio was negligible for the number of pulses applied in this work.

3.2.2. Plasma diagnostics

LIBS spectrum recorded for the W70Cu30 sample was used to determine the excitation temperature from the Boltzmann plot of the selected W and Cu spectral lines. In order to cover a large spectral

window (320 nm to 550 nm), several consecutive LIBS spectra were recorded, each covering a spectral portion of about 60 nm. The experimental parameters (laser energy, focusing, delay and gate time, and the number of accumulations) were held constant. Under our experimental conditions, only lines generated by neutral and single ionized W and Cu species can be detected. The list of lines and their spectral parameters (taken from the NIST Atomic Spectral Database [35]) are given in the

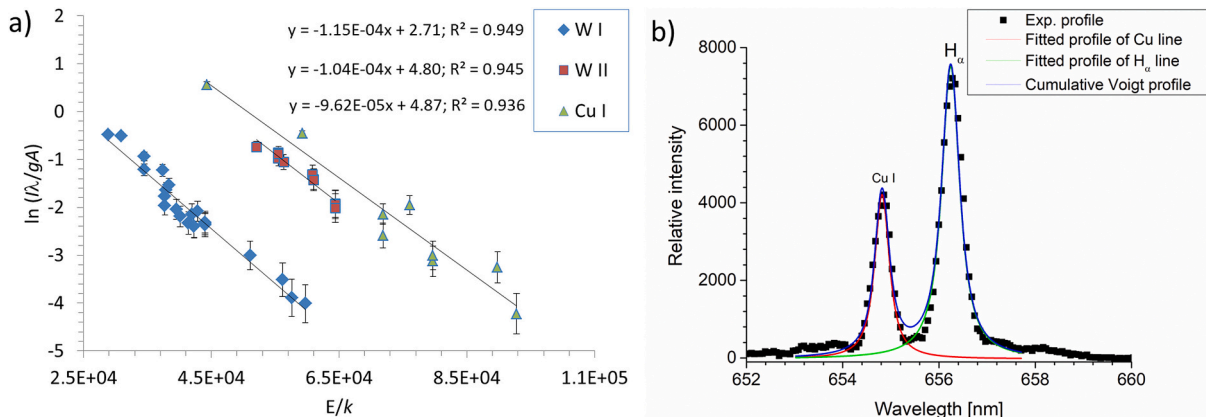


Fig. 7. a) Boltzmann plot of Cu and W spectral lines, and b) Experimental profile of the H α line fitted to a Voigt function.

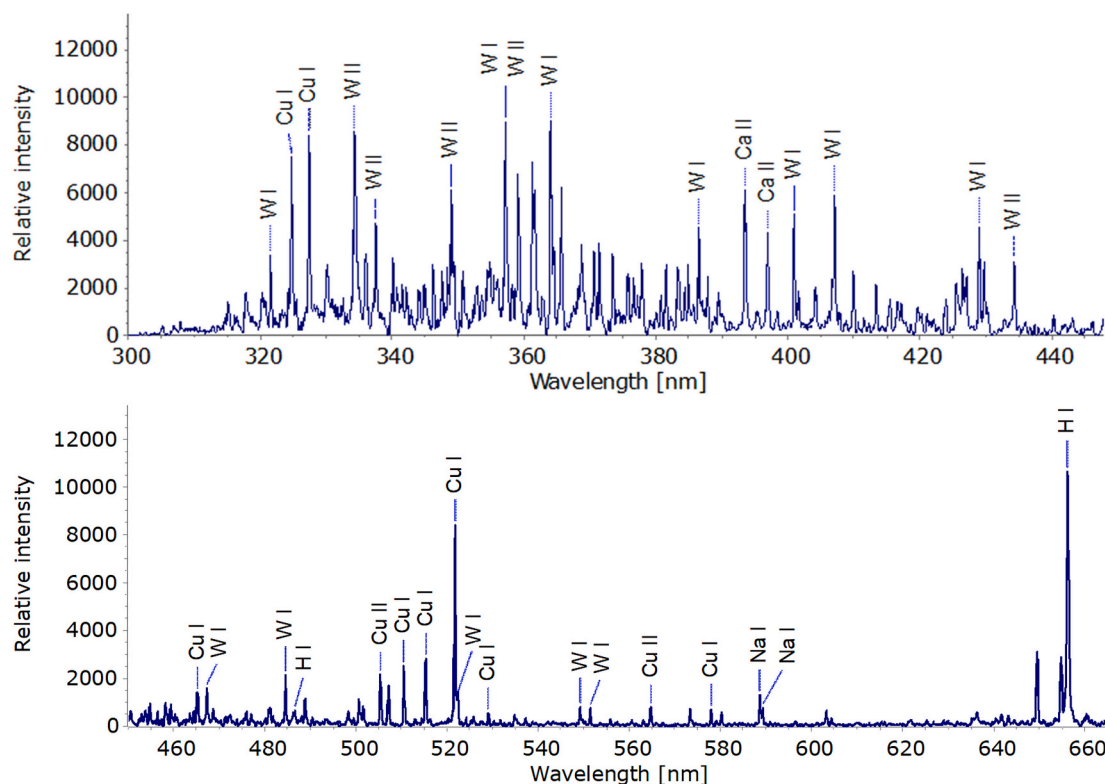


Fig. 8. LIBS spectra of the W93Cu7 alloy sample. Experimental conditions: Nd:YAG pulse energy 40 mJ; wavelength 532 nm; frequency 10 Hz; delay 0.5 μ s; gate 2.5 μ s; 10 mbar argon.

Appendix. The temperatures obtained from Boltzmann plots (Fig. 7a) were 8900 K, 9400 K, and 10,400 K for W I, W II, and Cu I, respectively. A Boltzmann plot using copper ionic lines was omitted because it had poor calculation accuracy of the plasma temperature due to a low number of identified Cu II spectral lines.

The electron number density was determined from the Stark width of the Balmer alpha line of the hydrogen, which is always present in the tungsten as an impurity (Fig. 7b). This line was chosen due to the low Balmer beta line intensity caused by the small amount of hydrogen. The line width was determined under the approximation that the line profile can be described with a Voigt function. The deconvolution of a Voigt function was performed using the Levenberg-Marquardt nonlinear fitting algorithm for minimum squares, with the Gaussian FWHM fixed, assuming that the Lorentzian component, w_L , is due to Stark broadening. The Gaussian fraction (w_G) is assumed to be a combination of the instrumental (w_i) and the Doppler broadening (w_D): $w_G = (w_D^2 + w_i^2)^{0.5} = (0.05^2 + 0.11^2)^{0.5} = 0.12$ nm. To calculate N_e , an approximate formula was used [36,37]:

$$N_e [m^{-3}] = 10^{23} \cdot \left(\frac{w_L [nm]}{1.098} \right)^{1.47135}$$

The estimated value of N_e was $2.5 \times 10^{22} m^{-3}$.

3.2.3. Univariate calibration

Characteristic spectra of the W/Cu composite sample in the 300–660

nm spectral range are shown in Fig. 8.

The possible influence of self-absorption was checked by comparing the experimental and theoretical ratios of line strengths within multiplets [38]. Based on the results shown in Table 2, it was concluded that the influence of self-absorption on the measured intensities of W and Cu lines could be neglected.

LIBS spectra of pure W and four W/Cu composite samples (Table 1) were used to construct a calibration curve. The spectra were recorded using the standard LIBS setup described in the experimental section using an optimized set of parameters: pulse energy 100 mJ; spot diameter 1 mm; delay 2 μ s; gate 20 ns; 100 accumulations (average of ten measurements of 10 accumulated consequent laser shots). LIBS spectra of calibration samples are shown in Fig. 9 a.

Because the selected Cu and W lines overlap, integral intensities of these lines were determined using their approximation with Voigt functions. The line fit was performed using the Levenberg-Marquardt nonlinear fitting algorithm for minimum squares, with the Gaussian FWHM fixed ($w_i = 0.11$ nm). The calculated contribution of Doppler broadening was negligible for temperatures around 10,000 K, 0.005 nm for the Cu 521.82 nm line, and 0.003 for the W 522.47 nm line. The selected line pair was suitable for the Cu concentration range considered in this study. For samples with a low concentration of Cu, the intensity ratio of the strongest Cu I line at 324.75 nm with some of the nearby W lines (e.g., W I 320.72 nm) may be used.

A linear relationship was obtained between the Cu I 521.82 nm and

Table 2

Comparison of theoretical and experimental ratios of spectral line intensities.

	Configuration	λ_1 (nm)/ λ_2 (nm)	$R = I_{\lambda_1}/I_{\lambda_2}$ (theor.)	$R = I_{\lambda_1}/I_{\lambda_2}$ (exp.)
W I	5d46s2 - 5d5(6S)6p	413.74 / 407.06	2.11	2.10
		436.48 / 407.06	0.32	0.29
Cu I	3d94s2 - 3d104p	510.55 / 578.21	2.42	2.27
		3d104p - 3d104d	515.32 / 521.82	0.53

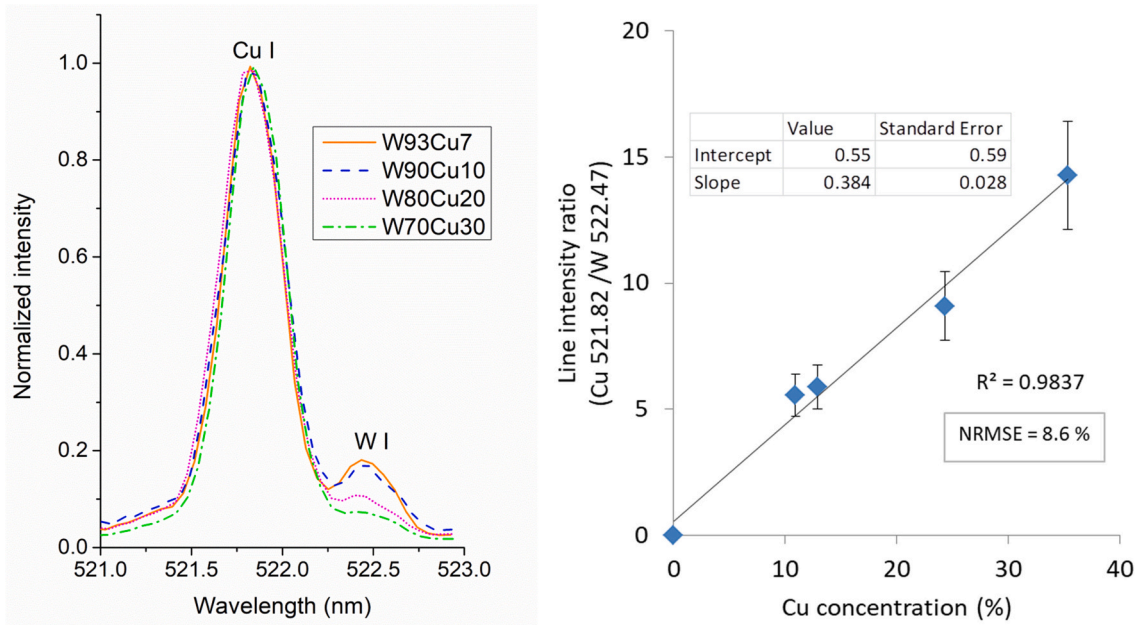


Fig. 9. (a) LIBS spectrum of W/Cu composites; (b) Calibration curve for Cu from the ratio $I_{Cu\ 1}/I_{W\ 1}$.

W I 522.46 nm line intensity ratio and the Cu concentration (Fig. 9 b). The calibration curve prediction error, calculated as a Root Mean Square Error (RMSE), was 0.598. The normalized value of the RMSE was 8.6%.

3.3. LIBS depth-profile analysis

A W/Cu functionally graded material (W/Cu FGM), i.e., tungsten with infiltrating copper along the sample thickness direction, was exposed to a variable number of Nd:YAG laser pulses. Time-resolved LIBS spectra were recorded to monitor the corresponding W and Cu spectral line intensity changes. The proposed depth profile analysis method was performed by combining the LIBS spectral analysis with the

results of 3D-optical profilometry used to establish the depth of the ablation craters [39]. Fig. 10 shows 3D surface profiles of craters created on a W/Cu target after the increasing number of laser pulses irradiated the same spot on the target.

Corresponding 2D cross-sectional profiles used to evaluate the depth of the craters are shown in Fig. 11 a. A relationship between the number of laser pulses and crater depths is shown in Fig. 11 b.

As seen in Fig. 11 a, the paraboloid function describes the crater shape well. The volume of a paraboloid is given by $V = 1/2 \pi r^2 h$, where r is the radius of the circular “cap” of the paraboloid and h is the axial height of the paraboloid. In our case, the radius of the surface damaged area was taken as r and the crater depth as h . Using this equation, the

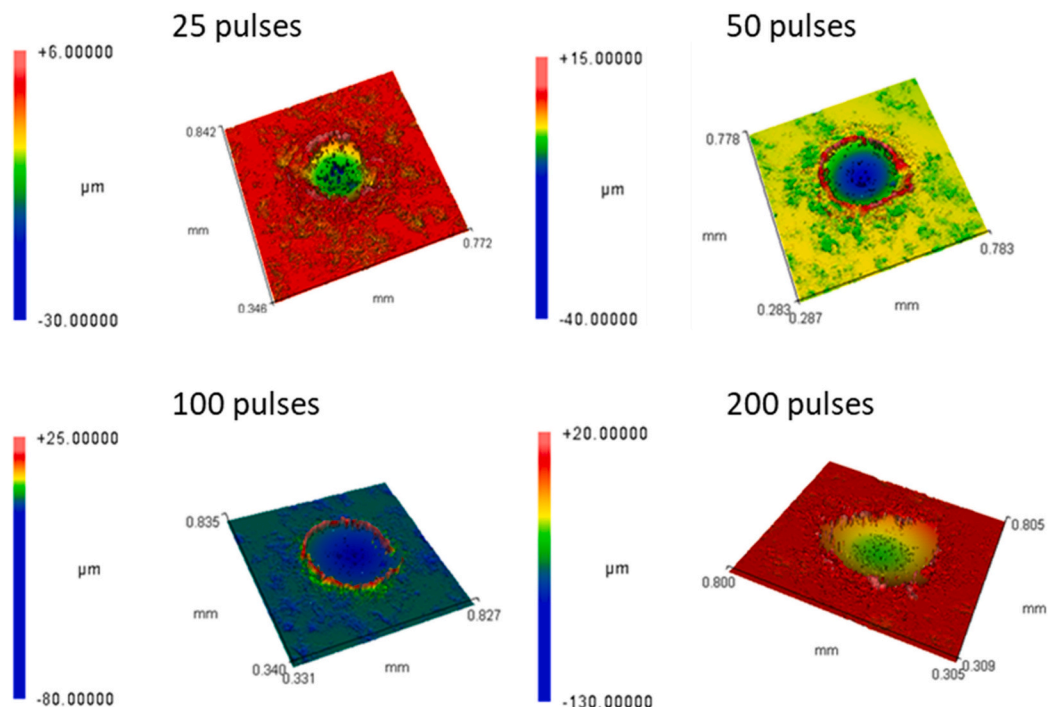


Fig. 10. Surface map of the W/Cu FGM target exposed to a different number of laser pulses.

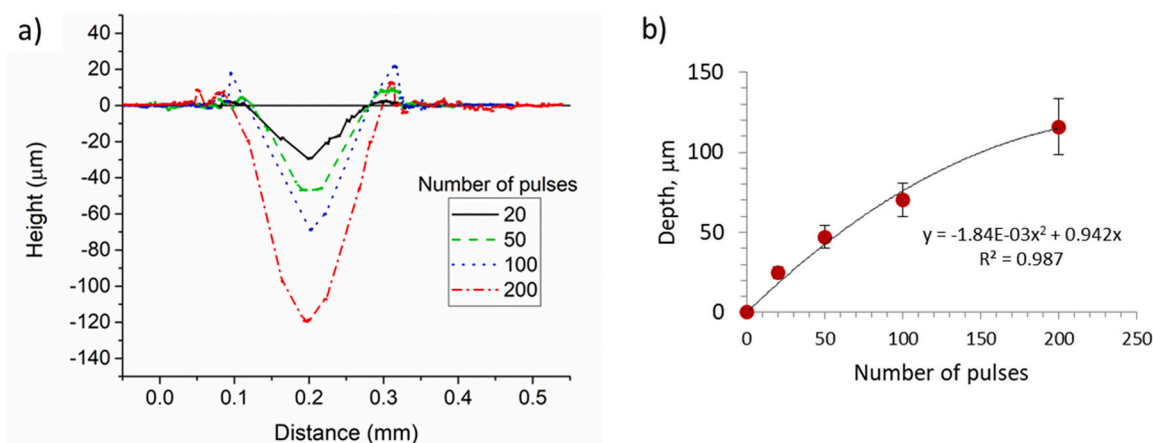


Fig. 11. (a) 2D profile of craters created on W/Cu target by a different number of laser pulses. (b) Crater depth as a function of the number of applied laser pulses.

Table 3
Characteristic parameters of craters created on W/Cu FGM target.

Number of pulses	Spot diameter (mm)	Crater depth (μm)	Spot surface area (10^{-4} cm^2)	Crater volume (10^{-7} cm^3)	Ablated mass* (μg)
25	0.16	29	2.0	3.0	5.7
50	0.16	47	2.0	4.8	9.2
100	0.16	69	2.0	6.9	13
200	0.20	120	3.1	19	36

* Calculated using tungsten density of 19.28 g/cm^3 .

volume of the ablated material was calculated. Characteristic parameters of craters used to estimate the ablated volume and mass of the ablated material are given in Table 3.

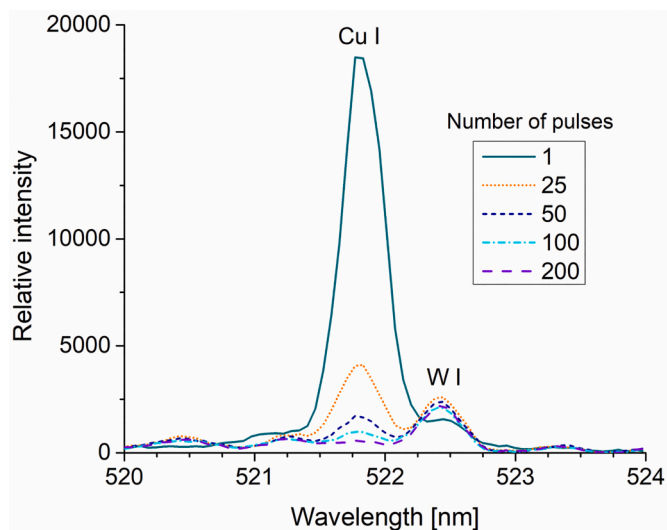


Fig. 12. LIBS spectra of a W/Cu-based gradient material. Laser energy 40 mJ; spot diameter 0.16 mm; delay 0.5 μs ; gate 2.5 μs ; 10 mbar argon.

Table 4
Copper content at different depths of the W/Cu FGM sample.

Number of laser shots	Depth (μm)	Intensity ratio Cu I 521.82/W I 522.46	Cu concentration (%)
1	0.9	12	30 ± 3
25	29	1.5	2.0 ± 0.2
50	47	0.7	0.39 ± 0.03
100	120	–	–

LIBS spectra of a W/Cu target irradiated by an increasing number of laser pulses applied to the same target spot are shown in Fig. 12. As the figure shows, the intensity of a copper spectral line at 521.82 nm decreases with the increasing number of applied laser pulses, suggesting copper content gradually reduces from the top. The line disappeared from the spectra after 200 laser shots, indicating the complete removal of a layer containing a gradient concentration of Cu. Based on the obtained results, we estimated the depth of inbound copper into tungsten to $\sim 120 \mu\text{m}$. The copper concentrations at different depths were estimated from the calibration curve (Fig. 9 b) using a measured Cu I 521.82 nm and W I 522.46 nm line intensity ratios. The results are shown in Table 4.

4. Conclusion

The results have shown that a standard LIBS setup based on Nd:YAG laser using a medium spectral resolution spectrometer can be successfully applied to quantitative analysis of W/Cu functionally graded materials relevant to fusion technology.

For the W/Cu composite with Cu in the 10.9% - 35.3% concentration range, a linear relationship was found between Cu I 521.82 nm to W I 522.46 nm spectral line intensity ratio and Cu concentration. Under optimized experimental conditions (fluence, delay and gate time, number of accumulations), the selected W and Cu lines used to construct a calibration curve were optically thin.

It should be noted that the suitability of the W/Cu samples selected

for the calibration technique should be carefully checked. Depending on the manufacturing processes, the grain size, shape of grains, distribution of additives inside the tungsten matrix, or other characteristics of W-based composites may influence the accuracy of LIBS analysis.

The copper concentration along the sample thickness direction was obtained by combining LIBS spectral analysis and optical profilometry results. The applied protocol may be suitable for depth profile analysis of tungsten-based composite in the fusion reactor, i.e., a transition layer between W tiles at the first wall of the reactor and cooling channels made of CuCrZr.

CRedit authorship contribution statement

M. Ivkovic: Conceptualization, Methodology, Supervision, Writing – original draft, Writing – review & editing. **J. Savovic:** Formal analysis, Visualization, Writing – review & editing. **B.D. Stankov:** Formal analysis, Investigation, Writing – review & editing. **M. Kuzmanovic:** Methodology, Validation, Writing – review & editing. **I. Trparic:** Formal analysis, Writing – review & editing.

Declaration of competing interest

The authors declare that they have no known competing financial interests or personal relationships that could have appeared to influence the work reported in this paper.

Data availability

Data will be made available on request.

Acknowledgements

The research was funded by the Ministry of Science, Technological Development and Innovation of the Republic of Serbia, Contract numbers: 451-03-47/2023-01/200024, 451-03-47/2023-01/200017 and 451-03-47/2023-01/200146, and supported by the Science Fund of the Republic Serbia, Grant no. 7753287.

Appendix A. Supplementary data

Supplementary data to this article can be found online at <https://doi.org/10.1016/j.sab.2024.106874>.

References

- M. Niino, T. Hirai, R. Watanabe, Functionally gradient materials. In pursuit of super heat resisting materials for spacecraft, *J. Japan Soc. Compos. Mater.* 13 (1987) 257–264, <https://doi.org/10.6089/jscm.13.257>.
- A. Kawasaki, R. Watanabe, Concept and P/M fabrication of functionally gradient materials, *Ceram. Int.* 23 (1997) 73–83, [https://doi.org/10.1016/0272-8842\(95\)00143-3](https://doi.org/10.1016/0272-8842(95)00143-3).
- M. Naebe, K. Shirvanimoghaddam, Functionally graded materials: a review of fabrication and properties, *Appl. Mater. Today* 5 (2016) 223–245, <https://doi.org/10.1016/j.apmt.2016.10.001>.
- Y. Miyamoto, W.A. Kaysser, B.H. Rabin, A. Kawasaki, R.G. Ford (Eds.), *Functionally Graded Materials*, Springer US, Boston, MA, 1999, <https://doi.org/10.1007/978-1-4615-5301-4>.
- K. Ichikawa (Ed.), *Functionally Graded Materials in the 21st Century*, Springer US, Boston, MA, 2001, <https://doi.org/10.1007/978-1-4615-4373-2>.
- S. Suzuki, M. Akiba, M. Araki, K. Yokoyama, Thermal cycling experiments of Monoblock Divertor modules for fusion experimental reactors, *Fusion Technol.* 21 (1992) 1858–1862, <https://doi.org/10.13182/FST92-A29989>.
- Y. Itoh, M. Takahashi, H. Takano, Design of tungsten/copper graded composite for high heat flux components, *Fusion Eng. Des.* 31 (1996) 279–289, [https://doi.org/10.1016/0920-3796\(95\)00432-7](https://doi.org/10.1016/0920-3796(95)00432-7).
- G. He, K. Xu, S. Guo, X. Qian, Z. Yang, G. Liu, J. Li, Preparation of tungsten fiber reinforced-tungsten/copper composite for plasma facing component, *J. Nucl. Mater.* 455 (2014) 225–228, <https://doi.org/10.1016/j.jnucmat.2014.05.026>.
- S. Wang, J. Li, Y. Wang, X. Zhang, R. Wang, Y. Wang, J. Cao, Thermal damage of tungsten-armored plasma-facing components under high heat flux loads, *Sci. Rep.* 10 (2020) 1359, <https://doi.org/10.1038/s41598-020-57852-8>.
- A.V. Muller, D. Ewert, A. Galatanu, M. Milwich, R. Neu, J.Y. Pastor, U. Siefken, E. Tejado, J.H. You, Melt infiltrated tungsten–copper composites as advanced heat sink materials for plasma facing components of future nuclear fusion devices, *Fusion Eng. Des.* 124 (2017) 455–459, <https://doi.org/10.1016/j.fusengdes.2017.01.042>.
- R. Neu, J. Riesch, A.V. Müller, M. Balden, J.W. Coenen, H. Gietl, T. Höschen, M. Li, S. Wurster, J.-H. You, Tungsten fibre-reinforced composites for advanced plasma facing components, *Nucl. Mater. Energy.* 12 (2017) 1308–1313, <https://doi.org/10.1016/j.nme.2016.10.018>.
- J.H. You, E. Visca, T. Barrett, B. Bösowirth, F. Crescenzi, F. Domptail, M. Fursdon, F. Gallay, B.-E. Ghidersa, H. Greuner, M. Li, A.V. Müller, J. Reiser, M. Richou, S. Roccella, C. Vorpahl, European divertor target concepts for DEMO: design rationales and high heat flux performance, *Nucl. Mater. Energy.* 16 (2018) 1–11, <https://doi.org/10.1016/j.nme.2018.05.012>.
- Z.-J. Zhou, S.-X. Song, J. Du, Z.-H. Zhong, C.-C. Ge, Performance of W/cu FGM based plasma facing components under high heat load test, *J. Nucl. Mater.* 363–365 (2007) 1309–1314, <https://doi.org/10.1016/j.jnucmat.2007.01.184>.
- E. Tejado, M. Dias, J.B. Correia, T. Palacios, P.A. Carvalho, E. Alves, J.Y. Pastor, New WC-cu thermal barriers for fusion applications: high temperature mechanical behaviour, *J. Nucl. Mater.* 498 (2018) 355–361, <https://doi.org/10.1016/j.jnucmat.2017.10.071>.
- C. Li, D. Zhu, R. Ding, B. Wang, J. Chen, B. Gao, Y. Lei, Characterization on the melting failure of CuCrZr cooling tube of W/cu monoblocks during plasma operations in EAST, *Nucl. Mater. Energy.* 25 (2020) 100847, <https://doi.org/10.1016/j.nme.2020.100847>.
- D.W. Hahn, N. Omenetto, Laser-induced breakdown spectroscopy (LIBS), part II: review of instrumental and methodological approaches to material analysis and applications to different fields, *Appl. Spectrosc.* 66 (2012) 347–419, <https://doi.org/10.1366/11-06574>.
- S. Almaviva, L. Caneve, F. Colao, V. Lazic, G. Maddaluno, P. Masetti, A. Palucci, A. Reale, P. Gasior, W. Gromelski, M. Kubkowska, LIBS measurements inside the FTU vessel mock-up by using a robotic arm, *Fusion Eng. Des.* 157 (2020) 111685, <https://doi.org/10.1016/j.fusengdes.2020.111685>.
- A. Favre, V. Morel, A. Bultel, G. Godard, S. Idlahcen, A. Benyagoub, I. Monnet, A. Sémérok, M. Dinescu, S. Markelj, P. Magaud, C. Grisolia, Double pulse laser-induced plasmas on W and Al by ps-LIBS: focus on the plasma-second pulse interaction, *Fusion Eng. Des.* 168 (2021) 112364, <https://doi.org/10.1016/j.fusengdes.2021.112364>.
- A. Marín Roldán, M. Pisarcík, M. Veis, M. Držík, P. Veis, Calibration-free analysis of a tungsten-based target for diagnostics of relevant fusion materials comparing picosecond and nanosecond LIBS, *Spectrochim. Acta - Part B at Spectrosc.* 177 (2021) 106055, <https://doi.org/10.1016/j.sab.2020.106055>.
- P. Liu, D.Y. Zhao, L.Y. Sun, C.L. Fu, J.M. Liu, C. Li, R. Hai, C.F. Sang, Z.H. Hu, Z. Sun, J.S. Hu, L. Wang, J.L. Chen, Y.F. Liang, G.N. Luo, H. Ding, In situ diagnosis of Li-wall conditioning and H/D co-deposition on the first wall of EAST using laser-induced breakdown spectroscopy, *Plasma Phys. Control. Fusion.* 60 (2018) 085019, <https://doi.org/10.1088/1361-6587/aace83>.
- F. Colao, S. Almaviva, L. Caneve, G. Maddaluno, T. Fornal, P. Gasior, M. Kubkowska, M. Rosinski, LIBS experiments for quantitative detection of retained fuel, *Nucl. Mater. Energy.* 12 (2017) 133–138, <https://doi.org/10.1016/j.nme.2017.05.010>.
- C. Li, C.-L. Feng, H.Y. Oderji, G.-N. Luo, H.-B. Ding, Review of LIBS application in nuclear fusion technology, *Front. Phys.* 11 (2016) 114214, <https://doi.org/10.1007/s11467-016-0606-1>.
- O.A. Waseem, H.J. Ryu, Tungsten-based composites for nuclear fusion applications, in: *Nucl. Mater. Perform. InTech*, 2016, <https://doi.org/10.5772/62434>.
- N. Farid, H. Wang, C. Li, X. Wu, H.Y. Oderji, H. Ding, G.-N. Luo, Effect of background gases at reduced pressures on the laser treated surface morphology, spectral emission and characteristics parameters of laser produced Mo plasmas, *J. Nucl. Mater.* 438 (2013) 183–189, <https://doi.org/10.1016/j.jnucmat.2013.03.022>.
- G.S. Maturya, A. Marín-Roldán, P. Veis, A.K. Pathak, P. Sen, A review of the LIBS analysis for the plasma-facing components diagnostics, *J. Nucl. Mater.* 541 (2020) 152417, <https://doi.org/10.1016/j.jnucmat.2020.152417>.
- P. Paris, J. Butikova, M. Laan, A. Hakola, I. Jögi, J. Likonen, E. Grigore, C. Ruset, Comparison of LIBS results on ITER-relevant samples obtained by nanosecond and picosecond lasers, *Nucl. Mater. Energy.* 18 (2019) 1–5, <https://doi.org/10.1016/j.nme.2018.11.018>.
- D. Wu, L. Sun, J. Liu, Y. Lyu, H. Wu, S. Yuan, R. Hai, C. Li, C. Feng, D. Zhao, H. Ding, Parameter optimization of the spectral emission of laser-induced tungsten plasma for tokamak wall diagnosis at different pressures, *J. Anal. At. Spectrom.* 36 (2021) 1159–1169, <https://doi.org/10.1039/D1JA00009H>.
- M.S. Seyam, P. Koshy, M.A. Elbestawi, Laser powder bed fusion of unalloyed tungsten: a review of process, structure, and properties relationships, *Metals (Basel)*. 12 (2022) 274, <https://doi.org/10.3390/met12020274>.
- H. Wu, C. Li, D. Wu, J. Liu, Z. He, Q. Li, S. Yuan, X. Cui, R. Hai, H. Ding, Characterization of laser-induced breakdown spectroscopy on tungsten at variable ablation angles using a coaxial system in a vacuum, *J. Anal. At. Spectrom.* 36 (2021) 2074–2084, <https://doi.org/10.1039/D1JA00196E>.
- S.N. Andreev, S.V. Orlov, A.A. Samokhin, Simulation of pulsed-laser-induced explosive boiling, *Phys. Wave Phenom.* 15 (2007) 67–80, <https://doi.org/10.3103/S1541308X0702001X>.
- K. Yahiaoui, T. Kerdja, S. Malek, Phase explosion in tungsten target under interaction with Nd:YAG laser tripled in frequency, *Surf. Interface Anal.* 42 (2010) 1299–1302, <https://doi.org/10.1002/sia.3300>.

- [32] H.Y. Oderji, N. Farid, L. Sun, C. Fu, H. Ding, Evaluation of explosive sublimation as the mechanism of nanosecond laser ablation of tungsten under vacuum conditions, *Spectrochim. Acta Part B At. Spectrosc.* 122 (2016) 1–8, <https://doi.org/10.1016/j.sab.2016.05.008>.
- [33] J. Hermann, C. Gerhard, E. Axente, C. Dutouquet, Comparative investigation of laser ablation plumes in air and argon by analysis of spectral line shapes: insights on calibration-free laser-induced breakdown spectroscopy, *Spectrochim. Acta Part B At. Spectrosc.* 100 (2014) 189–196, <https://doi.org/10.1016/j.sab.2014.08.014>.
- [34] J. Hermann, D. Grojo, E. Axente, C. Gerhard, M. Burger, V. Craciun, Ideal radiation source for plasma spectroscopy generated by laser ablation, *Phys. Rev. E* 96 (2017) 053210, <https://doi.org/10.1103/PhysRevE.96.053210>.
- [35] A. Kramida, Y. Ralchenko, J. Reader, NIST ASD Team, NIST Atomic Spectra Database (ver. 5.10), [Online], Available: <https://physics.nist.gov/asd>, 2022 [2023, May 30]. National Institute of Standards and Technology, Gaithersburg, MD., (n.d.). doi:doi:10.18434/T4W30F.
- [36] N. Konjević, M. Ivković, N. Sakan, Hydrogen Balmer lines for low electron number density plasma diagnostics, *Spectrochim. Acta - Part B At. Spectrosc.* 76 (2012) 16–26, <https://doi.org/10.1016/j.sab.2012.06.026>.
- [37] M.A. Gigosos, M.Á. González, V. Cardenoso, Computer simulated Balmer-alpha, -beta and -gamma stark line profiles for non-equilibrium plasmas diagnostics, *Spectrochim. Acta Part B At. Spectrosc.* 58 (2003) 1489–1504, [https://doi.org/10.1016/S0584-8547\(03\)00097-1](https://doi.org/10.1016/S0584-8547(03)00097-1).
- [38] N. Konjević, M. Ivković, S. Jovičević, Spectroscopic diagnostics of laser-induced plasmas, *Spectrochim. Acta Part B At. Spectrosc.* 65 (2010) 593–602, <https://doi.org/10.1016/j.sab.2010.03.009>.
- [39] V. Dwivedi, D. Prochazka, D. Janičković, P. Šperka, P. Švec, J. Kaiser, P. Veis, P. Pořízka, LIBS protocol for the assessment of depth profile, homogeneity, and quantification of Fe/co - based bilayer ribbon, *Spectrochim. Acta Part B At. Spectrosc.* 196 (2022) 106509, <https://doi.org/10.1016/j.sab.2022.106509>.



Determination of austenitic steel alloys composition using laser-induced breakdown spectroscopy (LIBS) and machine learning algorithms

Ivan Traparic^a  and Milivoje Ivkovic^b

Institute of Physics Belgrade, Pregrevica 118, Belgrade 11080, Serbia

Received 5 November 2022 / Accepted 1 February 2023 / Published online 22 February 2023
© The Author(s), under exclusive licence to EDP Sciences, SIF and Springer-Verlag GmbH Germany, part of Springer Nature 2023, corrected publication 2023

Abstract. In this paper, the determination of composition of certified samples of austenitic steel alloys was done by combining laser-induced breakdown spectroscopy (LIBS) technique with machine learning algorithms. Isolation forest algorithm was applied to the MinMax scaled LIBS spectra in the spectral range from (200–500) nm to detect and eject possible outliers. Training dataset was then fitted with random forest regressor (RFR) and Gini importance criterion was used to identify the features that contribute the most to the final prediction. Optimal model parameters were found by using grid search cross-validation algorithm. This was followed by final RFR training. Results of RFR model were compared to the results obtained from linear regression with \mathcal{L}^2 norm and deep neural network (DNN) by means of R^2 metrics and root-mean-square error. DNN showed the best predictive power, whereas random forest had good prediction results in the case of Cr, Mn and Ni, but in the case of Mo, it showed limited performance.

1 Introduction

The structural materials of fusion reactors are subjected to thermal, mechanical, chemical, and radiation loads. Due to their excellent manufacturability, good mechanical properties, welding ability, and corrosion resistance, austenitic stainless steels were chosen as structural reference material for ITER [1]. In addition, entire vacuum vessel of LHD stellarator in Japan is made of austenitic steel [2], and to diagnose the composition of the deposits on the fusion reactor's first wall, test targets made of austenitic steel (AISI 316 L) were settled at ten positions on the first wall [3]. Laser-induced breakdown spectroscopy (LIBS) is one of the emerging analytical technique that is non-destructive, easy to use and requires little to no preparation of the sample [4]. Therefore, it represents a great tool for the analysis of the composition of austenitic steel samples. There are two main approaches to the LIBS analysis, namely standard calibration method and calibration-free method [5]. In the method where calibration curve

is constructed, a connection between one integrated line intensity and known concentrations is established, thus enabling the determination of unknown concentration. This method is by far the most used one. Alternatively, one can assume local thermodynamic equilibrium (LTE) in plasma and use Saha–Boltzmann equation to obtain plasma temperature and density, and from this the unknown concentrations regardless of the matrix effect. Machine learning algorithms have been successfully applied in analysis of Raman spectra, NIR and THz spectroscopy, vibrational spectroscopy, fusion plasma spectroscopy, etc., just to name a few [6–10]. In recent years, to speed up the analysis of LIBS spectra, machine learning methods are being used intensively [11–14]. These methods involve the usage of principal component analysis (PCA) for dimensionality reduction, support vector machine (SVM) for classification purposes and partial least squares regression (PLS) for multivariate regression problems [15]. Also, for classification or regression problems, many authors applied back propagation neural networks (BPNN) or convolutional neural networks (CNN) to the LIBS spectra in order to perform quantitative analysis of different samples [16–20]. Other regression algorithms, like random forest regression (RFR), have also been widely used [21–24]. Random Forest was constructed and reported by Breiman [25], and it is based on the ensemble of decision trees, where the decision or prediction is made

Physics of Ionized Gases and Spectroscopy of Isolated Complex Systems: Fundamentals and Applications. Guest editors: Bratislav Obradović, Jovan Cvetić, Dragana Ilić, Vladimir Srećković, Sylwia Ptasinska.

^a e-mail: traparic@ipb.ac.rs (corresponding author)

^b e-mail: ivke@ipb.ac.rs

by the majority prediction. This algorithm was previously applied on steel spectra by Zhang et al. [26] where they showed that this regression could be applied for the determination of composition of steel alloys. Later, Zhang with his collaborators used BPNN combined with SelectKBest algorithm for feature selection to trace minor elements in steel samples [27]. Liu and his coworkers also used random forest, combined with permutation importance feature selection to train and predict the composition of steel alloys [28]. Gini importance criteria was also used previously in combination with random forest on classification problems [29,30], but here we are applying it to regression problem.

In this paper, we will consider three algorithms, random forest, linear regression with \mathcal{L}^2 norm and deep neural network (DNN) to predict steel samples composition. Instead of making our own database, we will use the dataset published at the LIBS 2022 conference site [31] and record our own test dataset under similar conditions to check how much these small differences affect the final model performance. Idea to use RF algorithm is twofold. On the one end, it is able to catch non-linear phenomena in the data, on the other end to see to what extent we can use already implemented Gini importance criteria within RF to make good regression model. Although simple neural networks have yielded good analytical prediction in the past, in general, they are hard to train (better said, it is not easy to find most favorable architecture), so we wanted to see how close RF predictions are going to be with respect to DNN.

The paper is organized as follows: In the first section, a brief introduction and overview of previous results is given. In Sect. 2, the experimental setup and sample preparation is described. Section 3 gives the detail description of applied methodology and data preprocessing, while the results are given in Sect. 4. Finally, we gave the conclusion of this work in Sect. 5.

2 Experimental setup and sample preparation

Experimental setup is shown in Fig. 1.

The setup is a classical LIBS setup consisting of Quantel Q switched neodymium-doped yttrium aluminum garnet (Nd:YAG) laser having pulse width of 6 ns, repetition rate of 10 Hz, pulse energy of 96 mJ and operated at fundamental wavelength $\lambda = 1064$ nm. Laser beam was reflected from 45° angle mirror M and focused via lens L onto a target mounted on a x - y micrometric moving stage by a lens of focal length $f = 11$ cm. Light emitted from plasma was collected using a fiber optic cable with collimator having a focal length of $f_{fc} = 4.4$ cm and directed onto the $50 \mu\text{m}$ width entrance slit of Mechelle 5000 spectrograph that can record spectra from 200 to 950 nm. As a detector, we used Andor iStar ICCD camera (model DH734, 1024×1024 pixels) cooled to -15°C . Camera was triggered with a photodiode and gated by usage of Stan-

ford Research digital delay unit (model DG535). Delay from laser pulse was set to $0.6 \mu\text{s}$ and the gate width was set to $50 \mu\text{s}$.

Steel samples used in this work were AISI steels with certified composition from National Bureau of Standards (NBS, today NIST), whose elemental composition is given in Table 1.

Sample mentioned above, austenitic steel AISI 316L lies in between these tested models (concentrations of main elements: Cr 17%, Ni 12%, Mo 2% and Mn 2%). Each sample was firstly polished by sandpaper 200, followed by polishing it with sandpaper 600. In front of laser beam, external shutter was placed, coupled with laser pulse counter. Counter was set to 16 counts, as it is a binary counter, and after 16 pulses, the shutter is closed for another 16 pulses. This represents one acquisition of the spectra. For each sample, we recorded 22 spectra from different places on the target, and each spectra is a result of averaging 20 acquisitions on the same place (this gives 320 individual laser shots per place on the target). To further improve and increase signal, electrical gain of the camera was set to 80 (on the scale of 0–255).

3 Methodology and data preprocessing

Database used in this paper was downloaded from LIBS 2022 website [31]. This database consists of a spectra of 42 different steel samples, and for each sample, a 50 single-shot spectra were taken. This gives in total a database of 2100 spectra samples divided into 40,002

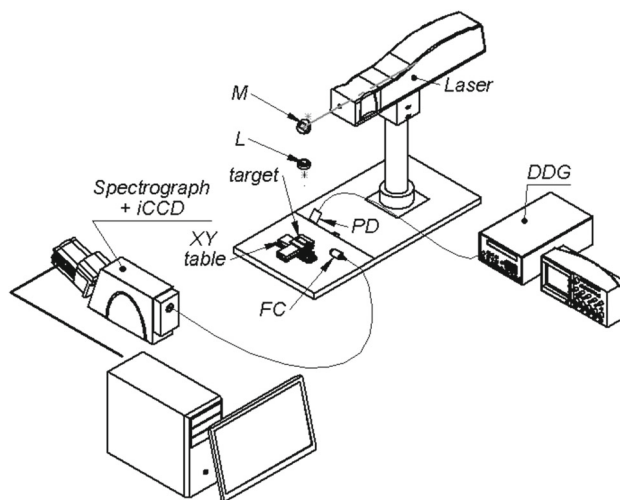
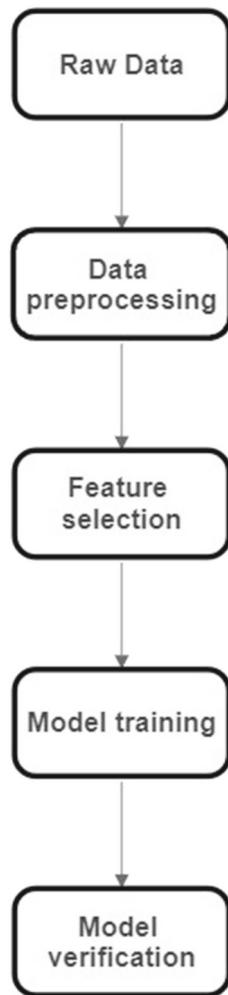


Fig. 1 Experimental setup. Laser (Quantel, $\lambda = 1064$ nm, pulse width 6 ns, peak energy 96 mJ) was focused via lens L onto the movable target and plasma spectrum was recorded by Andor iStar iCCD camera mounted on Echelle spectrograph. Camera gating was done by Stanford Research Digital Delay Generator (DDG, model 535) and triggered by photodiode (PD). Mirror M and lens L are integrated within a laser head, which was not drawn on this figure

Table 1 Steel alloy certified composition

Steel number	Steel type	Cr	Mn	Mo	Ni
443	Cr18.5–Ni9.5	18.5	3.38	0.12	9.4
445	AISI 410	13.31	0.77	0.92	0.28
446	AISI 321	18.35	0.53	0.43	9.11
447	AISI 309	23.72	0.23	0.053	13.26

**Fig. 2** Flowchart of procedures taken in this work

columns (each column corresponds to one wavelength). The flow diagram of our methodology is given in Fig. 2. For machine learning part of this work, we used python public repository scikit-learn.

3.1 Data preprocessing

Firstly, we restricted our dataset to the spectral range between 200 and 500 nm, as this is the spectral area where the most emission lines of metals of interest can be found. It is worth mentioning that all training dataset spectra were not intensity corrected. Therefore, no intensity correction was done on the test dataset.

In the spectra normalization step, two normalizations were tried to later adopt the best one, and those were total spectral area normalization, and standard normal variate (SNV) normalization. First one is clear, whereas SNV normalization represents a spectral normalization tool that mean centers the spectra and then divide each mean-centered intensity with its standard deviation [32]:

$$I_{\text{new}} = \frac{I_{\text{old}} - I_{\text{mean}}}{\sigma} \quad (1)$$

where I_{new} is the new intensity, I_{old} is the intensity that is being mean centered, I_{mean} is the mean intensity and σ is standard deviation of intensities. Besides these two, MinMax data scaling was also tried. MinMax scaling represents procedure where for each feature, we scale the values according to the formula below, so we have feature values between zero and one:

$$I_{\text{scaled}} = \frac{I - I_{\text{min}}}{I_{\text{max}} - I_{\text{min}}} \quad (2)$$

Proceeding further, we detected and ejected outliers with the help of Isolation Forest algorithm implemented in sci-kit learn. After the outliers have been removed, we fitted Random Forest regressor with aim to find features that give the most contribution to the final result. To achieve this, we actually trained four random forest models, one for each element, to have features that contribute to the each element prediction separately. Feature importances were calculated within random forest algorithm by usage of Gini importance. The higher the value, the more valuable this feature is to the final prediction.

3.2 Hyperparameters tuning and model selection

To find the optimal parameters of the model, we performed GridSearch cross-validation. This validation technique takes the given model parameters and initializes the model of interest with these parameters, splits provided dataset into training and test datasets, fits the model and reports the accuracy of the model through R^2 coefficient. This procedure is done five times in a row for each set of model parameters, where, at the end, for each model algorithm reports the best performance and with which parameters they were obtained. Used metrics to assess the predictive performance of the models were coefficient of determination R^2 and root-mean-square error (RMSE). With optimal parameters

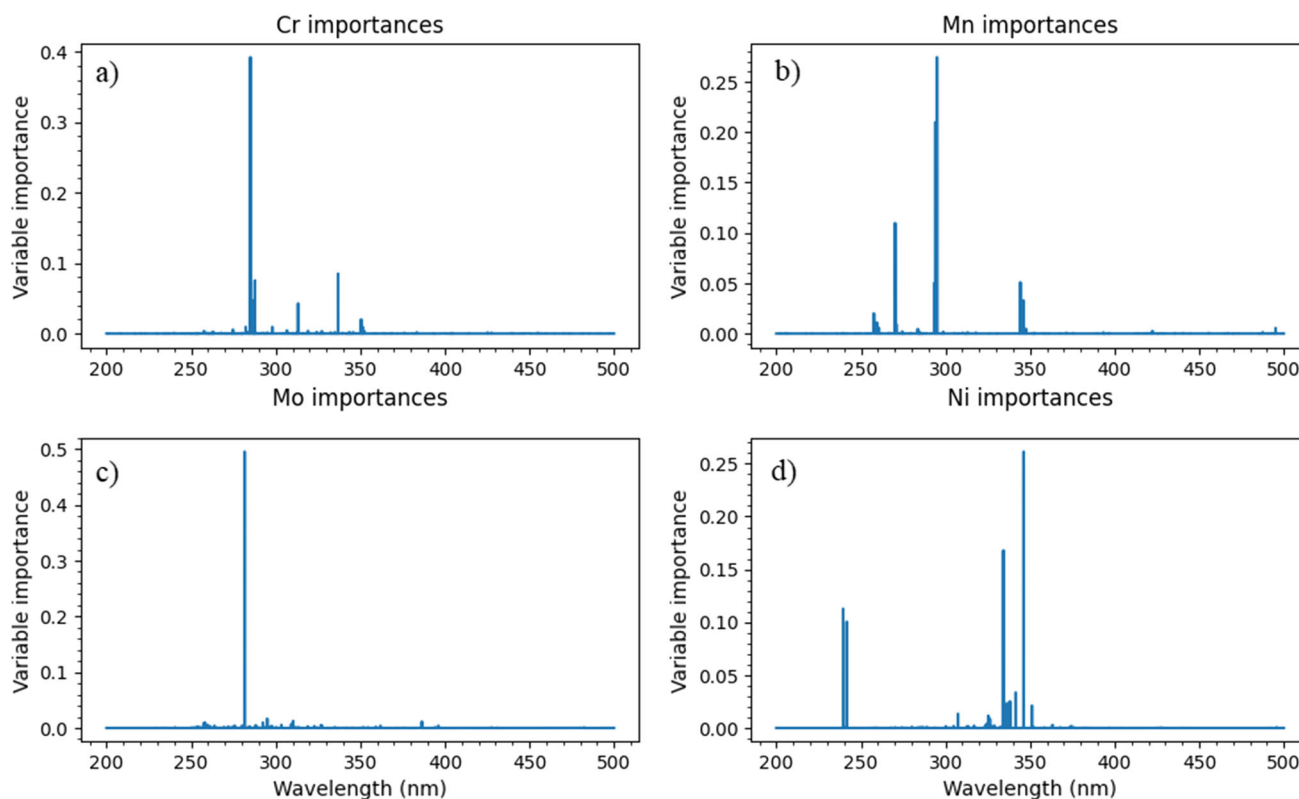


Fig. 3 Results for feature importance analysis for Cr and Mn (a, b) and Mo and Ni (c, d)

found, we proceeded to final model training and finally the prediction of steel samples composition.

4 Results

The results of feature importance analysis is given in Fig. 3. It is evident that the algorithm successfully recognized and selected persistent line of Mo II at 281.61 nm (see Fig. 3c). Also in Fig. 3d), lines of Ni II at 239.45 nm and 241.6 nm were successfully identified. Great importance was also given for Cr II lines around 285, 286, 287, 313 nm, as well as to Cr II line at 336 nm (see Fig. 3a)). Unimportant features have value of zero or close to zero, so the condition threshold was set to 10^{-4} , 2×10^{-4} and 5×10^{-4} , while the best results were obtained for threshold 2×10^{-4} . Hence, the final dimensionality of dataset used to train the final model is given in Table 2.

In GridSearch cross-validation, parameters for random forest that were supplied to the algorithm were number of estimators (number of trees in forest) which was changed from 200 to 350 in the step of 50, and maximal depth of the individual tree which was varied from none to 4. None here means that the tree is going to expand until all leaves are pure. In the case of linear regression, the only parameter that could be changed is \mathcal{L}^2 norm penalization coefficient α , and we have chosen the values of 0.5, 0.8 and 1. For DNN, considered

architectures were ones with one, two and three hidden layers [(100), (100, 100) and (100, 150, 50)]. Numbers in parentheses represent number of neurons in each hidden layer. Activation function was ReLU (Rectified Linear Unit). Best results reported for all models were ones with MinMax scaling. For RF, best results were the ones where number of trees was equal to 350 and maximum depth that was set to none. Best results with linear regression were reached for the α parameter equal to 0.8. Finally, for DNN, architecture with three hidden layers showed best performance. After dimensionality reduction via Gini importance, resulting dataset was divided into training and test datasets, keeping 20% of the data for testing. Validation of the models was done by using R^2 metrics and RMSE, and it is given in Table 3.

With model training finished, judging by the R^2 score, best overall performance is showed by deep neural network. The prediction precision for each element goes above 0.9, whereas the predicted values in the case of RF are little less. Results for linear regression are not given, since they are significantly worse than these, thus they were omitted. Prediction on recorded test dataset was done with RF as well as with DNN, and the predicted results are summed in Fig. 4. From Fig. 4a–d, it can be seen that DNN showed good performance on all elements, while the predictions made using RF are quite good for the case of Cr, Mn and Ni, but it showed bad overall performance regarding the prediction of Mo, see Fig. 4d. There was no difference when we tried to

Table 2 Dimensionality and number of samples in training dataset used for model training

Element	Number features	Number of samples
Cr	273	1608
Mn	129	1608
Mo	317	1608
Ni	120	1608

All useful information is contained in these selected features

predict Mo concentration with all features, where unimportant features were not removed.

5 Conclusion and future development

In this paper, the prediction of austenitic steel alloy samples was done using the random forest algorithm and deep neural network. Data preprocessing consisted of applying MinMax scaler on the raw data, followed by outliers removal with isolation forest algorithm. Feature

selection was performed by Gini importance criterion within random forest algorithm. It successfully isolated most important features, thus enabling the dimensionality reduction while keeping all the necessary information. This was preceded by final training of three models: random forest, linear regression with \mathcal{L}^2 norm and deep neural network. Random forest and neural network showed better predictive power than linear regression; hence, they were used as selected models for prediction of the steel alloy composition. Trained random forest model showed good predictive power for

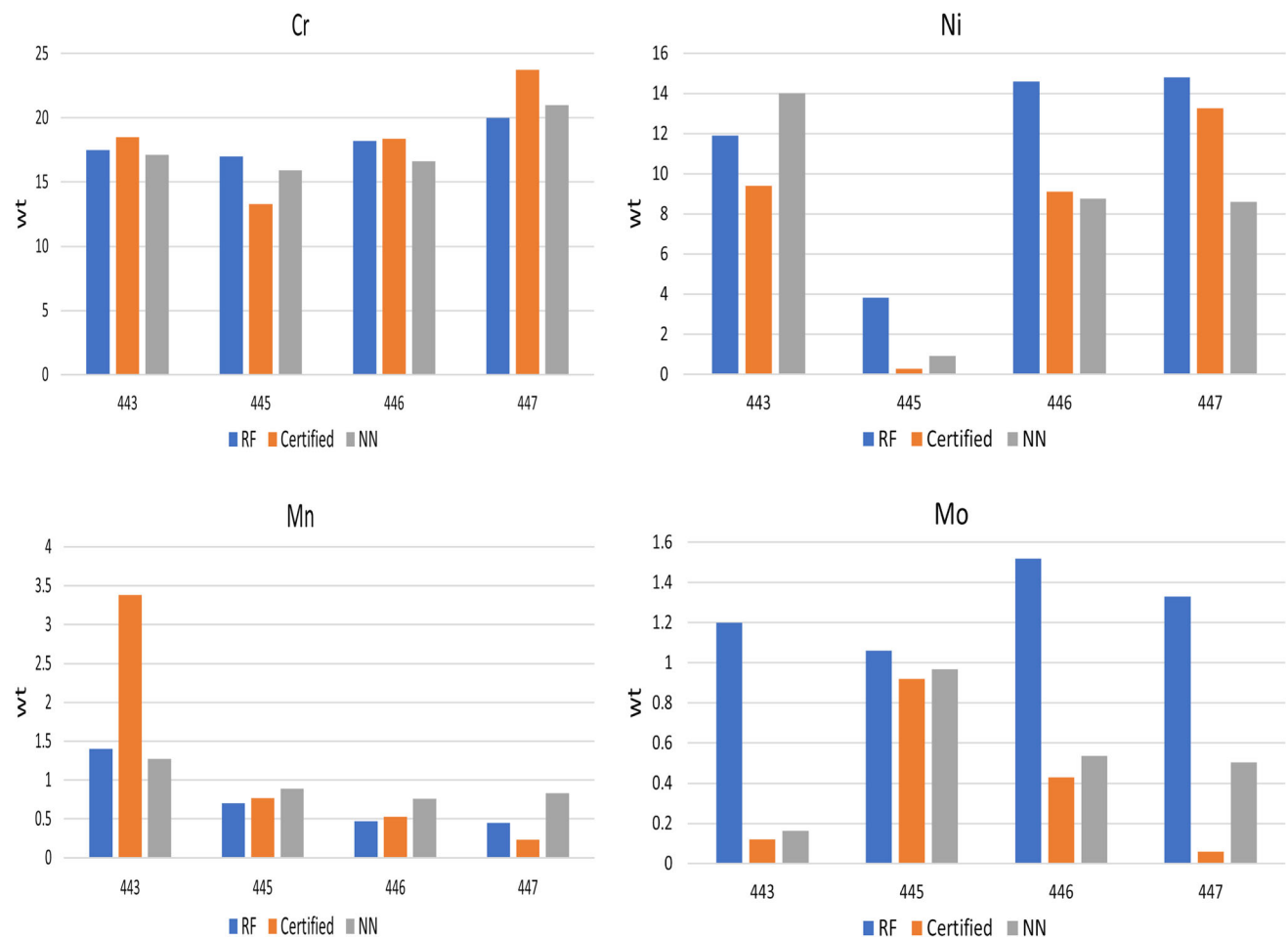


Fig. 4 RFR and DNN predicted results (denoted with RF and NN on the figure) and comparison with certified values. Numbers on x-axis denote the steel sample number given in Table 1. The figure indicates that the models learned and yielded good results in the case of Cr (a), Mn (c) and Ni (b), but on the other hand, RFR had rather poor performance in the case of Mo (d)

Table 3 R^2 and RMSE values for validation dataset

Element	$R^2_{\text{RF}}R$	R^2_{DNN}	RMSE _{RF}	RMSE _{NN}
Cr	0.88	0.97	3.68	1.84
Mn	0.89	0.93	0.397	0.313
Mo	0.85	0.96	0.511	0.263
Ni	0.97	0.98	1.77	1.21

Cr, Ni and Mn, but rather poor performance in the case of Mo. On the other hand, neural network showed good overall predictive power. Nevertheless, random forest algorithm, combined with the data preprocessing techniques, shows a good potential for application in austenitic steel alloy composition prediction, which was also confirmed by results from other authors. For future work, we tend to write a better feature extraction software that should improve the feature selection and hence the predictive power of a used regressor. Also, good overall results are obtained, although the training and test datasets were not intensity corrected. This work shows how useful it can be, to build a unique steel dataset for later usage by different authors, as they not need to every time record their own datasets. These results can be further improved, if one performs calibration transfer, as these spectra were recorded on different instruments. Here, this was not performed as we have not had any identical standard that was used on primary instrument.

Acknowledgements The research was funded by the Ministry of Science, Technological Development and Innovations of the Republic of Serbia, Contract Numbers: 451-03-68/2022-14/200024 and 451-03-68/2022-14/200146, and supported by the Science Fund of the Republic Serbia, Grant No. 3108/2021—NOVA2LIBS4fusion. Also we want to acknowledge the work of our technical associate Stanko Milanović for valuable assistance during the experimental setup. Finally, we want also to thank prof. Jelena Savović for providing us the test samples used in this work.

Author contributions

IT involved in methodology, software and original draft writing; MI involved in conceptualization, supervision and original draft editing.

Data Availability Statement This manuscript has associated data in a data repository. [Authors' comment: As we recorded the spectra of only four steel standard samples, we are of the opinion that scientific community will not have much use of this data, hence it is decided not to deposit it.]

Declarations

Conflict of interest Hereby, we want to state that these results should not be in any case compared to ones obtained by various authors at the LIBS 2022 conference benchmark-

ing competition, where this training dataset was first used. Best results from that competition will be published separately in special issue of Spectrochimica Acta B, and results from this paper have nothing to do with that competition. This paper was an extension of the work presented at SPIG 2022 conference.

References

1. R.J. Konings, R.E. Stoller (eds.), *Comprehensive Nuclear Materials*. (Elsevier, Amsterdam, 2020)
2. N. Inoue, A. Komori, H. Hayashi, H. Yonezu, M. Iima, R. Sakamoto, Y. Kubota, A. Sagara, K. Akaishi, N. Noda, N. Ohyabu, O. Motojima, Design and construction of the LHD plasma vacuum vessel. *Fus. Eng. Des.* **41**(1), 331–336 (1998). [https://doi.org/10.1016/S0920-3796\(98\)00248-8](https://doi.org/10.1016/S0920-3796(98)00248-8)
3. V. Alimov, M. Yajima, S. Masuzaki, M. Tokitani, Analysis of mixed-material layers deposited on the toroidal array probes during the FY 2012 LHD plasma campaign. *Fus. Eng. Des.* **147**, 111228 (2019). <https://doi.org/10.1016/j.fusengdes.2019.06.001>
4. D.C.L.J. Radziemski, *Spectrochemical analysis using laser plasma excitation*, edited by D.C.L.J. Radziemski (Marcel Dekker Inc, New York, 1989)
5. E. Tognoni, G. Cristoforetti, S. Legnaioli, V. Palleschi, Calibration-free laser-induced breakdown spectroscopy: state of the art. *Spectrochim. Acta Part B At. Spectrosc.* **65**(1), 1–14 (2010). <https://doi.org/10.1016/j.sab.2009.11.006>
6. C.A.M. Ramirez, M. Greenop, L. Ashton, I. ur Rehman, Applications of machine learning in spectroscopy. *Appl. Spectrosc. Rev.* **56**(810), 733–763 (2021). <https://doi.org/10.1080/05704928.2020.1859525>
7. N.M. Ralbovsky, I.K. Lednev, Towards development of a novel universal medical diagnostic method: Raman spectroscopy and machine learning. *Chem. Soc. Rev.* **49**, 7428–7453 (2020). <https://doi.org/10.1039/D0CS01019G>
8. W. Fu, W.S. Hopkins, Applying machine learning to vibrational spectroscopy. *J. Phys. Chem. A* **122**, 167–171 (2017). <https://doi.org/10.1021/acs.jpca.7b10303>
9. H. Park, J.-H. Son, Machine learning techniques for THz imaging and time-domain spectroscopy. *Sensors* (2021). <https://doi.org/10.3390/s21041186>
10. M. Koubiti, M. Kerebel, Application of deep learning to spectroscopic features of the Balmer-Alpha line for hydrogen isotopic ratio determination in tokamaks. *Appl. Sci.* (2022). <https://doi.org/10.3390/app12199891>
11. T. Chen, T. Zhang, H. Li, Applications of laser-induced breakdown spectroscopy (LIBS) combined with machine

- learning in geochemical and environmental resources exploration. *Trends Anal. Chem.* **133**, 116113 (2020). <https://doi.org/10.1016/j.trac.2020.116113>
12. C. Sun, Y. Tilan, L. Gao et al., Machine learning allows calibration models to predict trace element concentration in soils with generalized LIBS spectra. *Sci. Rep.* **9**, 11363 (2019). <https://doi.org/10.1038/s41598-019-47751-y>
 13. X. Zhang, F. Zhang, H.-T. Kung, P. Shi, A. Yushanjiang, S. Zhu, Estimation of the Fe and Cu contents of the surface water in the Ebinur lake basin based on LIBS and a machine learning algorithm. *Int. J. Environ. Res. Public Health* (2018). <https://doi.org/10.3390/ijerph15112390>
 14. L. Sheng, T. Zhang, G. Niu, K. Wang, H. Tang, Y. Duan, H. Li, Classification of iron ores by laser-induced breakdown spectroscopy (LIBS) combined with random forest (RF). *J. Anal. At. Spectrom.* **30**, 453–458 (2015). <https://doi.org/10.1039/C4JA00352G>
 15. Y. Tian, Q. Chen, Y. Lin, Y. Lu, Y. Li, H. Lin, Quantitative determination of phosphorus in seafood using laser-induced breakdown spectroscopy combined with machine learning. *Spectrochim. Acta Part B At. Spectrosc.* **175**, 106027 (2021). <https://doi.org/10.1016/j.sab.2020.106027>
 16. M.S. Babu, T. Imai, R. Sarathi, Classification of aged epoxy micro-nanocomposites through PCA- and ANN-adopted LIBS analysis. *IEEE Trans. Plasma Sci.* **49**(3), 1088–1096 (2021). <https://doi.org/10.1109/TPS.2021.3061410>
 17. X. Cui, Q. Wang, Y. Zhao et al., Laser-induced breakdown spectroscopy (LIBS) for classification of wood species integrated with artificial neural network (ANN). *Appl. Phys. B* **125**, 12556 (2019). <https://doi.org/10.1007/s00340-019-7166-3>
 18. R. Junjuri, M.K. Gundawar, A low-cost LIBS detection system combined with chemometrics for rapid identification of plastic waste. *Waste Manag.* **117**, 48–57 (2020). <https://doi.org/10.1016/j.wasman.2020.07.046>
 19. L.-N. Li, X.-F. Liu, F. Yang, W.-M. Xu, J.-Y. Wang, R. Shu, A review of artificial neural network based chemometrics applied in laser-induced breakdown spectroscopy analysis. *Spectrochim. Acta Part B At. Spectrosc.* **180**, 106183 (2021). <https://doi.org/10.1016/j.sab.2021.106183>
 20. F. Poggialini, B. Campanella, S. Legnaioli, S. Pagnotta, S. Raneri, V. Palleschi, Improvement of the performances of a commercial hand-held laser-induced breakdown spectroscopy instrument for steel analysis using multiple artificial neural networks. *Rev. Sci. Instrum.* **91**(7), 073111 (2020). <https://doi.org/10.1063/5.0012669>
 21. H. Tang, T. Zhang, X. Yang, H. Li, Classification of different types of slag samples by laser-induced breakdown spectroscopy (LIBS) coupled with random forest based on variable importance (VIRF). *J. Anal. At. Spectrom.* **32**, 2194–2199 (2017). <https://doi.org/10.1039/C7JA00231A>
 22. F. Ruan, J. Qi, C. Yan, H. Tang, T. Zhang, H. Li, Quantitative detection of harmful elements in alloy steel by LIBS technique and sequential backward selection-random forest (SBS-RF). *Anal. Methods* **7**, 9171–9176 (2015). <https://doi.org/10.1039/C5AY02208H>
 23. J. Liang, M. Li, Y. Du, C. Yan, Y. Zhang, T. Zhang, X. Zheng, H. Li, Data fusion of laser induced breakdown spectroscopy (LIBS) and infrared spectroscopy (IR) coupled with random forest (RF) for the classification and discrimination of compound *Salvia miltiorrhiza*. *Chemom. Intell. Lab. Syst.* **207**, 104179 (2020). <https://doi.org/10.1016/j.chemolab.2020.104179>
 24. G. Yang et al., The basicity analysis of sintered ore using laser-induced breakdown spectroscopy (LIBS) combined with random forest regression (RFR). *Anal. Methods* **9**, 5365–5370 (2017). <https://doi.org/10.1039/C7AY01389B>
 25. L. Breiman, Random forests. *Mach. Learn.* **45**, 5–32 (2001). <https://doi.org/10.1023/A:1010933404324>
 26. T. Zhang et al., A novel approach for the quantitative analysis of multiple elements in steel based on laser-induced breakdown spectroscopy (LIBS) and random forest regression (RFR). *J. Anal. At. Spectrom.* **29**, 2323 (2014). <https://doi.org/10.1039/c4ja00217b>
 27. Y. Zhang, C. Sun, L. Gao, Z. Yue, S. Shabbir, W. Xu, M. Wu, J. Yu, Determination of minor metal elements in steel using laser-induced breakdown spectroscopy combined with machine learning algorithms. *Spectrochim. Acta Part B At. Spectrosc.* **166**, 105802 (2020). <https://doi.org/10.1016/j.sab.2020.105802>
 28. K. Liu et al., Quantitative analysis of toxic elements in polypropylene (PP) via laser-induced breakdown spectroscopy (LIBS) coupled with random forest regression based on variable importance (VI-RFR). *Anal. Methods* **11**, 4769 (2019). <https://doi.org/10.1039/c9ay01796h>
 29. K. Wei, Q. Wang, G. Teng, X. Xu, Z. Zhao, G. Chen, Application of laser-induced breakdown spectroscopy combined with chemometrics for identification of penicillin manufacturers. *Appl. Sci.* (2022). <https://doi.org/10.3390/app12104981>
 30. X. Jin, G. Yang, X. Sun, D. Qu, S. Li, G. Chen, C. Li, D. Tian, L. Yao, Discrimination of rocks by laser-induced breakdown spectroscopy combined with random forest (RF). *J. Anal. At. Spectrom.* **38**, 243–252 (2023). <https://doi.org/10.1039/D2JA00290F>
 31. E. Kepes. (2022) LIBS 2022 quantification contest. https://figshare.com/projects/LIBS2022_Quantification_Contest/142250
 32. T.W. Randolph, Scale-based normalization of spectral data. *Cancer Biomark.* **2**, 135–144 (2006). <https://doi.org/10.3233/CBM-2006-23-405>

Springer Nature or its licensor (e.g. a society or other partner) holds exclusive rights to this article under a publishing agreement with the author(s) or other rightsholder(s); author self-archiving of the accepted manuscript version of this article is solely governed by the terms of such publishing agreement and applicable law.



Stark spectral line broadening modeling by machine learning algorithms

Irinel Tapalaga¹ · Ivan Traparić^{1,2} · Nora Trklja Boca¹  · Jagoš Purić¹ · Ivan P. Dojčinović¹

Received: 9 February 2021 / Accepted: 11 November 2021 / Published online: 16 January 2022
© The Author(s), under exclusive licence to Springer-Verlag London Ltd., part of Springer Nature 2021

Abstract

Various types of electric fields contained in the laboratory and astrophysical plasma cause a Stark broadening of spectral lines in plasma. Therefore, a large number of spectroscopic diagnostics of laboratory and astrophysical plasma are based on experimental and theoretical studies of Stark broadening of spectral lines in plasma. The topic of the present investigation is the Stark broadening caused by free electrons in plasma and its dependence on certain atomic parameters using a new method based on the machine learning (ML) approach. Analysis of empirical data on atomic parameters was done by ML algorithms with more success than it was previously done by classical methods of data analysis. The correlation parameter obtained by artificial intelligence (AI) is slightly better than the one obtained by classical methods, but the scope of application is much wider. AI conclusions are applicable to any physical system while conclusions made by classical analysis are applicable only to a small portion of these systems. ML algorithms successfully identified quantum nature by analyzing atomic parameters. The biggest issue of classical analysis, which is infinite spectral line broadening for high ionization stages, was resolved by AI with a saturation tendency.

Keywords Machine learning · Stark broadening · Atomic data · Plasma physics

1 Introduction

One of the greatest challenges of the modern science is the processing of enormous amounts of data. Two primary goals in this field are how to learn from data and how to make data predictions [37]. Data science and machine learning (ML) have made tremendous progress in the last few decades. Statistical physics have a great contribution to the development and understanding methods in ML [6]. ML algorithms have become very important in the analysis of data in physics and related sciences. ML methods have been shown to be useful in different physical sciences: astrophysics, particle physics, chemical physics, condensed-matter physics, quantum physics. In astrophysics and particle physics experiments such as CMS and ATLAS

at the LHC in CERN, as well as projects such as the Sloan Digital Sky Survey (SDSS), gives enormous amount of data measuring the particle collisions and properties of a billion stars and galaxies [37]. Object classification in astrophysics is very important task [3, 27, 46] whose successful solution enables easier selection of objects according to certain criteria and their further study. Use of ML algorithms enables the solution of numerous problems in the processing of astronomical data and enables the consideration of dependences and correlations that have not been observed before [25, 26, 44, 45]. In one of the most significant modern experiment: observation of the gravitational waves arises from the merger of a binary black hole, ML algorithms are used to clear the noise in the signals of gravitational waves [1, 57]. Large development in the domain of data science, as well as the strengthening of connection to quantum physics, enabled the development of our knowledge of the matter. Namely, atomic physics is a base for the creation of new molecules and advanced materials, as well. The theoretical basis of atomic physics is quantum mechanics. Quantum mechanics has provided a base for successful research of molecular

✉ Nora Trklja Boca
nora@ff.bg.ac.rs

¹ Faculty of Physics, University of Belgrade, Studentski trg 12, Belgrade 11000, Serbia

² Institute of Physics, University of Belgrade, Pregrevica 118, Belgrade 11080, Serbia

physics and condensed matter physics, as well as nuclear physics and particle physics. Consequently, the development of ML algorithms recently has been used to address fundamental questions in the domain of quantum physics [4, 49]. One of the big problems in quantum physics is the inability to solve the Schrödinger equation for multiparticle systems, i.e., inability to obtain appropriate wave functions. In quantum chemistry and chemical physics, ML algorithms are used for analysis and prediction of physical and chemical properties, chemical structures, optimization of reaction parameters and process conditions (a type of reagents, catalysts, concentration, time, temperature), prediction of new reaction design, maximization of the production rate of chemical reactions [2, 9, 18, 29, 59, 60]. In condensed-matter physics and material science, ML has been used to improve the calculation of material properties, as well as a modeling of properties of new materials [10, 12, 19, 43, 58]. Learning techniques can be used for the research of advanced materials: materials for memory devices, solar cells, batteries, sensors, nanoparticle catalysts, supercapacitors, superhard material, etc.

From interconnections between quantum physics and ML, scientific community has huge expectation [4, 8, 23, 24, 32, 33, 35, 38, 49, 54]. There are many current questions about entanglement classification [23], quantum state tomography [54], solving the quantum many-body problem [8, 24]. There are many interesting active ML models with the aim of creation of new quantum experiments [32, 33, 38], as well as quantum machine models [17]. Also, ML can be used to discover physical concepts from new experimental data [28]. ML approaches have been applied to atomic physics. The neural networks can be used as a representation of quantum states [6]. There is a lack of atomic parameters for heavy elements and high ionized atoms. ML can be applied to the classification of heavy atoms energy levels according to their electronic configurations [7, 41]. Learning techniques have been applied for the investigation of atomic processes, like ionization and radiation [6]. Analysis of spectra from stars and quasars, as well as laser-produced and fusion plasma, can be done with the help of ML [40, 45]. The knowledge of atomic parameters is a base for atomic processes modeling. The aim of this research work is to use machine learning algorithms for modeling Stark spectral line broadening.

Stark broadening of spectral lines is a tool for spectroscopic diagnostics of laboratory plasma, as well as astrophysical and fusion plasma. In astrophysics, Stark line widths are used for analysis of stellar spectra, investigation of chemical abundances of elements in different stellar objects, opacity calculations. Recently, it has been shown that Stark broadening has a big influence on the uncertainties in the calculation of the solar opacity [34]. Spectral

analysis has a very important role in the physics of fusion plasma, too. Part of the current research in this field is concentrated on the possibility of using various durable materials, (as Mo, Ti, Zr...) for tungsten alloying. During the operation of fusion machines, it is expected that a small amount of these materials would be found in the peripheral regions of confined plasma, because of the spattering process. Stark widths of these atoms and their ions are needed for a detailed spectral analysis and diagnostics.

Stark broadening of spectral lines of neutral atoms and ions is used in science for a number of problems in various physical conditions. Theoretical calculations of the Stark width values usually use one of the models given by Griem et al. [20]; Sahal-Bréchet et al. [47]; Griem [21]; Dimitrijević and Konjević [13]. Recent research indicates the importance and usefulness of searching for possible types of regularities in the framework of a Stark broadening investigation [16, 53, 56]. Still, existing tables with calculated and measured Stark widths have a big lack of data. There is a need for Stark widths data in the wide range of chemical elements, plasma temperature and electron densities. In this paper a correlation between Stark broadening and environment parameters, such as the ionization potential of the upper level of the corresponding transition, electron density and temperature, will be investigated using modern ML algorithms. If this method proves to be accurate enough, the process of calculating the value of Stark widths will be significantly accelerated and facilitated.

2 Theoretical background of Stark line broadening

One of the primary deexcitation ways of excited atoms is photon emission. A cumulative signal obtained from a radiating medium (for example plasma) is a spectral line with a small frequency range. Each spectral line emitted by atoms in plasma has a finite frequency range represented as line width. Generally, there are four types of spectral line broadening in plasma. One is a natural line broadening, related with the uncertainty in the energy of the states involved in the transition profile, with line width negligible compared to the other broadening mechanisms. The second is instrumental line broadening which includes the influence of spectral device on a line profile. Doppler broadening is caused by a distribution of velocities of atoms or molecules and depends on plasma temperature. The pressure broadening, which generally depends on pressure (i.e., density of active species) and temperature, results from the interactions of the emitters with neighboring neutral particles (resonant and Van der Waals broadening) and ionized particles (Stark broadening). Natural and instrumental broadening are always present. The existence of other types

of spectral line broadening depends on the plasma conditions. Stark broadening is caused by the free charges which surround the emitters in plasma and produce the local electric field which affects the emission process, giving rise to shifts of the emission wavelengths or changes in the phase of the radiation. This is observed as a phenomenon of broadening and shift of the spectral lines [22]. This effect is determined by the intensity of the local electric field and it depends on the density of charged particles in the plasma (electrons and ions). The influence of free electrons on the line broadening in plasma is much more pronounced than the influence of ions. The topic of the present investigation is the Stark broadening caused by free electrons in plasma using new method based on ML approach.

The general formula for Stark width calculation in the impact approximation, which is appropriate to use in the overwhelming number of cases, is [22]:

$$\omega = N_e \left\langle v \cdot \left(\sigma_{if} + \sum_{i'} \sigma_{ii'} + \sum_{f'} \sigma_{ff'} \right) \right\rangle_{av} \quad (1)$$

The line has a Lorentzian profile whose width is ω , expressed in angular frequencies unit [rad/s]. N_e and v are electron density and velocity, respectively. The average is being over the velocity distribution of perturbing electrons. The cross sections $\sigma_{ii'}$ ($\sigma_{ff'}$) are for inelastic scattering on the initial (final) state of the line,

while σ_{if} is an effective elastic cross section to be calculated essentially from the difference of elastic scattering amplitudes f_i and f_f .

The formula proposed by Griem [22] is very complicated, it cannot be resolved exactly, so it is useful to use different approaches in the calculation. The regularity approach which correlates Stark width of spectral line, ω , expressed in [rad/s], electron density N_e , electron temperature T_e and positive value of electron binding energy on the upper level of the transition, expressed in [eV], is given by Purić and Šćepanović [42] (Eq. 2):

$$\omega = Z_e^k \cdot a \cdot N_e \cdot f(T_e) \cdot \chi^{-b} \quad (2)$$

where $Z_e = 1, 2, 3, \dots$ for neutrals, singly charged ions, ... respectively and it represents the rest core charge of the ionized emitter and a , b and k are coefficients independent of electron concentration and ionization potential for a particular transition and the rest core charge of the emitter. In Eq. 2, stark width is expressed in radian per second and this is the only suitable unit to analyze the regularity of Stark broadening. If regularity analysis use wavelengths (λ) and line widths ($\Delta\lambda$) expressed in meters, Eq. 2 should be written as follows:

$$\Delta\lambda = \frac{Z_e^k \cdot a \cdot N_e \cdot f(T_e) \cdot \chi^{-b} \cdot \lambda^2}{2 \cdot \pi \cdot c} \quad (3)$$

In Eq. 3, every transition have its own wavelength, while the other parameters remain unchanged, so regularity can't be seen.

Atoms and ions with the same number of electrons form an isoelectronic sequence. It is expected that spectral series within an isoelectronic sequence show regularity behavior because a wide range of atomic/ionic parameters depend on the electron number. The results obtained by regularity studies have proven to be very precise and this approach has been used in previous papers of our group. In the last decade we have investigated Stark broadening regularities using Eq. 2 within spectral series of individual elements [14, 15, 30, 51, 52], within spectral series of individual isoelectronic sequences [53, 55, 56] and we published one paper with analysis of Stark line broadening regularities within two spectral series of isoelectronic sequences simultaneously: potassium and copper [16]. The present investigation goes one step further and analyses all elements for which there are available data needed for Stark broadening investigation, simultaneously, using machine learning approach. The aim is to find the best possible model which correlates Stark width of spectral line with all available parameters for transition of interest (atomic parameters and environmental parameters).

3 Dataset creation and data cleaning

In order to create our dataset we used two public repositories connected with atomic spectroscopy. First one is Stark B database [48], where the parameters of Stark broadening for different emitters are given. The features taken from this database are: chemical element, ionization stage, upper and lower level of spectral transitions, Stark broadening, the environment temperature and electron density in environment. In the available database, stark widths are expressed in angstroms (1 angstrom = 10^{-10} m). For analysis purpose, angstroms are converted in radian per second [53] (Eq. 4). In the physical sense, radian per second is unit related with energy.

$$\omega = \frac{2\pi \cdot c \cdot \Delta\lambda}{\lambda^2} \quad (4)$$

We also performed data analysis with Stark widths expressed in meters, using machine learning and results have not shown any meaningful trends. This is confirmation that radians per second are suitable unit for machine learning approach, too. When the difference between energy levels of the same multiplet is small compared to the distance to the next level linked by an allowed

transition, all the fine structure lines of the same multiplet have the same width and shift in Stark B database. In that case, the data are given of the multiplet only (w_{mult}) and for an average wavelength of the whole multiplet (λ_{mult}). The width value for a particular line (w_{line}) within a multiplet is obtained from:

$$w_{\text{line}} = \frac{w_{\text{mult}} \cdot \lambda_{\text{line}}^2}{\lambda_{\text{mult}}^2} \quad (5)$$

To ensure better results, we enriched features taken from Stark B database with ones taken from NIST Atomic Spectra database [31]: binding energy of both upper and lower transition levels, ground level energy, total angular momentum quantum number J of both upper and lower transition level, as well as principal n and orbital ℓ quantum numbers and total angular momentum J quantum numbers of upper and lower transition levels.

The algorithm of connecting those two databases to form our own works as described below. For every transition connected with certain chemical element, we take the electronic configuration of both upper and lower levels from Stark B database. Then, we look for that particular element in NIST database and compare the electronic configurations. If they match, then we take the binding energy of those levels,

their principal quantum number n , orbital quantum number ℓ and total angular momentum quantum number J and finally the ionization energy of that atom. The ionization energy is needed for calculation of the so-called upper level ionization potential χ . For practical purposes, we replaced the chemical element name with its atomic number Z and its charge, obtained from periodic system of elements (i.e., instead of Ar+2, we used $Z = 10$ and charge = + 2). For better understanding of the algorithm mentioned above, pseudo code is given in table Algorithm 1 while the complete code can be found at <https://github.com/ivantrparic/StarkBroadeningMLApproach>. After we completed the creation of database, it consisted of 54,236 successfully matched transitions for 53 different emitters.

Then we proceeded with data cleaning. Outliers were detected as those transitions where the energy of upper level is smaller than the energy of lower level, which is physically impossible, thus those lines were removed from the database. Next, we excluded transitions given for temperatures above 150,000 K and electron densities above 10^{18} cm^{-3} , because we are currently not interested in making predictions for those plasma conditions. As a result, this dataset contains 53 emitters and 34,973 spectral lines and follows a normal distribution.

Algorithm 1 Creation of database used in this paper

```

1: for element in elements do
2:   charge, Z ← DetermineZAndCharge(element)
3:   elementNIST ← FindElementInNIST(element)
4:   ElectronTemperature ← electronic temperature from Stark B database
5:   ElectronDensity ← electron density from Stark B database
6:   StarkWidth ← stark broadening from Stark B database
7:   UpperLevels ← upper transition levels from Stark B for element
8:   LowerLevels ← lower transition levels from Stark B for element
9:   Levels ← levels configuration in NIST database for elementNIST
10:  Upperbindingenergy, Lowerbindingenergy, jupper, jlower, ni, li, nf, lf, χ ← Arrays
    for saving found quantities from NIST database
11:  GroundLevel ← FindGroundLevel(elementNIST)
12:  for lowerlevel in LowerLevels do
13:    for level in Levels do
14:      if lowerlevel == level then
15:        Lowerbindingenergy, nf, lf, jlower ← binding energy
        and associated quantum numbers for that lower level taken from NIST
16:        upper level ionization potential χ ← GroundLevel - Lowerbindingenergy
17:        break
18:  for upperlevel in UpperLevels do
19:    for level in Levels do
20:      if upperlevel == level then
21:        Upperbindingenergy, ni, li, jupper ← binding energy
        and associated quantum numbers for that upper level taken form NIST
22:        break
23:  if length(Lowerbindingenergy) != length(Upperbindingenergy) then
24:    Error
25:    return
26:  else
27:    for i != length(Lowerbindingenergy) do
28:      Z, ElectronTemperature, ElectronDensity, charge, χ, GroundLevel,
        Upperbindingenergy, jupper, Lowerbindingenergy, jlower, ni, li, nf, lf, StarkWidth
        ← Insert line i in database

```

Table 1 List of ML algorithms and parameters

Model	Parameters
Linear regression	Normalize: [True, False]
Decision tree regressor	max_depth [3, 5, 10]
Random forest regressor	n_estimators [5, 10, 15, 100]
Gradient boosting regressor	max_depth [3, 5, 10], n_estimators [100, 150, 200]

Table 2 List of ML algorithms and their final score

Model	Best R^2	Parameters
Linear regression	0.38	Normalize: False
Decision tree regressor	0.92	max_depth = 10
Gradient boosting regressor	0.94	max_depth = 10, n_estimators = 150

It consisted of 15 columns, 14 of those were our features (atomic number Z , electron temperature, electron density, charge, lower level ionization potential χ , ground level energy, lower level energy, lower level J , upper level energy, upper level J , principal quantum number of lower level n_f , orbital quantum number of lower level ℓ_f , principal quantum number of upper level n_i , orbital quantum number of upper level ℓ_i), and 15th column was our target value ω .

4 Model creation and training

For model creation and training, we used public Python package Sci-kit learn. We created four models, every being Pipeline with two steps. In each object of Pipeline class, the

first step was data scaling using StandardScaler, and in second step we made our predictions with defined model. Considered models were: Linear Regression, Decision Tree Regressor, Random Forest Regressor and Gradient Boosting Regressor. We split the dataset into training and test dataset using train_test_split method, leaving 25% of the data for testing. To find the best model out of four considered, and best parameters for that model, we used ShuffleSplit combined with GridSearchCV. In ShuffleSplit object we set number of splits to 5, and we left 30% of data for testing. In GridSearchCV object we set cross validation to ShuffleSplit object. The values for parameters of models used in GridSearchCV are presented in table 1. Other parameters of the model remained at their default values.

To rank the performance of models, we used best Coefficient of Determination, R^2 , value obtained after

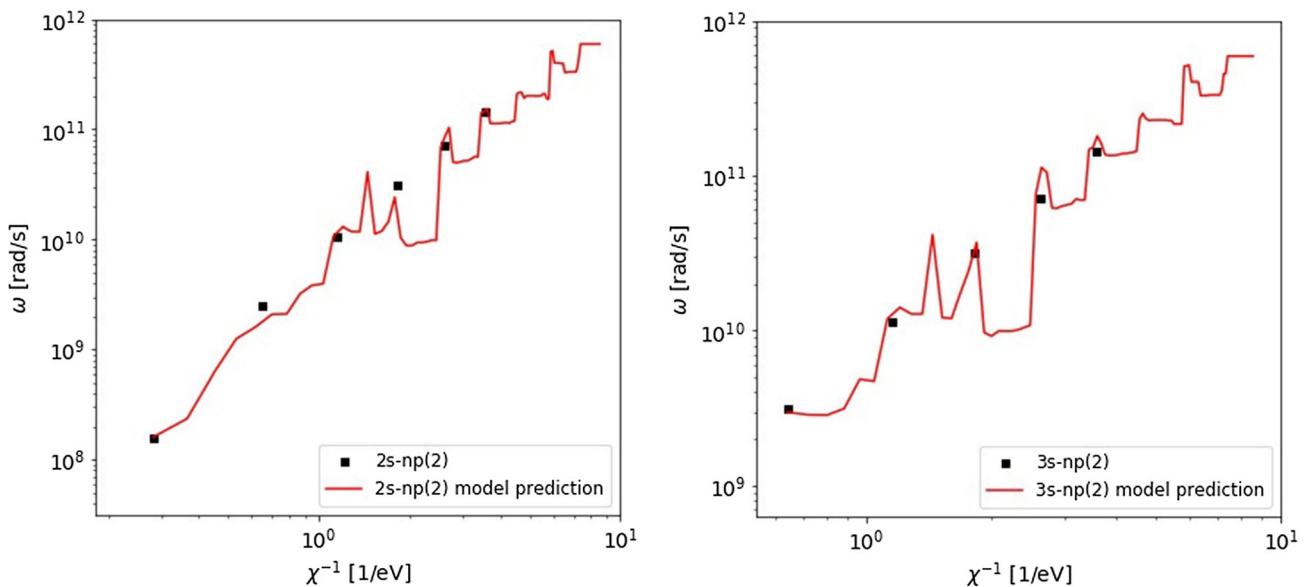


Fig. 1 Stark widths regularities within 2s-np i 3s-np spectral series of Li I ($T = 30,000$ K, $N_e = 10^{20} \text{ m}^{-3}$)

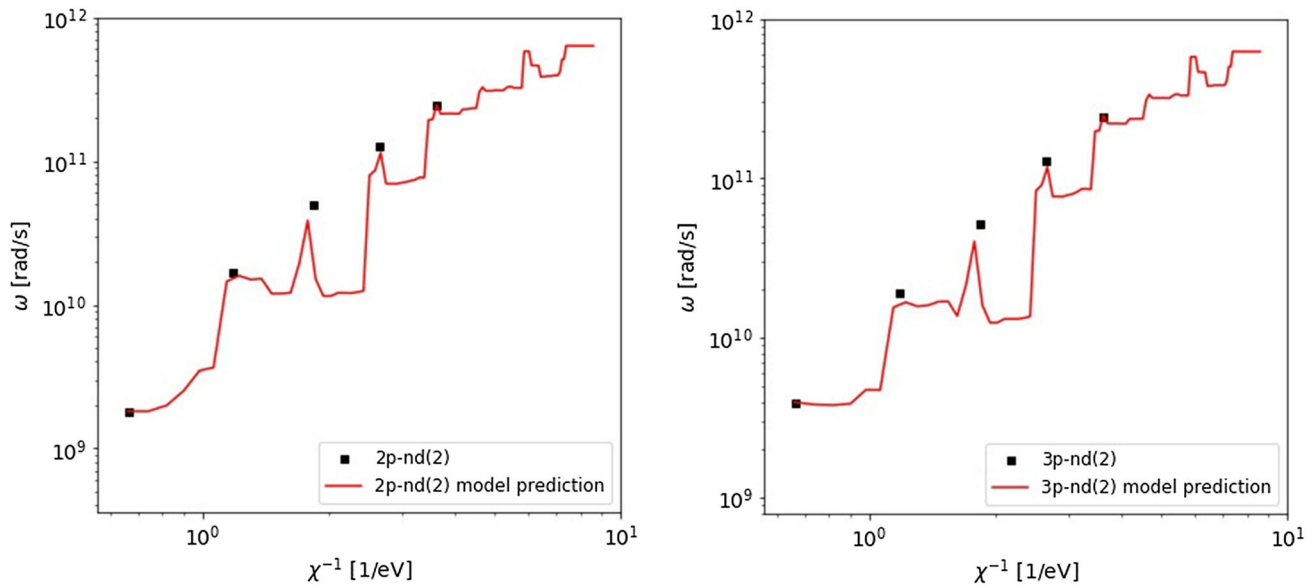


Fig. 2 Stark widths regularities within 2p-nd and 3p-nd spectral series of Li I ($T = 30,000$ K, $N_e = 10^{20} \text{ m}^{-3}$)

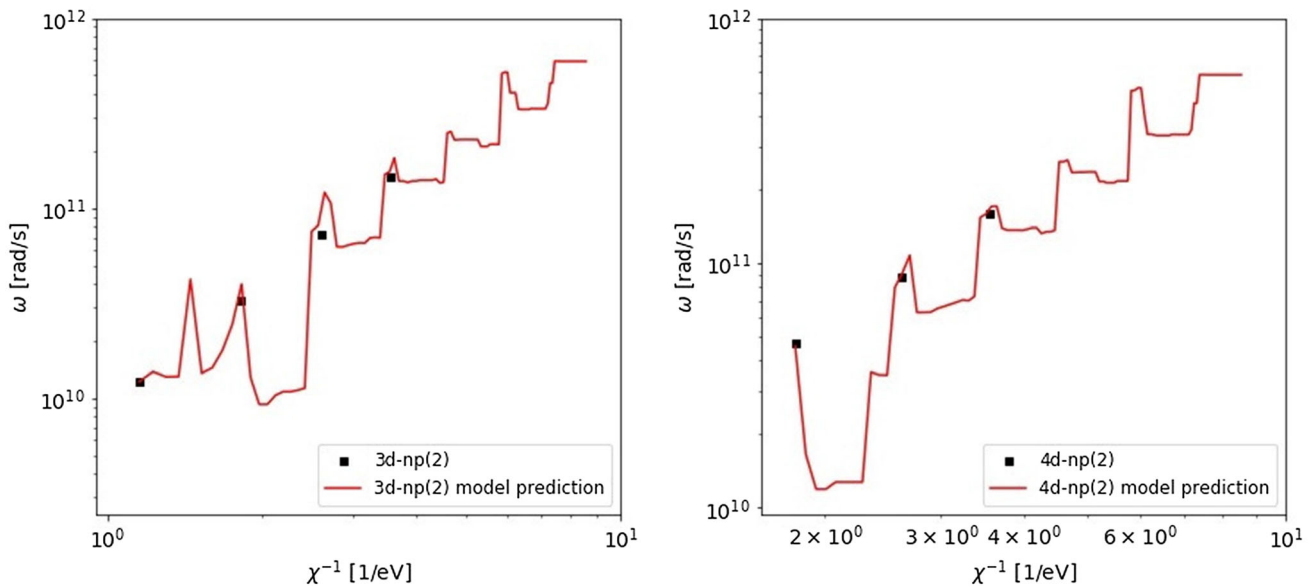


Fig. 3 Stark widths regularities within 3d-np and 4d-np spectral series of Li I ($T = 30,000$ K, $N_e = 10^{20} \text{ m}^{-3}$)

GridSearchCV algorithm finished. We have taken the parameters that the algorithm used to score that particular R^2 . As a result, we got that the best R^2 value was for Random Forest Regressor having $R^2 = 0.95$ for $n_{\text{estimators}} = 100$. The results of other model is given in table 2.

So, our winning model after performing hyper parameter tuning using GridSearchCV was Random Forest Regressor with number of estimators set to 100. Random Forest is a learning method that operates by constructing a large number of decision trees during the training process [5]. It is simple to use and shows high performance for a wide variety of tasks, making it one of the most popular ML

algorithms in different sciences. Random forests are an effective tool in predicting new data, in our case new atomic parameters. It should be emphasized that Breimans paper [5] is cited more about 30,000 times (Web of Science: 36.234, CrossRef: 27.683). In order to check overfitting of the winning model, we did R^2 score check of the model on both training and test datasets. Training R^2 score was 0.98, and test score was $R^2 = 0.95$, so we were sure our model is not overfitting the data.

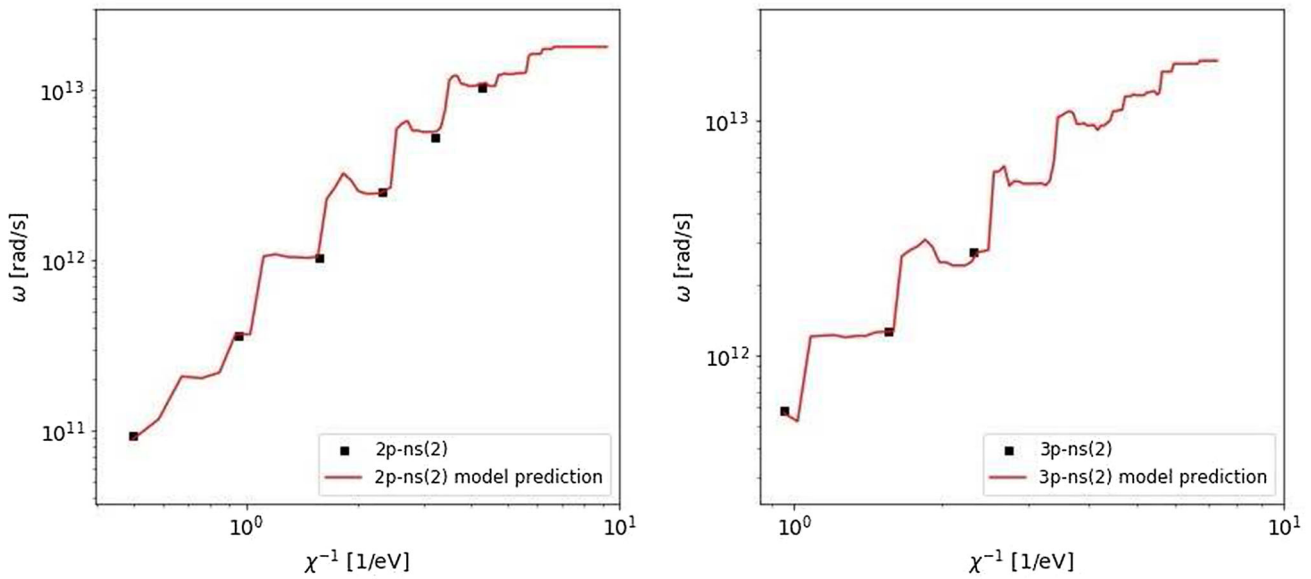


Fig. 4 Stark widths regularities within 2p-ns and 3p-ns spectral series of Li I ($T = 30,000\text{ K}$, $N_e = 10^{22}\text{ m}^{-3}$)

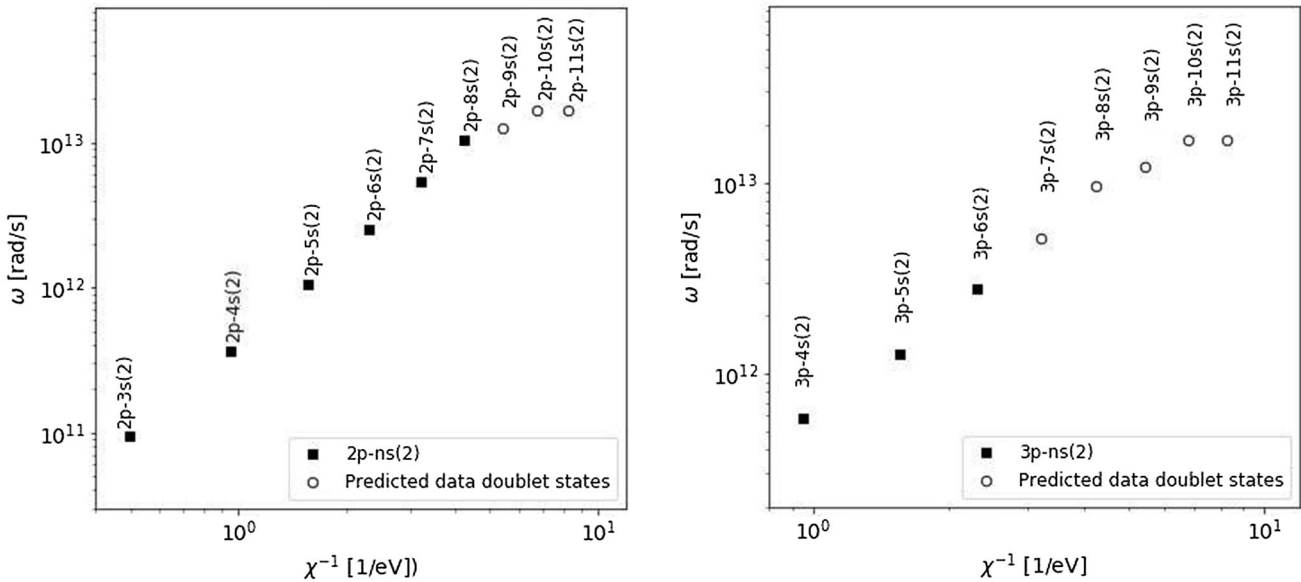


Fig. 5 Stark widths predictions for 2p-ns and 3p-ns spectral series of Li I ($T = 30,000\text{ K}$, $N_e = 10^{22}\text{ m}^{-3}$)

5 Results

The Random Forest model is used to calculate Stark broadening data for spectral series within neutral lithium Li I. Calculated stark widths (red lines) for transitions within analyzed series are represented with existing known values of Stark widths data at the same graphs.

Figure 1 shows the dependence of the Stark width (ω) on the reciprocal value of the electron binding energy at the upper level of the transition (χ^{-1}) for 2s-np and 3s-np transitions within lithium atom at a temperature of $T = 30,000\text{ K}$ and electron concentration $N_e = 10^{20}\text{ m}^{-3}$.

Figures 2 and 3 show the change in Stark width under the same conditions (temperature $T = 30,000\text{ K}$ and electron concentration $N_e = 10^{20}\text{ m}^{-3}$), but for 2p-nd and 3p-nd transitions, as well as 3d-np and 4d-np. A very good description of the atomic structure of lithium, i.e., the values of atomic parameters, can be observed. Interestingly, points 2s-2p and 2p-3d were omitted in our previous analysis [15], while the ML algorithm includes them in the overall analysis and gives excellent agreement with the Stark width value.

Of special importance is the possibility of obtaining the value of stark widths at higher energy levels, for which

these data are not quantitatively calculated. Figure 4 shows the change of Stark widths for the 2p-ns and 3p-ns transitions at a temperature of $T = 30,000$ K and electronic concentration $N_e = 10^{22} \text{ m}^{-3}$. In Fig. 5, the conditions are the same, but the initial values of the Stark width and the values obtained by the ML algorithm are given for higher energy levels of lithium atom. A slight saturation of the values of Stark parameters at higher energy levels can be observed.

The functional dependence obtained using the ML algorithm describes the quantum structure of the energy levels of lithium atoms. From the model lines (red lines), it can be concluded that the model successfully (within the error) indicates the quantum nature of atomic transitions and that other results do not make physical sense, but only jumps.

6 Conclusion

Analysis of spectral data on Stark broadening for 53 different emitters and 34973 lines by ML algorithms was done with more success than it was previously done by classical methods of data analysis. Random forest has scored an average of $R^2 = 0.95$ which makes it an excellent choice for Stark broadening calculations. The correlation parameter obtained by AI is slightly better than the one obtained by classical methods of Stark broadening analysis, but the scope of application is much wider. AI conclusions are applicable to any physical system while conclusions made by classical analysis are applicable only to a small portion of these systems, mostly to ions with low ionization stage. This improves the quality of predictions and enhance a broader usability of results. In fact, these results can be used for any transition and any environment without any restrictions. ML algorithms successfully identified quantum nature by analyzing Stark broadening parameters which can not be done with similar analyses that used classical methods and obtained linear correlation. The biggest issue of the classical analysis is infinite spectral line broadening for high ionization stages and it was successfully resolved by AI with a saturation tendency.

The process of calculating the values of Stark widths, which is used in science for a number of problems in various physical conditions in spectroscopic diagnostics of laboratory plasma, as well as astrophysical and fusion plasma, is significantly accelerated and facilitated with new method based on ML and proposed in the present paper. Using our new proposed model, Stark databases can be significantly improved. For example, Stark broadening calculations can be made for some spectral transitions within W, Ti, Mo and Zr atoms, which are common in

nuclear fusion diagnostics and of interest for spectral analysis in fusion physics [39], as titanium, molybdenum and zirconium are used as alloying materials for tungsten [11, 50]. Lines of Ti are used for astrophysics diagnostics, too [36]. Despite their significance, there is a very big lack of Stark data for these atoms and their ions. There is a lot of missing energy data for higher energy levels for W, Ti, Mo and Zr atoms and their ions. For example, there is no precise value of energy for 6p level for Ti II, so there is no calculated Stark data for transition for which this level is the closest perturbing level. Although very rich in data, NIST database does not have energy values data for all possible excited states of atoms. With standard known methods for Stark width calculation, it is not possible to calculate Stark widths for levels for which energy values of the closest perturbing levels are missing, but ML algorithms enable calculation in these situations, too. In next step, ML predictions and analytic calculations will be compared and ML technique will be used for atomic parameters analyses. Special attention will be paid to spectral lines that are important for fusion and astrophysical research.

Funding The Funding was provided by Ministarstvo Prosvete, Nauke i Tehnološkog Razvoja. This work is financially supported by the Ministry of Education, Science and Technological Development of the Republic of Serbia.

Declarations

Conflict of interest The authors declare that they have no conflict of interest.

References

1. Abbott BP, Abbott R, Abbott TD, Abernathy MR, Acernese F, Ackley K, Adams C et al (2016) Observation of gravitational waves from a binary black hole merger. *Phys Rev Lett* 116:061102
2. Balabin RM, Lomakina EI (2009) Neural network approach to quantum-chemistry data: accurate prediction of density functional theory energies. *J Chem Phys* 131:074104
3. Ball NM, Brunner RJ (2010) Data mining and machine learning in astronomy. *Int J Mod Phys* 19(7):1049–1106
4. Bharti K, Haug T, Vedral V, Kwek LC (2020) Machine learning meets quantum foundations: a brief survey. *AVS Quantum Sci* 2:034101
5. Breiman L (2001) Random Forests. *Mach Learn* 45:5–32
6. Carleo G, Cirac I, Cranmer K, Daudet L, Schuld M, Tishby N, Vogt-Maranto L, Zdeborova L (2019) Machine learning and the physical sciences. *Rev Mod Phys* 91:045002
7. Cao X, Liu H, Chen N (1997) Classification of Cm I energy levels using PCA-BPN and PCA-NLM. *Chem Phys* 220:289–297
8. Carleo G, Troyer M (2017) Solving the quantum many-body problem with artificial neural networks. *Science* 355:602–606

9. Cova TFGG, Pais AACC (2019) Deep learning for deep chemistry: optimizing the prediction of chemical patterns. *Front Chem* 7:809
10. Carrasquilla J, Melko RG (2017) Machine learning phases of matter. *Nat Phys* 13:431–434
11. Cui Z, Zhang X, Liu Q, Li H, Liu Y, Liu H, Wang X, Huang J, Liu H, Cheng J, Li M (2020) A first-principles study of the mechanical and thermodynamic properties of WTi, WV, WZr, WVTi, WVZr alloys. *Fusion Eng Design* 152:111451
12. Deringer VL, Caro MA, Csanyi G (2019) Machine learning interatomic potentials as emerging tools for materials science. *Adv Mater* 1902765:1–16
13. Dimitrijević MS, Konjević N (1980) Stark widths of doubly- and triply-ionized atom lines. *JQSRT* 24:451
14. Dojčinović IP, Tapalaga I, Purić J (2012) Stark parameter regularities of neutral helium lines within different spectral series. *Mon Not R Astron Soc* 419(1):904–912
15. Dojčinović IP, Tapalaga I, Purić J (2013) Stark-width regularities of neutral lithium lines within different spectral series. *Mon Not R Astron Soc* 429(3):2400–2406
16. Dojčinović IP, Trklja N, Tapalaga I, Purić J (2019) Investigation of Stark line broadening within spectral series of potassium and copper isoelectronic sequences. *Mon Not R Astron Soc* 489(3):2997–3002
17. Dunjko V, Wittek P (2020) A non-review of quantum machine learning: trends and explorations. *Quantum Views* 4:32
18. Gastegger M, Behler J, Marquetand P (2017) Machine learning molecular dynamics for the simulation of infrared spectra. *Chem Sci* 8:6924–6935
19. Gavezzotti A (2012) Computational studies of crystal structure and bonding. *Top Curr Chem* 315:1–32
20. Griem HR, Baranger M, Kolb AC, Oertel G (1962) Stark Broadening of Neutral Helium Lines in a Plasma. *Phys Rev* 125:177
21. Griem HR (1968) Semiempirical Formulas for the Electron-Impact Widths and Shifts of Isolated Ion Lines in Plasmas. *Phys Rev* 165:258
22. Griem HR (1974) Spectral line broadening by plasmas. Academic Press, New York
23. Harney C, Pirandola S, Ferraro A, Paternostro M (2020) Entanglement classification via neural network quantum states. *New J Phys* 22:045001
24. Hartmann MJ, Carleo G (2019) Neural-network approach to dissipative quantum many-body dynamics. *Phys Rev Lett* 122:250502
25. Hezaveh YD, Levasseur LP, Marshall PJ (2017) Fast automated analysis of strong gravitational lenses with convolutional neural networks. *Nature* 548:555–557
26. Huerta EA, Allen G, Andreoni I, Antelis JM, Bachelet E, Beriman GB, Bianco FB et al (2019) Enabling real-time multimessenger astrophysics discoveries with deep learning. *Nat Rev Phys* 1:600–608
27. Ishida EEO, Beck R, González-Gaitán S, de Souza RS, Krone-Martins A, Barrett JW, Kennamer N et al (2019) Optimizing spectroscopic follow-up strategies for supernova photometric classification with active learning. *Mon Not R Astron Soc* 483:2–18
28. Iten R, Metger T, Wilming H, del Rio L, Renner R (2020) Discovering physical concepts with neural networks. *Phys Rev Lett* 124:010508
29. Janet JP, Chan L, Kulik HJ (2015) Accelerating Chemical discovery with machine learning: simulated evolution of spin crossover complexes with an artificial neural network. *J Phys Chem Lett* 9:1064–1071
30. Jevtić D, Dojčinović IP, Tapalaga I, Purić J (2012) Stark width regularities of neutral potassium lines within different spectral series. *Bull Astr Soc India* 40:151–160
31. Kramida A, Ralchenko Y, Reader J, NIST ASD Team (2019) NIST Atomic Spectra Database (version 5.7.1), [Online]. Available: <https://physics.nist.gov/asd> [Tue Mar 24 (2020) National Institute of Standards and Technology, Gaithersburg, MD
32. Krenn M, Gu X, Zeilinger A (2017) Quantum experiments and graphs: Multiparty states as coherent superpositions of perfect matchings. *Phys Rev Lett* 119:240403
33. Krenn M, Malik M, Fickler R, Lapkiewicz R, Zeilinger A (2016) Automated search for new quantum experiments. *Phys Rev Lett* 116:090405
34. Krief M, Feigel A, Gazit D (2016) Line broadening and the solar opacity problem. *Astrophys J* 824(2):98
35. Luchnikov IA, Vintskevich SV, Grigoriev DA, Filippov SN (2020) Machine learning non-Markovian quantum dynamics. *Phys Rev Lett* 124:140502
36. Manrique J, Aguilera JA, Aragon C (2016) Experimental Stark widths and shifts of Ti II spectral lines. *Mon Not R Astron Soc* 462(2):1501–1507
37. Mehta P, Bukov M, Wanga CH, Day AGR, Richardson C, Fisher CK, Schwab DJ, colleagues, (2019) A high-bias, low-variance introduction to Machine Learning for physicists. *Phys Rep* 810:1–124
38. Melnikov AA, Nautrup HP, Krenn M, Dunjko V, Tiersch M, Zeilinger A, Briegel HJ (2018) Active learning machine learns to create new quantum experiments. *Proc Natl Acad Sci USA* 115(6):1221–1226
39. Miškovičová J, Anuš M, van der Meiden H, Veis P (2020) Selection of molybdenum lines by quantitative analysis of molybdenum-zirconium-titanium alloy by CF-LIBS for future fusion applications. *Fusion Eng Des* 153:111488
40. Osterheld AL, Morgan WL, Larsen JT, Young BKF, Goldstein WH (1994) Analysis of spectra from laser produced plasmas using a neural network. *Phys Rev Lett* 73(11):1505–1508
41. Peterson KL (1991) Classification of Cm II and Pu I energy levels using counterpropagation neural networks. *Phys Rev A* 44:126–138
42. Purić J, Šćepanović M (1999) General regularities of stark parameters for ion lines. *Astrophys J* 521:490
43. Purja Pun GP, Batra R, Ramprasad R, Mishin Y (2019) Physically informed artificial neural networks for atomistic modeling of materials. *Nat Commun* 10:2339
44. Reis I, Baron D, Shahaf S (2019) Probabilistic random forest: a machine learning algorithm for noisy data sets. *Astronom J* 157(16):1–12
45. Reis I, Poznanski D, Baron D, Zasowski G, Shahaf S (2018) Detecting outliers and learning complex structures with large spectroscopic surveys - a case study with APOGEE stars. *Mon Not R Astron Soc* 476:2117–2136
46. Rohde DJ, Drinkwater MJ, Gallagher MR, Downs T, Doyle MT (2005) Applying machine learning to catalogue matching in astrophysics. *Mon Not R Astron Soc* 360:69–75
47. Sahal-Bréchet S (1969) Impact theory of the broadening and shift of spectral lines due to electrons and ions in a plasma. *Astron Astrophys* 1:91
48. Sahal-Bréchet S, Dimitrijević MS, Moreau N (2020) STARK-B database. [online]. Available: <http://stark-b.obspm.fr> [February 20, 2020]. Observatory of Paris, LERMA and Astronomical Observatory of Belgrade
49. Sarma SD, Deng DL, Duan LM (2019) Machine learning meets quantum physics. *Phys Today* 72(3):48–54
50. Snead LL, Hoelzer DT, Rieth M, Nemith AA (2019) Refractory Alloys: Vanadium, Niobium, Molybdenum, Tungsten. *Struct*

- Alloys for Nucl En App 585–640, Chapter 13. <https://www.sciencedirect.com/science/article/pii/B9780123970466000137>
51. Tapalaga I, Dojčinović IP, Purić J (2011) Stark width regularities within magnesium spectral series. *Mon Not R Astron Soc* 415:503
 52. Tapalaga I, Dojčinović IP, Milosavljević MK, Purić J (2012) Stark Width Regularities within Neutral Calcium Spectral Series. *PASA* 29:20
 53. Tapalaga I, Trklja N, Dojčinović IP, Purić J (2018) Stark width regularities within spectral series of the lithium isoelectronic sequence. *Mon Not R Astron Soc* 474:5479
 54. Torlai G, Mazzola G, Carrasquilla J, Troyer M, Melko R, Carleo G (2018) Neural-network quantum state tomography. *Nat Phys* 14:447
 55. Trklja N, Tapalaga I, Dojčinović IP, Purić J (2018) Stark widths regularities within spectral series of sodium isoelectronic sequence. *New Astr* 59:54
 56. Trklja N, Tapalaga I, Dojčinović IP, Purić J (2019) Stark Widths Regularities Within: ns-np, np-ns, np-nd, nd-np and nd-nf Spectral Series of Potassium Isoelectronic Sequence. *Atoms* 7(4):99
 57. Wei W, Huerta EA (2020) Gravitational wave denoising of binary black hole mergers with deep learning. *Phys Lett B* 800:135081
 58. Westerhout T, Astrakhantsev N, Tikhonov KS, Katsnelson MI, Bagrov AA (2020) Generalization properties of neural network approximations to frustrated magnet ground states. *Nat Commun* 11:1593
 59. Wu J, Shen L, Yang W (2017) Internal force corrections with machine learning for quantum mechanics/molecular mechanics simulations. *J Chem Phys* 147:161732
 60. Zhang P, Shen L, Yang W (2019) Solvation free energy calculations with quantum mechanics / molecular mechanics and machine learning models. *Phys Chem B* 123(4):901–908

Publisher's Note Springer Nature remains neutral with regard to jurisdictional claims in published maps and institutional affiliations.

The usage of perceptron, feed and deep feed forward artificial neural networks on the spectroscopy data: astrophysical & fusion plasmas

N.M. Sakan , I. Traparić, V.A. Srećković  and M. Ivković

*Institute of Physics Belgrade, University of Belgrade, Pregrevica 118, 11080
Belgrade, Serbia (E-mail: nsakan@ipb.ac.rs)*

Received: July 28, 2022; Accepted: October 1, 2022

Abstract. Artificial neural networks are gaining a momentum for solving complex problems in all sorts of data analysis and classification matters. As such, idea of determining their usability on complex plasma came up. The choice for the input data for the analysis is a set of stellar spectral data. It consists of complex composition plasma under vast variety of conditions, dependent on type of star, measured with calibrated standardized procedures and equipment. The results of the analysis has shown that even a simple type of perceptron artificial neural network could lead to results of acceptable quality for the analysis of spectra of complex composition. The analyzed ANNs performed good on a limited data set. The results can be interpreted as a figure of merit for further development of complex neural networks in various applications e.g. in astrophysical and fusion plasmas.

Key words: Atomic processes–Line: profiles–astrophysical & fusion plasmas

1. Introduction

The usage of machine learning algorithms is a growing field of research (D’Isanto et al., 2016; Baron, 2019; Kates-Harbeck et al., 2019). Since the computer power is constantly growing its usage is often found in a wide variety of applications: from determination of objects on a photograph all the way to expert systems capable to determine adequate states and predicted outcomes of complex systems; from difficult-to-maintain machines states and prediction of conditions, up to the assistance in human health monitoring.

Even the specific fields of spectroscopy rely deeply on artificial neural networks, as is the case for instance with medical spectroscopy application Wang et al. (2015), or for instance agricultural application Basile et al. (2022); Longin et al. (2019). The material recognition in extraterrestrial spectroscopic probing is also a very difficult task, since the limitations of the mass and resolving power of the onboard instruments are a very difficult limiting factor (Koujelev et al., 2010; Bornstein et al., 2005).

Usage of the artificial neural networks (ANN) fell into focus of our interest because of flexibility of their application, as well as a variety of complex problems that they have already solved.

All of the mentioned has been a factor for applying neural networks to the decision process of determining a stellar spectral type as an example of application on astrophysical data (Albert et al., 2020). Artificial neural networks are often used in astrophysics (e.g. for the integral field spectral analysis of galaxies in Hampton et al. 2017). There is an expectation of development of further focus on convolutional neural networks application on spectroscopic data (Castorena et al., 2021). Also, even more complex predictions based on back-propagation in neural networks as well as complex artificial neural networks structures in spectroscopic usage are known (Li et al., 2017). In order to have insight of applicability of the ANN usage we have limited our research on simplest case as a figure of merit.

Few random spectral curves from database Pickles (1998) are presented here in results. Entire database set consists of spectra for 12 types of stars, spectral type O normal; B normal; A normal; F normal; F Metal rich; F metal weak; G normal; G Metal rich; G metal weak; K normal; K Metal rich; K metal weak; and M normal. Our aim was to create test case as a method of determining a quality of specific ANN in various machine learning analysis, from stellar and fusion spectra analysis, material analysis, up to extremely specific cases as enhancing a low resolution instrument performance for specific applications (Marinković et al., 2019; Albert et al., 2020).

2. ANN basics and principles

The usage of systems related to the functions of neural networks has been in focus of investigation since mid-1940 McCulloch & Pitts (1943), but the real usage has evolved with the application of modern day digital computers, which enabled construction of networks of enlarged complexity. One of the simplest neural networks, that could be seen more as a test case of validity of operation of artificial intelligence systems, is perceptron (Rosenblatt, 1958). The prediction as well as sensitivity of the training data set is in favor of more complex networks. It is the primary goal of our investigation, along with their application on spectral data sets and measurements.

The choice for the dataset was made on open access data files for the 131 stellar spectra published by Pickles (1998) (available at accompanying reference appended to the bibliographical entry, as seen in May 2022). The results are promising and further research on the field is expected. The quality of the trained artificial neural network prediction is related to the data set as well as its structure. An effort of applying it on a large scale dataset or database should be carried out.

The problem of finding out a category of data subset is an inherent problem for any sort of machine learning and as such for the artificial neural networks also. The artificial neural network is a system of mathematical functions trying to resemble a simplified animal brain. The network consists of artificial neurons.

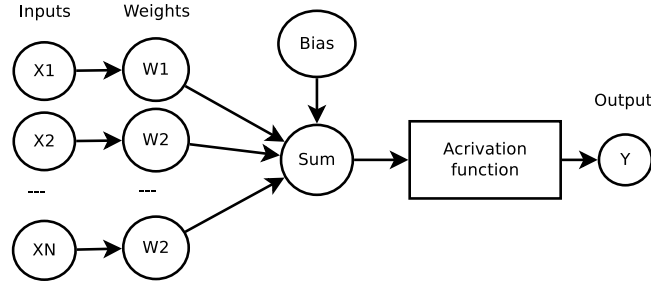


Figure 1. The concept of a neuron. Schematic presentation.

A neuron is described as a function that adopts output value based on its input values and bias value by the means of reaction function. The simplest neuron concept could be seen on a Figure 1. The neuron determines its output state as an output of activation function based on a weighted sum of input values and a bias value itself, and could be described by equation

$$y_{out} = f_{act} \left(Bias + \sum_{i=1}^N x_i w_i \right), \quad (1)$$

where f_{act} is a activation function, x_i and w_i are the i -th input value as well as adequate input weight.

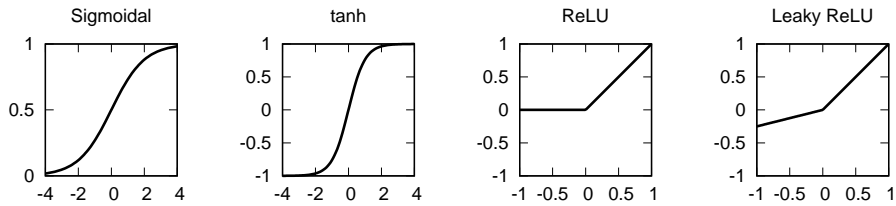


Figure 2. Four most common neuron reaction functions.

The neuron reaction on external stimulus is strongly dependent on its reaction function. In order to determine the neuron behavior on a micro scale, the reaction function as well as the method of adopting the weight values plays a determining role. Four most common reaction functions are shown on Figure 2.

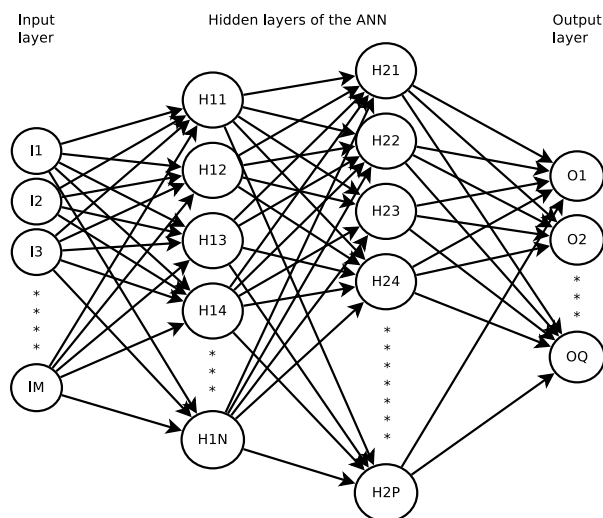


Figure 3. Concept of ANN of perceptron, feed forward and deep feed forward. The shown ANN consists of M input neurons, two hidden layers of N and P neurons and output layer of Q neurons.

A topology of the neural network as well as the learning method are determining the global reaction of the neural network. For the goal of usability analysis the simplest ANN topologies, perceptron, is chosen. The Feed Forward and Deep Feed Forward topologies are based upon fully connected dense layers of neurons, see Figure 3. The two specific layers, input and output, have the dimensionality of the input data and output states consequently and are the only limiting factors of the network. When there is more than one hidden layer, the neural network is considered to be the deep one.

3. Results and discussion

In Figure 4 several random spectral curves from database Pickles (1998) are presented. Entire dataset consists of spectra for 12 types of stars, spectral type O normal; B normal; A normal; F normal; F Metal rich; F metal weak; G normal; G Metal rich; G metal weak; K normal; K Metal rich; K metal weak; and M normal. Each epoch of the dataset was divided into 70% for training set and 30% for the test set.

As a test bench for the application of the ANN to the selection set of perceptron, Feed Forward and Deep Feed Forward networks are used. As a reaction function ReLU (rectified linear unit) was used, and the input data was normalized to unit using standardization

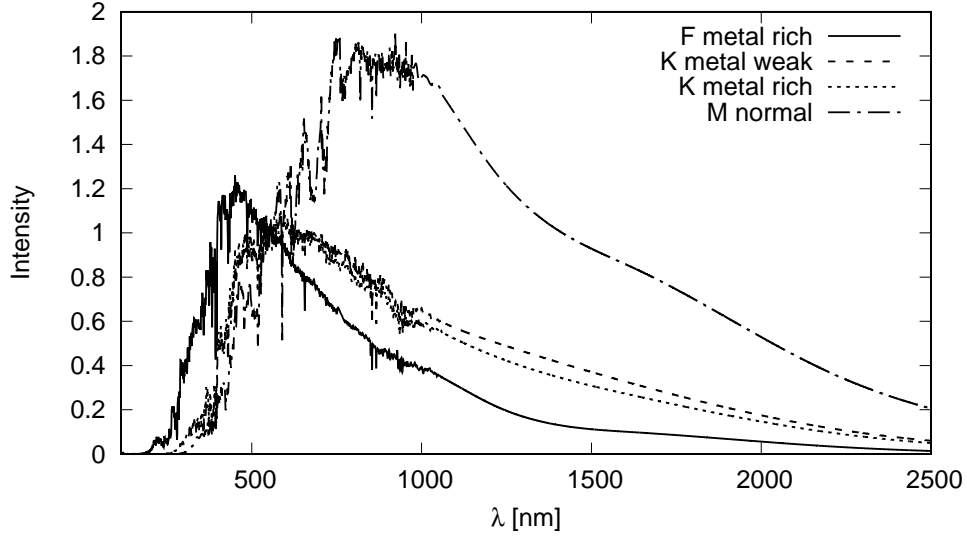


Figure 4. Several sample spectra. Spectra i.e. data is taken from [Pickles \(1998\)](#).

$$x' = \frac{x - \mu}{\sigma}, \quad \hat{\mu} = \frac{1}{N} \sum_{i=1}^N x_i, \quad \hat{\sigma} = \sqrt{\frac{1}{N-1} \sum_{i=1}^N (x_i - \hat{\mu})^2}. \quad (2)$$

No additional data preparation was imposed. The investigated neural network topologies were let to train on the set of data for 200 epochs. Input layer consisted of 4771 input values of available data, output layer consisted of 12 types of stars, spectral type O normal; B normal; A normal; F normal; F Metal rich; F metal weak; G normal; G Metal rich; G metal weak; K normal; K Metal rich; K metal weak; and M normal. The hidden layers consisted of 5000 neurons in first, 1000 in second and 512 neurons in third layer. They were included consequently in order to compare ANN behavior, see Figure 5.

It is obvious, by the analysis of calculated data presented in Figure 5, that the deeper ANNs are capable to learn faster and have better predictions after smaller epochs of learning. This capability is a winning solution in the case of complex spectra. The ANN could fall into pseudo stable states and produce a non-minimal error. Such falls into local minimum state could be avoided by several advanced methods one of which is providing an algorithm for forgetting of the learned state, e.g. algorithm that disturbs a learned state after each application.

Also, there are probably better methods for the input dataset preparation, from pure mathematical procedures up to convolutional ANN (CNN) incorporation. It is proven that, even in its simplest forms, ANN could be used for such

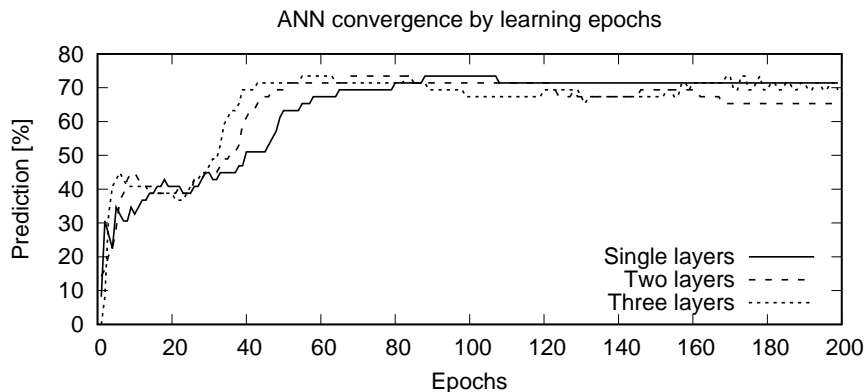


Figure 5. Convergence of ANN of perceptron, feed forward and deep feed forward, on analyzed dataset.

tasks. It is to expect that there are better ANN topologies for such a task, and this is a field for further investigation.

From the above it is obvious that even in its crudest form artificial neural networks are capable to successfully deal with the spectra classification. It is confirmed that this case could be used as a figure of merit for the further development of ANN and machine learning applications in general.

4. Conclusions and future possibilities

The results are promising and the further research on the field is expected. The first goal of analysis of a single set of complex spectral data recorded under similar conditions is achieved with reasonably good prediction. Concerning minute differences in comparison to each other it is considerable result for the basic ANN structure.

Since the quality of the trained artificial neural network prediction is related to its structure as well as the dataset quality and volume, an effort on a large-scale database collection should be carried out. One of the first steps should be inclusion of pre-trained convolutional ANN for the purpose of input data pre-processing before entering of selector ANN.

Commercial packages as well as some specific open-source solutions for the analysis of the spectra with the help of predefined ANN exist. Their application is usually very specific and does not allow the opportunity to fit the best ANN nor to perform unique mathematical procedures during input data preparation that could be best suited for the sought purpose. This possibility is the winning factor in each specific case. Such approach should enable systems for more specialized problem solutions, from stellar and fusion spectra analysis up to more

specific expert systems related to technical solutions. The further development in both ANN structures as well as data preparation should be carried out with the specified problem in mind.


Acknowledgements. The research was funded by the Ministry of Education, Science and Technological Development of the Republic of Serbia, Contract: 451-03-68/2022-14/200024 and supported by the Science Fund of the Republic Serbia, Grant no. 3108/2021.

References

- Albert, D., Antony, B. K., Ba, Y. A., et al., A Decade with VAMDC: Results and Ambitions. 2020, *Atoms*, **8**, 76, DOI: 10.3390/atoms8040076
- Baron, D., Machine Learning in Astronomy: a practical overview. 2019, *arXiv e-prints*, arXiv:1904.07248
- Basile, T., Marsico, A. D., & Perniola, R., Use of Artificial Neural Networks and NIR Spectroscopy for Non-Destructive Grape Texture Prediction. 2022, *Foods*, **11**, DOI: 10.3390/foods11030281
- Bornstein, B., Castano, R., Gilmore, M., Merrill, M., & Greenwood, J., Creation and testing of an artificial neural network based carbonate detector for Mars rovers. 2005, in *2005 IEEE Aerospace Conference*, 378–384
- Castorena, J., Oyen, D., Ollila, A., Legett, C., & Lanza, N., Deep spectral CNN for laser induced breakdown spectroscopy. 2021, *Spectrochimica Acta Part B: Atomic Spectroscopy*, **178**, 106125, DOI: <https://doi.org/10.1016/j.sab.2021.106125>
- D’Isanto, A., Cavuoti, S., Brescia, M., et al., An analysis of feature relevance in the classification of astronomical transients with machine learning methods. 2016, *Monthly Notices of the RAS*, **457**, 3119, DOI: 10.1093/mnras/stw157
- Hampton, E. J., Medling, A. M., Groves, B., et al., Using an artificial neural network to classify multicomponent emission lines with integral field spectroscopy from SAMI and S7. 2017, *Monthly Notices of the Royal Astronomical Society*, **470**, 3395, DOI: 10.1093/mnras/stx1413
- Kates-Harbeck, J., Svyatkovskiy, A., & Tang, W., Predicting disruptive instabilities in controlled fusion plasmas through deep learning. 2019, *Nature*, **568**, 526, DOI: 10.1038/s41586-019-1116-4
- Koujelev, A., Sabsabi, M., Motto-Ros, V., Laville, S., & Lui, S., Laser-induced breakdown spectroscopy with artificial neural network processing for material identification. 2010, *Planetary and Space Science*, **58**, 682, DOI: <https://doi.org/10.1016/j.pss.2009.06.022>, exploring other worlds by exploring our own: The role of terrestrial analogue studies in planetary exploration
- Li, Z., Zhang, X., Mohua, G. A., & Karanassios, V., Artificial Neural Networks (ANNs) for Spectral Interference Correction Using a Large-Size Spectrometer and ANN-Based Deep Learning for a Miniature One. 2017, in *Advanced Applications for Artificial Neural Networks*, ed. A. El-Shahat (Rijeka: IntechOpen)

- Longin, L., Tusek, A. J., Valinger, D., et al., Application of Artificial Neural Networks (ANN) Coupled with Near-InfraRed (NIR) Spectroscopy for Detection of Adulteration in Honey. 2019, *Biodiversity Information Science and Standards*, **3**, e38048, DOI: 10.3897/biss.3.38048
- Marinković, B., Srećković, V., Vujčić, V., et al., BEAMDB and MOLD—Databases at the Serbian Virtual Observatory for Collisional and Radiative Processes. 2019, *Atoms*, **7**, 11, DOI: 10.3390/atoms7010011
- McCulloch, W. S. & Pitts, W., A logical calculus of the ideas immanent in nervous activity. 1943, *The bulletin of mathematical biophysics*, **5**, 115, DOI: 10.1007/BF02478259
- Pickles, A. J., A Stellar Spectral Flux Library: 1150-25000 Å. 1998, *Publications of the ASP*, **110**, 863, DOI: 10.1086/316197
- Rosenblatt, F., The perceptron: A probabilistic model for information storage and organization in the brain. 1958, *Psychological Review*, **65**, 386, DOI: 10.1037/h0042519
- Wang, Q., Zheng, N., Li, Z., & Ma, Z., Quantitative analysis of glucose in whole blood using FT-Raman spectroscopy and artificial neural network. 2015, in *Proceedings of the 2015 International Conference on Computational Science and Engineering* (Atlantis Press), 471–475

New perspectives in the analysis of Stark width regularities and systematic trends

Z. Majlinger^{1,2,3} and I. Traparić⁴ 

¹ *Astronomical Observatory, Volgina 7, 11060 Belgrade, Serbia*

² *ES “I. G. Kovačić”, Kralja Tomislava 18, 51326 Vrbovsko, Croatia*

³ *ES “V. Gortan”, Prilaz Vladimira Gortana 2, 51000 Rijeka, Croatia*

⁴ *Institute of Physics Belgrade, Pregrevica 118, 11080, Belgrade, Serbia*
(E-mail: traparic@ipb.ac.rs)

Received: September 29, 2023; Accepted: October 20, 2023

Abstract. Regularities and systematic trends among the sample of Stark widths obtained by using modified semiempirical method from the STARK-B database were analysed. Two different approaches are independently used – multiple regression method combined with simple cluster analysis, and random forest (RF) machine learning algorithm. Predicted values of Stark widths calculated with estimate formulae obtained from multiple regression method, and those values predicted by using RF algorithm, were compared with already known corresponding experimental Stark widths published elsewhere. Results of this analysis indicate that both of these methods can mostly predict new Stark width values within the acceptable range of accuracy.

Key words: line profile — Stark broadening — atomic data — machine learning

1. Introduction

Stark broadening theory plays the important role in investigation of high temperature dense plasma, where the collisional processes between the charged particles contribute significantly to the spectral line broadening. From technological perspective, Stark widths and shifts of spectral lines in the spectra of neutral atoms and ions are of interest for a number of problems - for example, analysis and modelling of laboratory, laser produced, fusion or technological plasmas, accurate spectroscopic diagnostics and modelling, etc. Applications of Stark broadening theory are also various in research of astrophysical plasma as well - for example, for interpretation, synthesis and analysis of stellar spectral lines, determination of chemical abundances of elements from equivalent widths of absorption lines, opacity calculations, estimation of the radiative transfer through the stellar atmospheres and subphotospheric layers, radiative acceleration considerations, nucleosynthesis research, etc.

Calculation of Stark broadening parameters sometimes can be difficult, and it can take a time, especially if quantum theory is applied. If conditions to apply less accurate but faster quasistatic, unified, semiempirical or semiclassical methods are not satisfied, quick and simple estimates could become important, especially if we do not need a great accuracy, or there is no time for more complicated and more accurate calculations, or if we have a great number of Stark broadening parameters to calculate in very small period of time. This is very common case, for example, if astrophysical spectra are investigated. According to (Wiese, Konjevic, 1982), regularities and systematic trends (RST) can be found among the Stark widths of atomic spectral lines, which can simplify the way of obtaining these estimates. This is especially significant when some atomic data, necessary to perform more accurate Stark broadening methods of calculations, are missing. For example, the lack of atomic data, such as energy levels or transition probabilities is usually noticed in the spectral data for rare-earth elements. Analysis based on RST is mostly the only way to determine Stark widths and shifts in sometimes very complex spectra of these elements, which become more and more important in spectral investigations of hot stars of spectral type A and B, and white dwarfs (Popović, Dimitrijević, 1998).

In this investigation, we focused on searching systematic trends among great amount of Stark widths from STARK-B database (Sahal-Bréchet et al., 2014b, 2015), obtained by modified semiempirical (MSE) method (Dimitrijević, Konjević, 1981) as a continuation of our previous work on determination of unknown MSE Stark widths and studying of RST among the MSE Stark broadening parameters (see, for example, Majlinger et al., 2015, 2017a,b, 2020a). Two different methods are used to analyse the sample – classical statistical regression method, which has already been used many times in previous investigations of regularities and systematic trends, and random forest (RF) algorithm from a group of machine learning methods, which become very popular methods more often used in these days whenever some classification or non-linear regression is needed to be performed. Unlike to previous analyses of RST, here some new atomic parameters, which have not taken into consideration before, are included. We will shortly explain both of these methods and finally discuss and compare the obtained results.

2. Methods

2.1. Simple cluster and multiple regression analysis

Estimates of Stark widths can be divided into three main groups:

- approximations derived from the theory – e.g., Cowley’s formula (Cowley, 1971) or MSE formula (Dimitrijević, Konjević, 1987)
- formulae based on statistical analysis on a large number of existing Stark widths (see e.g. Purić, Šćepanović, 1999; Purić et al., 1978).

- formulae based on systematic trends noticed without statistical analysis on corresponding examples (Wiese, Konjevic, 1982).

Whether it is one type or another, the formula for estimating Stark widths for lines of multiple ionized atoms usually can be expressed as a non-linear function of atomic and plasma parameters:

$$\omega_E = f(\lambda, N_e, T, Z, E_{ion}, E_{upper}, E_{lower}) \quad (1)$$

Sometimes some of these parameters are included in the estimate implicitly, through the effective ionization potential χ_j for level j :

$$\chi_j = E_{ion} - E_j, \quad j = \text{upper, lower} \quad (2)$$

according to Purić, or effective principal quantum number of the upper (n_+) or lower (n_-) level, which has already been used, for example, in MSE theory of Dimitrijević and Konjević (Dimitrijević, Konjević, 1981):

$$n_+^2 = \frac{Z^2 E_H}{\chi_{upper}} \quad (3)$$

$$n_-^2 = \frac{Z^2 E_H}{\chi_{lower}} \quad (4)$$

Here $Z - 1$ is the charge of the ion, ω_E is the estimated Stark width in \AA , λ is the wavelength in \AA , N_e is the perturber density in cm^{-3} , E_H is the energy of the hydrogen atom (or Rydberg constant), E_{ion} is the ionization energy, and E_j is the energy of upper or lower levels in cm^{-1} ($j = \text{upper, lower}$).

Immediately after the first article on Stark broadening (Holtzmark, 1919), simple approximate formulas derived from the theory began to appear. Cowley's formula (Cowley, 1971) is probably the best known among them and it is still commonly used in astrophysics. Cowley (1971) specified three different formulas, one for neutral emitters, one for electrically charged emitters (which humble Cowley contributes to Griem), and one for estimating widths for temperatures close to 10000 K. The authors use different variants of Cowley's formula in addition to the original ones from the article (Cowley, 1971), and the difference is in the neglect or addition of the lower effective principal quantum number as a number and in the values of the numerical constant in the formula (see e.g. Killian et al., 1991; Alwadie et al., 2020).

Jagoš Purić made a great effort in studying RST among the Stark width values. The first works on regularities were published by (Purić, Ćirković, 1973) and (Purić et al., 1978). Purić and his co-workers found the correlation between Stark width and difference between ionization energy and energy of the upper state (what he called the upper effective ionization potential) and a number of experimental and theoretical values of Stark widths, offering a set of different estimation formulae. In the following decades, a number of papers on this topic were published, where different correlation parameters were stated for different transitions, different charges and different homologous and isoelectronic

sequences (see e.g. Miller et al., 1980; Purić et al., 1978, 1993, 1997, 2008). This statistical research is also supported by some other authors (see e.g. Djeniže, 1999; Djeniže et al., 2001), with occasional attempts to generalize this approach for all different transitions, different elements and different charge values (Purić, Šćepanović, 1999; Scepanovic, Puric, 2013). Comparing the great amount of Stark width data from STARK-B database (Sahal-Bréchet et al., 2014b, 2015), Purić offered so-called “generalized” estimate (Purić, Šćepanović, 1999) which should be used, according to the authors, “to calculate Stark line widths of the multiply charged ion of different elements along the periodic table.” These scientific articles evolve over time, so Purić and co-workers later give up searching for a universal formula for all lines and focus their statistical analysis only on individual homologous or isoelectronic series (Dojčinović et al., 2011, 2012, 2013a,b; Tapalaga et al., 2011, 2018; Jevtić et al., 2012; Trklja et al., 2019b,a). However, the possibility to apply all of these estimates to predict new unknown Stark widths should be furtherly discussed (Majlinger et al., 2017a,b, 2020b).

The final purpose of this research was to find new general estimates accurate enough to approximately predict the unknown values of Stark widths. Our assumption is that these new estimates should be related on existing estimates, e.g. Cowley’s from Cowley (1971) and Purić’s from Purić and Šćepanović (1999). However, after investigation of accuracy in prediction of unknown Stark widths by using of these two estimates, in the cases of MSE calculated electron-impact widths for Lu III and Zr IV spectral lines, it was obvious that they don’t offer enough accurate approximation (Majlinger et al., 2017a, 2020b). At least in the case of Zr IV Stark widths, several possible reasons were suggested to explain this discrepancy (Majlinger et al., 2017b):

- numerical coefficients in estimations are not properly adjusted
- some important parameters are neglected in equation (1) but significantly contribute to the result, and
- temperature functions used in previous estimates could be incorrect

According to statistical analysis of Stark widths calculated for 143 transitions from 26 multiply charged ions of 17 elements using the modified semiempirical method, (for example, most of them are elaborated by (Dimitrijević, Konjević, 1981), and previous assumptions, new estimates of Stark widths were found. After providing simple cluster analysis (Aggarwal, V., 2014) and multiple regression analysis (for example Chatterjee, Simonoff, 2014), we concluded that MSE Stark width sample has to be divided in three separate groups:

1. For a type I of transitions: $nl-nl'$, $L = l$, $L' = l'$ (for example, $2s^1S-2p^1P^o$, $3s^3S-3p^3P^o$, $3p^1P^o-3d^1D$, $4s^3S-4p^3P^o$, etc), proper estimate is Cowley-like:

$$\omega_{E1} = 3.438 \cdot 10^{-24} N_e \lambda^2 \frac{n_+^4 + n_-^4}{Z^2(2l_> - 1)^{-\frac{3}{4}}} f(T) \quad (5)$$

2. For a type II of transitions: $nl-n'l'$, $L = l, L' = l'$ (for example, $2p^3P^o-3s^3S$, $4p^2P^o-5d^2D$, $4d^2D-5f^2F^o$, $4d^2D-6f^2F^o$, etc), proper estimate is Purić-like:

$$\omega_{E2} = 0.808 \cdot 10^{-25} N_e \lambda^2 \frac{n_+^6 + n_-^6}{Z^2(2l_{>} - 1)^{-\frac{1}{5}}} f(T) \quad (6)$$

Here $f(T)$ is chosen temperature function (which will be explained later), while $l_{>} = \max(l_{upper}, l_{lower})$, where l_{upper} and l_{lower} are orbital quantum numbers for upper and lower level respectively.

3. For all other types of these simplest transitions (type III), like $nl-nl'$, $L \neq l, L' \neq l'$ and $nl-n'l'$, $L \neq l, L' \neq l'$ (for example, $3s^1P^o-3p^1D$, $3s^4P^o-3p^4P$, $3p^5D^o-3d^5F$, $3d^1F^o-4p^1D$, etc.), a well known general expression, valid also for the first two types, can be used to obtain width for particular lines within a multiplet from an average width as a whole:

$$\omega_{E3} = \left(\frac{\lambda_{E3}}{\lambda_0} \right)^2 \omega_0 \quad (7)$$

where ω_{E3} and ω_0 are estimates of unknown Stark widths and a Stark width obtained with estimates (5) or (6), while λ_{E3} and λ_0 are corresponding wavelengths respectively.

After optimizing the number of parameters in these estimates according to minimum description length properties (see, for example, Grünwald, 2004), and keeping in mind that all models are uncertain, idealizing reality (Wit et al., 2012) and that sample is not equal to population, we rounded exponents in (5) and (6) on the closest integer or rational number, to avoid physically meaningless results (for example, $\lambda^{1.74}$ is replaced with λ^2 , $Z^{1.95}$ with Z^2 , etc.) and to approach enough to probable statistical model ideally concerning about population.

From interpolation of analysed data, new temperature function is suggested:

$$f(T) = \frac{1 - \beta}{\sqrt{T}} + \beta \frac{\ln T}{\sqrt{T}} \quad (8)$$

where β is the linear function of temperature defined as:

$$\beta = AT + B \quad (9)$$

Numerical constants A and B are estimated to be $A = 9.62 \cdot 10^{-7}$ and $B = -4.167 \cdot 10^{-2}$ from the values of lower temperature limit for all considered Stark widths. Lower temperature limit for most of considered Stark widths lies in a range 15000 – 70000 K which corresponds to range of distance between perturbing and perturbed levels used in all considered Stark width calculations around cca 7500 – 38500 cm^{-1} . It is easy to see that relation $0 \leq \beta \leq 1$ is mostly valid for such choice of A and B, and that temperature function approximately

simulates both lower and upper temperature limit conditions when β reach to its limits, which is in a good agreement with some previous analyses of behavior of Stark width values for highest and lowest value of temperature (for example Sahal-Bréchet et al., 2014a).

Correlation between new estimates of full Stark width at half maximum (FWHM) obtained by using relations (5), (6) and (7), and existing MSE values for transition type I, type II and type III with corresponding regression lines are displayed in Figs. 1-3 respectively. To calculate correlation parameters for each estimate, we used the general symbol ω_{EST} instead of ω_{E1} , ω_{E2} , and ω_{E3} . Correlation coefficients corresponding to each estimate WEST are presented in Table 1. In the most idealistic scenario, for log-log regression equation $\log \omega_{EST} = C_1 + C_2 \log \omega_{MSE}$, should be valid $C_1 = 0$, $C_2 = 1$ and therefore $\omega_{EST} = \omega_{MSE}$. As the additional attemption to confirm a validation of this method, predicted Stark widths with estimates from above are compared with corresponding experimental values from references (Konjević et al., 1984, 2002). Result of this comparison is presented in Fig. 4.

Table 1. Correlation parameters for log-log regression equation $\log \omega_{EST} = C_1 + C_2 \log \omega_{MSE}$, between results of estimates (5), (6) and (7) respectively, and MSE values of FWHM Stark widths from analysed sample.

Transition type	C_1	C_2	$ErrC_1$	$ErrC_2$	St. dev.	R_{corr}
I	-1.45E-5	0.9126	0.0325	0.0336	0.13	97.76
II	-.28E-5	1.0266	0.0473	0.0262	0.19	99.32
III	-0.0334	0.84	0.025	0.029	0.064	97.23

2.2. Machine learning methods and RF algorithm

As machine learning represents a very popular tool for different types of problems encountered in science, here it was applied on the study of regularities of Stark broadening. Machine learning model based on Random Forest algorithm was developed and described in detail in reference (Tapalaga et al., 2022), so here it would be briefly described for the sake of completeness. Before developing the model, we needed to develop and create a database for training and testing of the future models. This database was created as a combination of two databases, namely NIST atomic database (Kramida et al., 2022), from which we took atomic parameters of interest for every transition and Stark B database (Sahal-Bréchet et al., 2015) from which we took Stark width and plasma parameters for each calculated width. After the completion of this database, it contained around 53 000 lines. Features selected for this research were: Plasma electron density, electron temperature, atomic number, charge of the emitter, energies of both upper and lower levels, total angular momentum of both upper and lower levels, principal and orbital quantum numbers for initial and final of corresponding transitions.

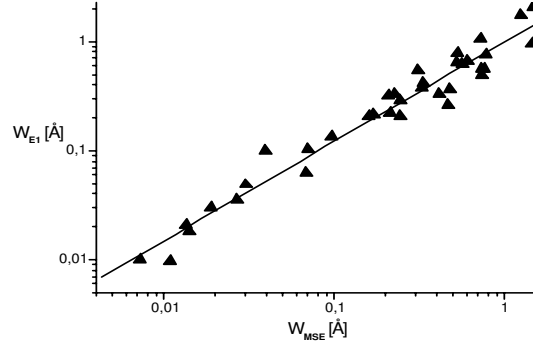


Figure 1. Log-log correlation between FWHM Stark width values obtained by using estimates from multiple regression analysis (ω_{E1}) and MSE values (ω_{MSE}), with corresponding regression line.

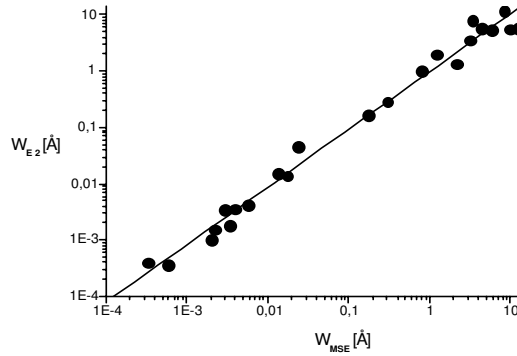


Figure 2. Log-log correlation between FWHM Stark width values obtained by using estimates from multiple regression analysis (ω_{E2}) and MSE values (ω_{MSE}), with corresponding regression line.

Additionally, ionization energy and quantity called upper level effective potential after (Purić, Šćepanović, 1999) were taken into a set of input parameters, which provides a label data comparison. Data outliers were removed as data having higher energy of lower level than upper level. Finally, the analysis was constrained to the following plasma parameters: $N \leq 10^{17} \text{ cm}^{-3}$, $T_e \leq 150\,000 \text{ K}$ and $E_{upper} \leq 500 \text{ eV}$. This restriction left us with around 32 000 available transitions for further analysis. To choose the best model and corresponding parameters, GridSearchCV (Grid Search Cross Validation) technique was applied. Here for every set of model parameters, model is trained and tested on

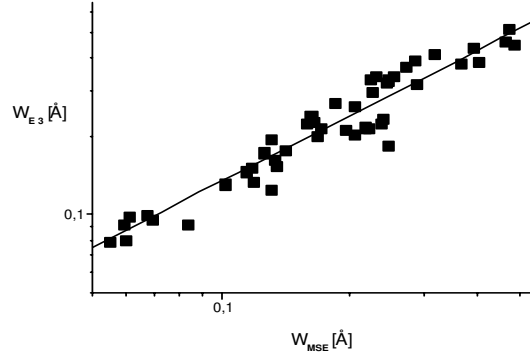


Figure 3. Log-log correlation between FWHM Stark width values obtained by using estimates from multiple regression analysis (ω_{E3}) and MSE values (ω_{MSE}), with corresponding regression line.

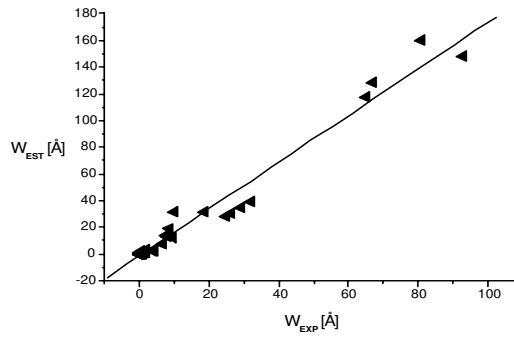


Figure 4. Linear correlation between FWHM Stark width values obtained by using estimates from multiple regression analysis (ω_{EST}) and corresponding experimental values (ω_{EXP}), with corresponding regression line.

given dataset, and best performance is reported. Along with best performance, algorithm reports with which parameters has been obtained. Three models were tested: Decision Tree, Random Forest and Gradient Boosting Regressor. Performances of the model are reported in table 2.

It can be seen that the best results were obtained with Random Forest for the following parameters: maximal depth of the tree equal to 10, minimal samples at one leaf set to 3 and number of estimators equal to 200. As in the case of multiple regression method, Stark widths predicted with using RF algorithm were compared with corresponding experimental widths from the same refer-

Table 2. Comparison of performances for three learning machine models used in analysis.

Model	Parameters	R^2 score
Decision tree	max_depth = 5	0.9
Random Forest	max_depth = 10	0.97
	min_samples_leaf = 3 n_estimators = 200	
Gradient Boosting Regressor	max_depth = 10	0.96
	min_samples_leaf = 2 n_estimators = 200	

ences as before (Konjević et al., 1984, 2002). Results of this comparison are shown in Fig. 5 and Fig. 6. As we can see on figure 5, RF model performs well, except of few points that are estimated badly. Also, from the figure 6 it can be concluded that RF method performs better in visible part than in the ultra violet or infrared part of the spectrum.

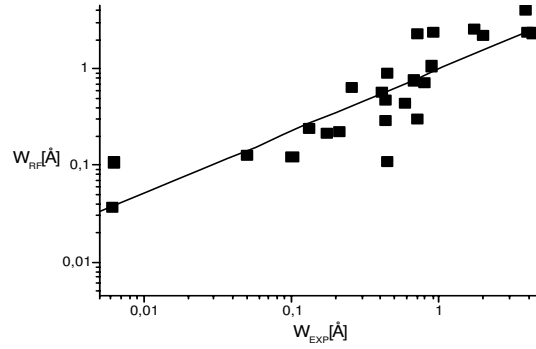


Figure 5. Log-log correlation between FWHM Stark width values obtained by using RF algorithm (w_{RF}) and corresponding experimental values (w_{EXP}), with corresponding regression line.

To improve the model and to test whether we could reduce the number of features in the dataset while keeping the accuracy of the model, permutation importance test was performed. This method permutes each feature randomly within dataset, and calculate the decrease in performance of the already trained model. Greater the decrease, more important is the feature. Results of this analysis are given in table 3.

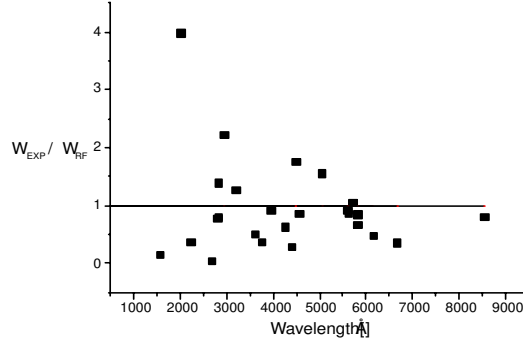


Figure 6. Dependence of ratio between experimental FWHM Stark widths (w_{EXP}) and corresponding values obtained by using RF algorithm (w_{RF}) on wavelength of spectral lines for which Stark widths are calculated.

Table 3. Feature importance test results for RF model.

Feature	Importance score
Electron density N_e	5.9 ± 0.2
Upper - level principal quantum number n_i	3.50 ± 0.12
Charge of emitter q	1.04 ± 0.04
Upper-level effective potential χ	0.37 ± 0.04
Emitter Z	0.31 ± 0.03
Upper-level orbital quantum number l_i	0.19 ± 0.02
Energy of upper level E_{upper}	0.11 ± 0.02
Lower-level principal quantum number n_f	0.11 ± 0.01
Energy of lower level E_{lower}	0.048 ± 0.005
Lower-level orbital quantum number l_f	0.029 ± 0.004
Lower-level total angular momentum quantum number J_{upper}	0.029 ± 0.007
Upper-level total angular momentum quantum number J_{lower}	0.021 ± 0.005
T_e	0.017 ± 0.003
E_i	0.002 ± 0.001

Results in table 3 indicate that electron density is most important feature as expected, while other important features are naturally emitter, its charge, principal and orbital quantum numbers of upper level and upper-level effective potential χ . Other parameters were removed from analysis, as upper level is included in definition of χ , and model was retrained. As expected, model gave very similar results as those reported in this work, which just confirms that model didn't got confused with some redundant data in initial run.

3. Discussion

For Type I, ratios between estimates and MSE values vary between 0.5 and 2.6, for type II between 0.4 and 1.7, and for type III between 0.7 and 2.0. so we can say that accuracy of our estimates according to MSE values are mostly between -50% and $+160\%$. Including predicted accuracy of MSE results, which is $\pm 50\%$, we expect that global accuracy of our estimates, according to statistical sample we used, should lie between $\pm 50\%$ and $\pm 100\%$ e.g. comparable with the old Griem's semiempirical theory (Griem, 1968).

Despite of several exceptions, ratio between most of new calculated estimates and corresponding experimental Stark widths from references (Konjević et al., 1984, 2002), lies between 0.2 and 2 (see Tab. 3), which leads to conclusion that our estimates are usually accurate in a range of $\pm 100\%$, in accordance with our expectations. On the other hand, average value of this ratio for comparison of estimates with experimental Stark widths is 1.38 ± 0.11 , resulting with accuracy in a range between $\pm 30\%$ and $\pm 50\%$, which is even better than theoretically predicted accuracy for modified semiempirical theory by Dimitrijević and Konjević (1981).

Ratios between Stark widths predicted by using RF algorithm and corresponding experimental Stark widths taken from the same references mentioned above (Konjević et al., 1984, 2002), with the exception of two extreme values 0.06 and 4, lie between 0.16 and 2.23, but average ratio of these values is 0.96 ± 0.16 , leading to an accuracy of around $\pm 20\%$, which is much better than accuracy of predicted results obtained by using classical statistical method. To express the accuracy for both methods, as it is usual in statistics, we used arithmetical mean as the average value of analysed data, while the standard deviation is used as a measure of data dispersion. As a final proof that both of presented methods could be valid, in Fig. 7 we presented results obtained from mutual comparison of Stark width values predicted with these two different approaches. Linear regression equation which expresses dependence between Stark widths predicted with RF method ω_{RF} and those predicted by using estimates WEST obtained by using formulae (5), (6) and (7) is found to be $\omega_{RF} = 0.0523 + 1.0563 \omega_{EST}$ with correlation coefficient $R_{CORR} = 91.05\%$. Figure 7 and values of correlation parameters show that both of these two methods are equivalent, e. g. the results of the estimates with RF model and classical multiple regression statistical method are almost the same. Although it is feeded with results obtained by using semiclassical perturbation method (see for example Sahal-Bréchet et al., 2014a), RF algorithm is shown to be a good predictor, despite of a theoretical method used to calculate analysed Stark width data, because it gives results comparable with estimates based on set of calculations obtained by using modified semiempirical method.

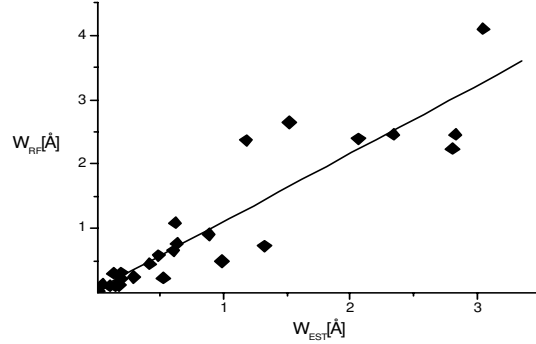


Figure 7. Linear correlation between FWHM Stark width values obtained by using estimates from multiple regression analysis (w_{EST}) and corresponding values obtained by using RF algorithm (w_{RF}), with corresponding regression line.

4. Conclusion

Both of the methods used in this study have some advantages and disadvantages. In general, the advantage of ML models is that they are faster and easier to perform with the proper knowledge of computer programming. On the other hand, any of ML algorithms is some kind of black box, e. g. we finally don't know how input and output parameters are connected. If we want to find out the relationship between Stark width values and atomic and plasma parameters presented in a form of simple formula, we have to continue to investigate regularities and systematic trends of Stark widths using the estimates as, for example, were obtained here (equations (5)-(7)). If we don't need to know this connection, using of some ML algorithm is probably the best solution. Results of predictions using RF model show that, if some general estimate really exists, according to previous vision of Jagoš Purić, it should be the function of 14 variables. In this case, number of input atomic and plasma parameters we used before in a group of equations (1) to find systematic trends among the Stark width value, should be enlarged. We proved that, with additional two parameters (upper and lower orbital quantum number) and considering transition type into analysis, strongly affect on result of estimate, as it is assumed, for example, in (Majlinger et al., 2017b).

However, it is very important to stress that the estimates obtained in this work should be valid under the assumption that they can be applied on simple type of spectra, as they have been analysed in this case (for example, where for all transitions in a whole spectrum parent term remains the same). For more complex spectra, these estimates should be improved, or some other methods are welcome to be used. Furthermore, although RF model shows very strong potential to be applied on RST analysis in future, it is tested only in the sample

of Stark broadening parameters related to simple spectra described here, and in the case of Li I spectral lines (Tapalaga et al., 2022), so it should also be confirmed in a greater sample to make us sure that this method can be applied generally in prediction of new Stark widths despite of complexity of a spectrum we investigate. For the application of these methods to study regularities and systematic trends among the Stark broadening parameters of lines in more complex spectra, additional investigations are needed, and development of both of these method are necessary. Created database used in this and previous study is published online and it is available for use. It can be found on the link <https://github.com/ivantraparic/StarkBroadeningMLApproach>.

Acknowledgements. The research was funded by the Ministry of Science, Technological Development and Inovations of the Republic of Serbia, Contract numbers: 451-03-68/2022-14/200024 and 451-03-68/2022-14/200146. We are very grateful to Milan S. Dimitrijević on useful suggestions and comments during the writing of this paper.

References

- Aggarwal, C., V., R. C. 2014, *Data Clustering* (Taylor and Francis Group)
- Alwadie, N., Almodlej, A., Ben Nessib, N., Dimitrijević, M. 2020, *Contrib. Astron. Obs. Skalnate Pleso*, **50**, 86
- Chatterjee, S., Simonoff, J. S. 2014, *Handbook of Regression Analysis* (John Wiley and Sons)
- Cowley, C. 1971, *The Observatory*, **91**, 139
- Dimitrijević, M., Konjević, N. 1987, *J. Quant. Spectrosc. Radiat. Transfer*, **20**, 223
- Dimitrijević, M. S., Konjević, N. 1981, *Spectral Line Shapes* (Walter de Gruyter and Co.), 211
- Djeniže, S. 1999, *J. Res. Phys.*, **28**, 231
- Djeniže, S., Srećković, A., Kalezić, S. 2001, *Serb. Astron. J.*, **164**, 21
- Dojčinović, I. P., Tapalaga, I., Purić, J. 2011, *Pub. Astron. Soc. Australia*, **28**, 281
- Dojčinović, I. P., Tapalaga, I., Purić, J. 2012, *Mon. Not. R. Astron. Soc.*, **419**, 904
- Dojčinović, I. P., Tapalaga, I., Purić, J. 2013a, *Bull. Astron. Soc. India*, **41**, 281
- Dojčinović, I. P., Tapalaga, I., Purić, J. 2013b, *Mon. Not. R. Astron. Soc.*, **429**, 2400
- Griem, H. R. 1968, *Phys. Rev.*, **165**, 258
- Grünwald, P. D., A tutorial introduction to the minimum description length principle. 2004, *ArXiv*, **math.ST/0406077**
- Holtzmark, J. 1919, *Annalen der Physik*, **363**, 577
- Jevtić, D., Dojčinović, I. P., Tapalaga, I., Purić, J. 2012, *Bull. Astron. Soc. India*, **40**, 151
- Killian, J., Montenbruck, O., Nissen, P. 1991, *Astron. Astrophys. Suppl.*, **88**, 101

- Konjević, N., Dimitrijević, M. S., Wiese, W. L. 1984, *J. Phys. Chem. Ref. Data*, **13**, 649
- Konjević, N., Lessage, A., Fuhr, J. R., Wiese, W. L. 2002, *J. Phys. Chem. Ref. Data*, **31**, 819
- Kramida, A., Ralchenko, Y., Reader, J., NIST ASD Team. 2022, NIST Atomic Spectra Database (version 5.10), <https://physics.nist.gov/asd>, accessed: September 2023
- Majlinger, Z., Dimitrijević, M. S., Srećković, V. A. 2020a, *Mon. Not. R. Astron. Soc.*, **496**, 5584
- Majlinger, Z., Dimitrijević, M. S., Srećković, V. A. 2020b, *Contrib. Astron. Obs. Skalnaté Pleso*, **50**, 164
- Majlinger, Z., Dimitrijević, M. S., Simić, Z. 2017a, *Atoms*, **5**, 49
- Majlinger, Z., Simić, Z., Dimitrijević, M. S. 2015, *Astron. Astrophys.*, **36**, 671
- Majlinger, Z., Simić, Z., Dimitrijević, M. S. 2017b, *Mon. Not. R. Astron. Soc.*, **470**, 1911
- Miller, M. H., Lessage, A., Purić, J. 1980, *Astrophys. J.*, **239**, 410
- Popović, L. C., Dimitrijević, M. S. 1998, *Contrib. Astron. Obs. Skalnaté Pleso*, **27**, 353
- Purić, J., Dimitrijević, M. S., Lakićević, I. S. 1978, *Physics Letters A*, **67**, 189
- Purić, J., Dojčinović, I. P., Nikolić, M., et al. 2008, *Astrophys. J.*, **680**, 803
- Purić, J., Šćepanović, M. 1999, *Astrophys. J.*, **521**, 490
- Purić, J., Šćepanović, M., Milosavljević, V., Ćuk, M., XXIII ICPIG (Toulouse, France). 1997, V – 48
- Purić, J., Ćirković, L., XI ICPIG. 1973, 398
- Purić, J., Miller, H., Lessage, A. 1993, *Astrophys. J.*, **416**, 825
- Sahal-Bréchet, S., Dimitrijević, M., Ben Nessib, N. 2014a, *Atoms*, **2**, 225
- Sahal-Bréchet, S., Dimitrijević, M. S., Moreau, N. 2015, STARK-B database, <http://stark-b.obspm.fr>, accessed: September 2023
- Sahal-Bréchet, S., Dimitrijević, M. S., Moreau, N., Ben Nessib, N., SF2A Conf. 2014b, 515
- Scepanovic, M., Puric, J. 2013, *Rom. Rep. Phys.*, **65**, 1275
- Tapalaga, I., Dojčinović, I. P., Purić, J. 2011, *Mon. Not. R. Astron. Soc.*, **415**, 503
- Tapalaga, I., Dojčinović, I. P., Purić, J. 2018, *Mon. Not. R. Astron. Soc.*, **474**, 5479
- Tapalaga, I., Traparić, I., Trklja Boca, N., et al. 2022, *Neural Comput. Applic.*, **34**, 6349
- Trklja, N., Dojčinović, I. P., Tapalaga, I., Purić, J. 2019a, *Atoms*, **7**, 99
- Trklja, N., Tapalaga, I., Dojčinović, I. P., Purić, J. 2019b, *New Astron.*, **59**, 54
- Wiese, W., Konjevic, N. 1982, *J. Quant. Spectrosc. Radiat. Transfer*, **28**, 185
- Wit, E., van den Heuvel, E., Romeijn, J. 2012, *Statistica Neerlandica*, **66**, 217

VUV SPECTROSCOPY OF THE He II - LYMAN SERIES FOR ELECTRON DENSITY ESTIMATION

I. TRAPARIĆ^{1,2} and M. IVKOVIĆ²

¹*Faculty of Physics, University of Belgrade, Studentski trg 12, Belgrade, Serbia*

²*Institute of Physics, University of Belgrade, Pregrevica 118, Belgrade, Serbia*
E-mail ivke@ipb.ac.rs

Abstract. We report use of the spectral line shapes of the Lyman series of ionized helium for diagnostics of high temperature plasmas. As a light source the low pressure pulsed arc was used. Electron density was determined from width of the He II Paschen alpha line and parameters of the He I 447.1 nm line, while electron temperature was determined from Boltzmann plot of the He II lines. The use of the Inglis-Teller relation on merging of spectral lines along series and on condition for partial local thermodynamic equilibrium was tested as methods for electron density estimation.

1. INTRODUCTION

Vacuum ultra violet, VUV spectroscopy is very important since most intense spectral lines of various elements are in this wavelength region. Special attention was devoted to study of hydrogen and helium lines important for diagnostics of astrophysical and fusion plasmas. Among them, in high temperature plasmas the shape and width of ionized helium Lyman series lines are extensively studied both theoretically, (Kepple, 1971) and experimentally (Wrubel, 2001) and (Mijović, 1989). Since lower members of a series are often highly self-absorbed, in this work methods for plasma diagnostics based on higher member of Lyman series are analyzed.

2. EXPERIMENT

Experimental setup is shown in Figure 1. Plasma source is low pressure pulsed arc, whose inner diameter is 10 mm and distance between electrodes 130 mm. Pressure in the source was set and controlled by needle valve, with the gas flow of 0.2 l/min. One side of plasma source is mounted on VUV spectrometer, and on the other end there is a quartz window. Light emission was obtained by discharging capacitor of Experimental setup is shown in Figure 1. Plasma source is low pressure pulsed arc, whose inner diameter is 10 mm and distance between electrodes 130 mm. Pressure in the source was set and controlled by needle valve, with the gas flow of 0.2 l/min. One side of plasma source is mounted on VUV spectrometer, and on the other end there is a quartz window. Light emission was obtained by discharging capacitor of 5 μ F (previously charged using high voltage supply unit) with ignitron switch BK7703. The discharge

process is controlled via automatic trigger unit. Around the source, Rogowski coil was placed, in order to measure current shape and its value. The radiation from this source is projected 1:1 onto the slit of VIS spectrometer using optical mirrors M1 and M2. Mirror M1 is plane mirror, while M2 is focusing mirror ($f = 2\text{m}$). Visible spectrometer is McPherson 2061 Cherny-Turner type spectrometer, who has the slit widths of $15\ \mu\text{m}$, focal length of $1\ \text{m}$ and grating with $1200\ \text{grooves/mm}$. As light detector we used

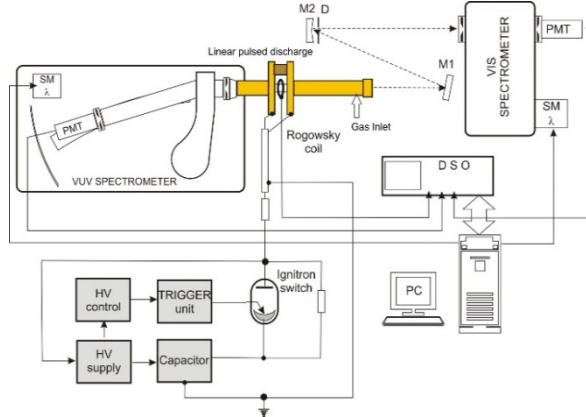


Figure 1: Experimental setup

photomultiplier, PMT mounted on spectrometer exit slit. Wavelength scanning was performed by rotation of diffraction grating with stepper motor, controlled by PC.

As we said above, the other end of plasma source is mounted on VUV spectrometer McPherson 247, which have concave grating of radius $2.2\ \text{m}$ and $600\ \text{grooves/mm}$. Wavelength scanning is performed by moving the exit slit around the Rowland circle with help of stepper motor controlled by the PC. Spectrometer is grazing incidence spectrometer (large incidence angle), so we can observe EUV wavelengths from 0 to around $125\ \text{nm}$.

3. RESULTS AND DISCUSSION

In order to compare results obtained by different methods for electron density determination, N_e was determined from spectral lines recorded in visible spectral range. The N_e in early times of plasma evaluation was determined from full width at half maximum, FWHM of He II Pashen alpha line using formula (Busher et al, 1996):

$$N_e[\text{cm}^{-3}] = 3.58 \cdot 10^{17} \cdot \text{FWHM} [\text{nm}]^{1.204} \quad (1)$$

In plasma decay N_e was determined from separation between forbidden and allowed component of the He I using formula (Ivković et al, 2010):

$$\log_{10}(N_e) = 21.5 + \log_{10} \left(\left(\frac{s}{0.1479} \right)^{b(T_e)} - 1 \right), \quad b(T_e) = 1.46 + \frac{8380}{T_e^{1.2}} \quad (2)$$

using $T_e = 32000 \pm 4000\ \text{K}$ determined from Boltzmann plot of He II Lyman lines, see Figure 2 and 5. The correction of self-absorption using additional mirror was not possible due to window-less operation of the discharge tube, since neither air not MgF_2 window are not transparent for radiation at $30\ \text{nm}$ and below.

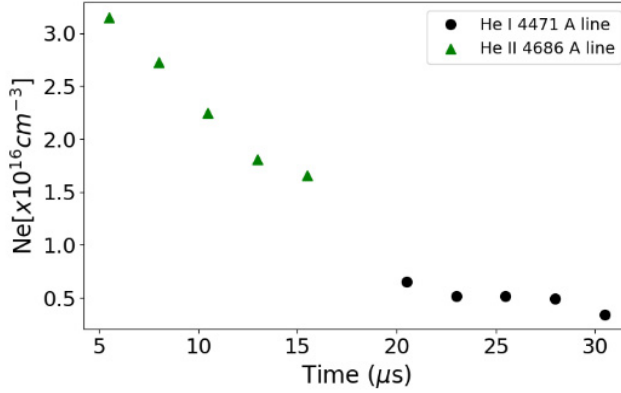


Figure 2: Time dependence of the electron densities in He at 3 mbar and 7 kV

Shapes of the He II lines belonging to the Lyman series were recorded using VUV spectrometer. Recordings were performed at different He gas pressures and different voltages.

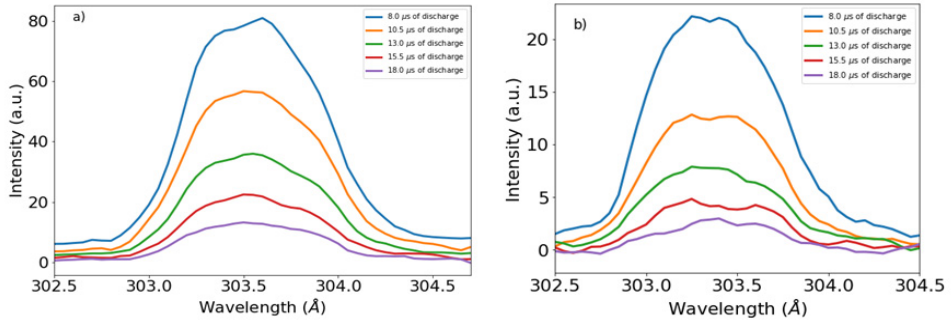


Figure 3: Line shapes of the He II Lyman alpha line at He gas pressure of 3 mbar at discharge voltages V of : a) 7 kV and b) 6 kV

It can be seen that He II Lyman alpha line at 30.2 nm is self-absorbed and becomes even self-reversed, see Figure 3.

Therefore, additional methods based on the recordings of higher members of the He II Lyman series shape for N_e determination were tested. First method is based on relation, see (Inglis-Teller, 1939), between N_e and principal quantum number of the upper level of the last resolved line in series n_{max} :

$$\log_{10}(N_i + N_e [cm^{-3}]) = 23.26 - 7.5n_{max} + 4.5 \log_{10} Z \quad (3)$$

The second one is based on determination of n for which partial local thermo-dynamic equilibrium-PLTE criteria, see (Griem, 1963) was satisfied:

$$N_e(\text{cm}^{-3}) \geq 7.4 \cdot 10^{18} \frac{Z}{n^{17/2}} \sqrt{\frac{k_B T_e}{E_H}} \quad (4)$$

Here Z is the nuclear emitter charge, E_H is the hydrogen atom ionization energy and T_e is electron temperature.

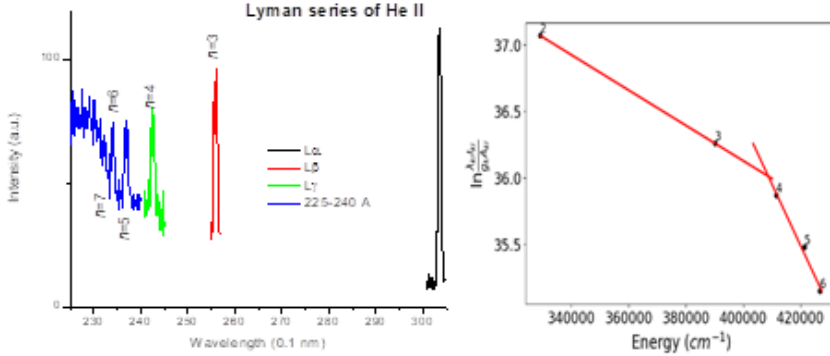


Figure 4. He II Lyman series lines at He gas pressure of 3 mbar at $V = 7\text{kV}$
Spectra recorded (left) and Boltzmann plot (right)

In order to estimate the range of application and accuracy of these methods N_e calculated by these two methods for $T_e = 32\ 000\ \text{K}$ is presented in Table 1. It can be seen that both methods can be used only for $N_e < 10^{16}\ \text{cm}^{-3}$.

Table 1: N_e determined by relation (3) – IT and (4) – PLTE for $T_e = 32\ 000\ \text{K}$

n	2	3	4	5	6	7	8	9
N_e IT	5.02	2.4	2.77	5.2	1.32	4.17	1.53	6.34
[cm-3]	E20	E19	E18	E17	E17	E16	E16	E15
N_e PLTE	2.94	9.35	8.11	1.22	2.58	6.97	2.24	8.23
[cm-3]	E17	E15	E14	E14	E13	E12	E12	E11

It should be stressed that for He gas pressure of 3 mbar, discharge voltage 7 kV the N_e determined from He II P_α line is 3.15, from IT relation between 1.53 and 4.17 and from PLTE criteria using $n = 3.8$, see (Konjević et al, 2009) is 0.13 times $10^{16}\ \text{cm}^{-3}$. Increasing accuracy of IT method by using envelopes i.e. curves through min and max of series lines proposed by (Vidal, 1966) is under development.

References

- Busher S., Glenzer S. and Kunze H.J., 1996, *J.Phys. B, At.Mol.Opt.Phys.* **29**, 4107
 Griem H. R., 1963: *Phys. Rev.* **131**, 1170.
 Inglis D. and Teller E., 1939, *Astrophys.J.* **90**, 439.
 Ivković M. et al., 2010: *Spectrochimica Acta B* **65**, 234.
 Kepple P., 1971, *Technical Report University of Maryland* **72-018**.
 Konjević N., Jovičević S., Ivković M., 2009, *Physics of plasmas* **16**, 103501.
 Mijović S., Pantelić D, Konjević N., Popović M.,: 1989, *Fizika*, **21**, 319.
 Vidal C.R., 1966, *JQSRT* **6**, 575.
 Wrubel Th. , Buscher S., Kunze H.-J., Ferri S.,2001, *JQSRT* **71**, 739.

ELEMENTAL ANALYSIS OF AUSTENITIC STEEL BY CALIBRATION-FREE LASER-INDUCED BREAKDOWN SPECTROSCOPY (CF-LIBS)

I. TRAPARIĆ¹, M. JOVANOVIĆ¹, M. KUZMANOVIĆ² and M. IVKOVIĆ¹

¹*Institute of Physics, University of Belgrade, PO Box 68, 11080 Belgrade, Serbia*

²*Faculty of Physical Chemistry, University of Belgrade, Studentski trg 12 - 16, 11158 Belgrade, Serbia.*

E-mail ivke@ipb.ac.rs

Abstract. Diagnostics of the plasma-facing components (PFC) of a fusion reactor is vital for the safe operation of the device. In this paper, the calibration-free (CF) LIBS procedure was used to assess the chemical composition of an ITER-relevant material, an austenitic steel sample. The self-absorption correction of the intensities of the chosen spectral lines was done for each element, using the estimated plasma temperature and the internal reference line. Obtained results suggest that this method could be suitable for the chemical analysis of austenitic steels, but further investigation is needed to quantify its analytical performance fully.

1. INTRODUCTION

The structural materials of fusion reactors are subjected to thermal, mechanical, chemical, and radiation loads. Due to their excellent manufacturability, good mechanical properties, welding ability, and corrosion resistance, austenitic stainless steels were chosen as structural reference material for ITER (P.J. Maziasz and J.T. Busby, 2012). In addition, to diagnose the composition of the deposits on the fusion reactor's first wall, test targets made of austenitic steel (AISI 316 L) were settled at ten positions on the LHD at NIFS in Japan (V. Kh. Alimov et al., 2019). A CF-LIBS analysis of the LIBS 316L(N)-IG (ITER Grade) was conducted to evaluate the applicability of LIBS for the determination of the composition of test targets and deposits at reactor walls.

2. EXPERIMENTAL SETUP

The experimental setup is shown in Figure 1. Target AISI 316L (YUS = Č.45703, DIN = X2CrNiMo17-12-2, EN 1.4404) plates were placed on the PC controllable x-y table. The impulse from Nd:YAG Q-switch laser (Quantel, $\lambda = 532$ nm, energy 55 mJ, pulse duration 6 ns) was focused on a target with a lens whose focal length

Quantitative analysis was done using a calibration-free algorithm proposed by Yang et al. (Yang et al., 2018). As a first step, internal reference lines were selected manually for each plasma species. In the next step, self-absorption (SA) correction of the internal reference line was done using the following formula (Yang et al., 2018):

$$f_{\lambda}^S = f_{\lambda_R}^S (I_{\lambda}^{ki} / I_{\lambda_R}^{mn}) (A_{mn} g_m / A_{ki} g_k) e^{E_k - E_m / k_B T} \quad (1)$$

where f_{λ} and f_{λ_R} are the SA coefficients of the analytical and internal reference line; I_{mn} , A_{mn} , g_m , and I_{ki} , A_{ki} , g_k are the intensity, coefficient of spontaneous emission, and statistical weight of the upper level for reference and analytical line, respectively.

In the third step, Boltzmann plots, constructed using uncorrected intensities of spectral lines for each analyte, were used to determine excitation temperatures. After this, the optimal temperature was searched in the interval (T_{\min} , T_{\max}) using Particle Swarm Optimization (PSO) algorithm. The selection of temperature interval was based on the minimal and maximal estimated temperatures from Boltzmann plots ($T_{\min} = 7477$ K, and $T_{\max} = 18567$ K). Number of particles was set to 20, inertia coefficient was $w = 0.6$, and cognitive and social coefficients were $c_1 = c_2 = 0.5$. The optimal temperature was found to be 7920 K (0.68 eV).

Finally, using equation (2) (Yang et al., 2018) and the optimal temperature found by PSO, we were able to correct the analytical lines for self-absorption:

$$I_{\lambda}^S = (I_{\lambda_R}^{mn} / f_{\lambda_R}) (A_{ki} g_k / A_{mn} g_m) e^{E_m - E_k / k_B T_{opt}} \quad (2)$$

Results of the optimization process are shown in figure 3.

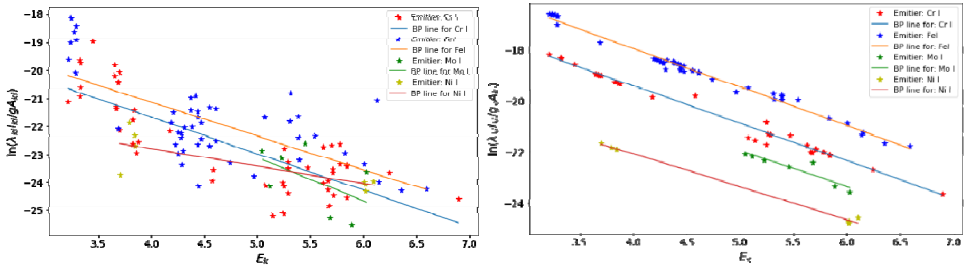


Figure 3. Boltzmann plots before any correction (left) and after all corrections (right).

After all corrections, concentrations of all species were calculated using standard calibration-free procedure (Yang et al., 2018):

$$c_s = \frac{1}{F} U_s(T) e^{q_s} \quad (3)$$

Here, F is the experimental parameter that includes the optical efficiency of the collecting system, $U_s(T)$ is the partition function of given species for temperature T , and q_s is the intercept of the Boltzmann plot.

Parameter F was determined from the following condition:

$$\sum_{s=1}^n c_s = \frac{1}{F} \sum_{s=1}^n U_s(T) e^{q_s} = 1 \quad (4)$$

By applying the described CF model to the experimentally determined intensities of spectral lines, the following elemental composition of the analyzed sample was calculated: Fe - 89.5%, Cr - 8.3 %, Mo - 1.7 %, and Ni - 0.50 %.

4. CONCLUSION

The applied CF model successfully corrected Boltzmann plots for self-absorption, but the obtained concentrations deviate significantly from the expected chemical composition of this type of steel. Careful analysis of the relative spectral intensities of the Fe, Mo, Cr, and Ni lines, considering the measured temperature value, indicates that the declared composition most likely does not correspond to the tested sample. In the next step, an independent chemical analysis of the same sample is planned to confirm the validity of the applied model for the analysis of this type of steels.

Acknowledgements

The research was funded by the Ministry of Education, Science and Technological Development of the Republic of Serbia, Contract numbers: 451-03-68/2022-14/200024 and 451-03-68/2022-14/200146, and supported by the Science Fund of the Republic Serbia, Grant no. 3108/2021.

References

- Maziasz P.J., Busby J.T.: 2012, *Comprehensive Nuclear Materials*, Editor(s): Rudy J.M. Konings, Elsevier.
- Cuicci A., Corsi M., Palleschi V., Rasteli S.: 1999, *Applied Spectroscopy* **53**, 960.
- Alimov V. Kh., Yajima M., Masuzaki S., Tokitani M.; 2019, *Fusion Engineering and Design* **147**, 111228.
- Yang J., Li X., Xu J., and Ma X.: 2018, *Applied Spectroscopy* **72**, 129.

APPLICATION OF ARTIFICIAL NEURAL NETWORK IN THE ANALYSIS OF THE SPECTRA FROM LASER ABLATION COMBINED WITH FAST PULSE DISCHARGE

NENAD M. SAKAN, MILICA L. VINIĆ, VLADIMIR A. SREĆKOVIĆ,
IVAN TRAPARIĆ and MILIVOJE R. IVKOVIĆ

*Institute of Physics Belgrade, University of Belgrade, Pregrevica 118, Belgrade,
Serbia*

E-mail nsakan@ipb.ac.rs

Abstract. The presented work investigates the application of artificial neural networks (ANN) onto spectral classification. The goal of the work was to determine the type of unknown spectra on the basis of a train dataset with the usage of several types of basic ANN. The numerical procedures we are developing, for LIBS analysis of the plasma-facing components of the fusion reactor, was tested on the classification of spectra from different soil or ore types. The data source is a laser ablation combined with fast pulse discharge, the method proposed for the reactor wall analysis. The success in its application has shown not only that the ANN is usable in case of classification of type of spectra but it presents a step forward making of expert system for the more complex equipment.

1. INTRODUCTION

Classification and determination is a common field for the usage of machine learning. The artificial neural networks (ANN) are most powerful machine learning algorithms (Mishra et. al. 2017). As a test case the simplest shallow and deep neural networks has been selected. As a merit a experimental data from laser ablation assisted plasma source for the cases of clay soil and tile brick are used. The goal was to test if the ANN could achieve precision in determining of the appropriate analyzed material as well as type of plasma as an emitter, and as such to prove the usability of ANN method for the fast classification of the recorded spectra. The test dataset was collected with the advanced, laser ablation combined with fast pulse discharge, enhanced LIBS technique (Vinić et al., 2014).

The main contributions of this research work are as follows:

- We compared the applications of the four ANN of different complexities.
- Utilized the ANN of deep type.

In the following section we have described the experimental setup and discussed the results and the future steps.

2. EXPERIMENTAL SETUP

The laser induced breakdown spectroscopy (LIBS) has evolved to a mature technique for the analysis of various samples, from gaseous up to underwater samples. The work has been carried out in order to enhance the emissivity of plasma, the introducing a second pulse, in the case of dual pulse LIBS (DP-LIBS). This technique has made improvement in detection limit and a DP-LIBS is now comparable to other more mature spectroscopy techniques and as such is adopted as a standard spectroscopy technique. The other way of enhancement of the detection limit is fast spark discharge enhanced LIBS, it also has a possibility to excite harder to excite elements such as carbon, chlorine, sulphur and fluorine.

The experimental setup is shown on Figure 1. The investigated material (1.) is irradiated by the 100-mJ nanosecond pulse Moletron model MY-34 Nd-YAG laser (2). The plasma is formed on the sample, as well as inside the fast spark discharge. The radiation is analyzed spectrally as well as temporally with the Andor technology, model Shamrock 303-i spectroscope, coupled with the Andor iStar iCCD camera, model DH 720 -18F-03 (position 3). The time delay for the start of collection a spectral data is determined by the delay unit (4). The electrical behavior of the spark as well as total emissivity is monitored and recorded on the oscilloscope (5). The spark discharge unit consists of capacitor (7), and current probe (8). The photodiode (9) monitors the emissivity of produced plasma.

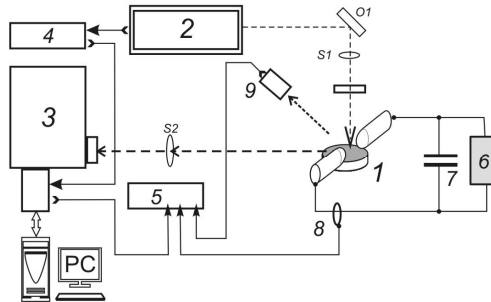


Figure 1: Experimental setup of the system for the laser ablation of the sample material spectroscopy: 1. - investigated material pill, 2. - Nd-YAG laser, 3. - spectroscope with coupled iCCD camera, 4. - delay unit, 5. - oscilloscope, 6. - high voltage supply , 7. - capacitor bank , 8. - current probe.

The set of measurements for clay soil and tile bricks are selected. In the initial time at the delay of 0.1 μs , only the LIBS phase of the plasma is visible, in the later recorded spectra, 0.6 μs delay, the ablated material is inside spark discharge that was triggered by the LIBS phase plasma. So, the four classes of spectra are recorded and used for ANN training, they are denoted here as clay-LIBS, clay-spark, tile-LIBS and tile-spark. For more details on the technique as well as achieved improvement of the signal to noise ratio please consult (Vinić et al., 2014).

3. ANN THEORY AND TOPOLOGY

The artificial neural network application in various areas of spectroscopy is in growth, from environmental applications up to the analysis of LIBS extraterrestrial probes on Mars rover (Sun et al. 2021). In the literature the LIBS spectroscopy as a tool for determining a lead concentration in soil (Zhao et al. 2019) is coupled with ANN. It is a trend in progress for environmental and geophysical analysis (Tingting et al., 2020). Usually, the package of proven machine learning kit is used, for instance Google kit Keras (<https://keras.io/>) is often used in LIBS specific applications (Hao et al., 2020), in this work a Keras implementation of feed forward and deep feed forward ANN was made for the investigation of the usability of ANN presented in this manuscript.

4. RESULTS AND DISCUSSION

The prediction was made on the basis of available experimental data set. The selection was made to throw individual CCD lines of data in order to have artificial dataset enlargement with the different areas of plasma observed as well as different noise composition. The random choice of two thirds of the data was used to train the ANN while the one thirds was used to test the prediction.

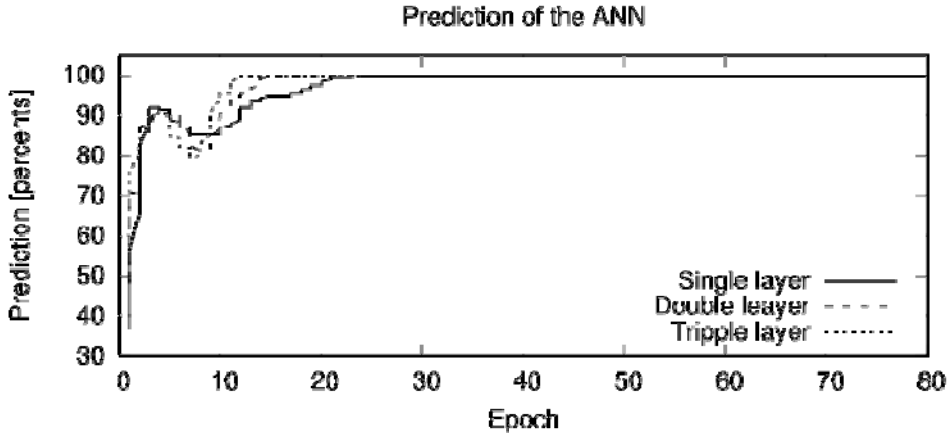


Figure 2: Artificial neural network prediction of the spectra type

The input layer is determined with the dimensionality of input data, so for the available data set the input layer consists of 9927 input neurons. The prediction space consists of four individual outcomes, so the output layer consists of four vectors: $[1\ 0\ 0\ 0]$ – clay-LIBS; $[0\ 1\ 0\ 0]$ – clay-spark; $[0\ 0\ 1\ 0]$ – tile-LIBS; and $[0\ 0\ 0\ 1]$ – tile-spark. The output layer of ANN consists of four neurons belonging to each output vector. Three networks were compared, simplest one consists of only one hidden layer of 15000 neurons, the two layers one with additional 512 neuron second hidden layer, and third one, most complex, consisting of three hidden dense layers of 15000,

1200 and 256 neurons consequently. The output of four consecutive runs was recorded for each of the three investigated ANN. The output outcome was shown on Figure 2. The most complex ANN consist of three hidden dense layers is the one that converged fastest towards the 100% prediction. It could be seen that the process of selection of investigated spectra could be conducted with the help of ANN.

5. CONCLUSIONS AND PERSPECTIVES

From the presented results it is possible to make several conclusions, as first it could be seen that the determination of target type as well as plasma condition, as an emitter could be achieved with ANN successfully. The further conclusion is made by the analysis of the convergence, the more complex, deep ANN, could be more usable for investigation of the further applicability of the method. More over, the third one, is that the sensitivity on the type of emitter, the type of plasma with the ablated material, could lead to more advanced application of inverse methods, to enable prediction of the emitted spectra based on input variables as laser energy, buffer gas, pressure, composition of target and so on.

The paths for the further development, enlarging the data base of the training sets in order of making a more precise determination of the investigated spectra category, the outcome could be enlarged sensitivity on both target material composition as well as plasma conditions. In the case of large training set the interpolation of the known cases is more precise so the inverse problem could be tested. The other result could be more sensitive selection between the spectra that could not be easily dissolved by human eye or the in depth analysis of data could be both time and effort consuming process. Finally, a set of trained ANN could be generated for the in field usage for the specific tasks, e.g. the path towards the production of expert systems.

Acknowledgements

The research was funded by the Ministry of Education, Science and Technological Development of the Republic of Serbia, Contract: 451-03-68/2022-14/200024 and supported by the Science Fund of the Republic Serbia, Grant no. 3108/2021

References

- Chen T., et al. (2020), *TrAC*, **133**, 116113
 Hao Y., et al. (2020), *Sensors*, **20**(5), 1393
 Mishra, C. et. al. (2017), *IAES International Journal of Artificial Intelligence* 6.2 : 66
 Sun C. et al. (2021), *Sci Rep* **11**, 21379
 Vinić M. and Ivković M., (2014), *IEEE Trans. Plasma Sci.*, **42**, no. 10, 2598
 Zhao Y et al. (2019), *Appl. Spectrosc.*, **73**(5), 565

MODELING OF STARK SPECTRAL LINE BROADENING BY MACHINE LEARNING ALGORITHMS

IRINEL TAPALAGA¹, IVAN TRAPARIĆ², NORA TRKLJA BOCA¹,
JAGOŠ PURIĆ¹ and IVAN P. DOJČINOVIĆ¹

¹University of Belgrade, Faculty of Physics, P. O. Box 44, 11000 Belgrade, Serbia

²University of Belgrade, Institute of Physics, Pregrevica 118, 11080 Belgrade, Serbia

E-mail nora@ff.bg.ac.rs

Abstract. Stark broadening caused by free electrons in plasma and its dependence on atomic parameters available in NIST and Stark-b atomic databases has been investigated using a new method based on the machine learning (ML) approach. The correlation parameter obtained by artificial intelligence (AI) is slightly better than the one obtained by classical methods, but the scope of application is much wider. ML algorithms successfully identified quantum nature by analyzing atomic parameters. The biggest issue of classical analysis, which is infinite spectral line broadening for high ionization stages, was resolved by AI with a saturation tendency.

1. INTRODUCTION AND THEORETICAL BACKGROUND

Stark broadening of spectral lines of neutral atoms and ions is used in science for a number of problems in various physical conditions (see Tapalaga et al. 2022). Recent research indicates the importance and usefulness of searching for possible types of regularities in the framework of a Stark broadening investigation. Still, existing tables with calculated and measured Stark widths have a big lack of data. There is a need for Stark widths data in the wide range of chemical elements, plasma temperature and electron densities. In this paper a correlation between Stark broadening and environment parameters, such as the ionization potential of the upper level of the corresponding transition, electron density and temperature, will be investigated using modern ML algorithms. If this method proves to be accurate enough, the process of calculating the value of Stark widths will be significantly accelerated and facilitated.

The general formula for Stark width calculation in the impact approximation (see Griem 1974) is very complicated, it cannot be resolved exactly, so it is useful

to use different approaches in the calculation. The regularity approach which correlates Stark width of spectral line (ω) expressed in [rad/s], electron density (N_e), electron temperature (T_e) and positive value of electron binding energy on the upper level of the transition (χ), expressed in [eV], is given by Puric and Scepanovic 1999. (Eq. 1)

$$\omega = Z_e^k a N_e f(T_e) \chi^{-b} \quad (1)$$

where $Z_e = 1, 2, 3...$ for neutrals, singly charged ions, ... respectively and it represents the rest core charge of the ionized emitter and a, b and k are coefficients independent of electron concentration and ionization potential for a particular transition and the rest core charge of the emitter.

It is expected that spectral series within an isoelectronic sequence show regularity behavior because a wide range of atomic/ionic parameters depend on the electron number. In the last decade we have investigated Stark broadening regularities within spectral series of individual elements, individual isoelectronic sequences and within two spectral series of isoelectronic sequences simultaneously. The present investigation goes one step further and analyses all elements for which there are available data needed for Stark broadening investigation, simultaneously, using machine learning approach. The aim is to find the best possible model which correlates Stark width of spectral line with all available parameters for transition of interest (atomic parameters and environmental parameters).

2. DATASET CREATION AND DATA CLEANING

In order to create dataset, two public repositories connected with atomic spectroscopy are used. First one is Stark B database, see Sahal-Brechot et al. 2020, where the parameters of Stark broadening for different emitters are given. The features taken from this database are: chemical element, ionization stage, upper and lower level of spectral transitions, Stark broadening, the environment temperature and electron density in environment. For analysis purpose, Stark widths expressed in angstroms are converted in radian per second.

To ensure better results we enriched features taken from Stark B database with ones taken from NIST Atomic Spectra database (see Kramida et al. 2019): binding energy of both upper and lower transition levels, ground level energy, total angular momentum quantum number (J) of both upper and lower transition level, as well as principal (n) and orbital (l) quantum numbers and ionization energy. The algorithm for connecting those two databases to form our own works is described below. For every transition connected with certain chemical element, we take the electronic configuration of both upper and lower levels from Stark B database. Then we look for that particular element in NIST database and compare the electronic configurations. If they match, then we take the binding energy of those levels, their

principal quantum number, orbital quantum number and total angular momentum quantum number and finally the ionization energy of that atom. After data cleaning, dataset contains 53 emitters and 34973 spectral lines and follows a normal distribution.

3. MODEL CREATION AND TRAINING

For model creation and training, public Python package Sci-kit learn is used. Four models have been created, every being Pipeline with two steps. In each object of Pipeline class, the first step was data scaling using StandardScaler, and in second step we made our predictions with defined model. Considered models were: Linear Regression, Decision Tree Regressor, Random Forest Regressor and Gradient Boosting Regressor. The dataset was split into training and test dataset using train test split method, leaving 25% of the data for testing. To rank the performance of models, we used best Coefficient of Determination, R^2 , value obtained after GridSearchCV algorithm finished. As a result, we got that the best R^2 value was for Random Forest Regressor having $R^2 = 0.95$ for n estimators = 100. Random Forest is a learning method that operates by constructing a large number of decision trees during the training process, see Tapalaga et al. 2022. It is simple to use and shows high performance for a wide variety of tasks, making it one of the most popular ML algorithms in different sciences. Random forests are an effective tool in predicting new data, in our case new atomic parameters.

4. RESULTS

The Random Forest model is used to calculate Stark broadening data for spectral series within neutral lithium Li I, see Tapalaga et al. 2022. Fig 1. shows the dependence of the Stark width (ω) on the reciprocal value of the electron binding energy at the upper level of the transition (χ^{-1}) for 2s-np and 3s-np transitions within lithium atom. Calculated Stark widths (red lines) for transitions within analyzed series are represented with existing known values of Stark widths data at the same graphs (see Fig. 1). The functional dependence obtained using the ML algorithm describes the quantum structure of the energy levels of lithium atoms. From the model lines (red lines) it can be concluded that the model successfully (within the error) indicates the quantum nature of atomic transitions and that other results do not make physical sense, but only jumps.

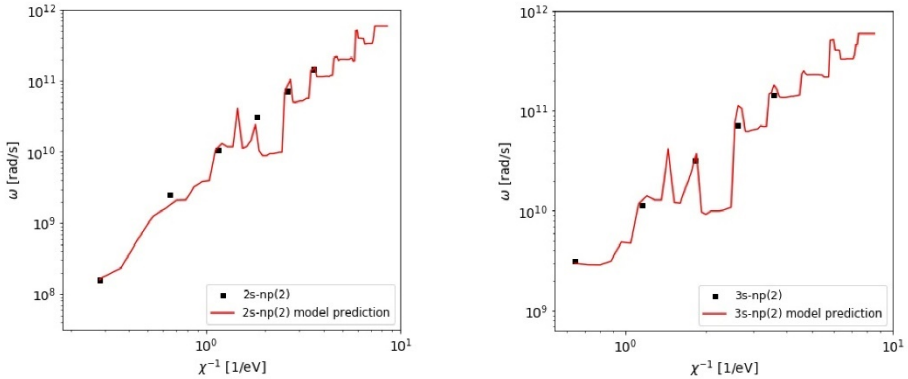


Figure 1: Stark widths regularities within 2s-np and 3s-np spectral series of Li I ($T = 30000 \text{ K}$, $N_e = 10^{20} \text{ m}^{-3}$)

5. CONCLUSION

Analysis of spectral data on Stark broadening for 53 different emitters and 34973 lines by ML algorithms was done with more success than it was previously done by classical methods of data analysis. Random forest has scored an average of $R^2 = 0.95$ which makes it an excellent choice for Stark broadening calculations. With standard known methods for Stark width calculation, it is not possible to calculate Stark widths for levels for which energy values of the closest perturbing levels are missing, but ML algorithms enable calculation in these situations, too.

References

- Griem, H.R. : 1974, *Spectral Line Broadening by Plasmas*, Academic Press, New York
- Kramida A, Ralchenko Yu, Reader J and NIST ASD Team (2019). NIST Atomic Spectra Database (version 5.7.1), [Online]. Available: <https://physics.nist.gov/asd> [Tue Mar 24, 2020]. National Institute of Standards and Technology, Gaithersburg, MD.
- Purić, J., Šćepanović, M. : 1999, *Astrophys. J.*, **521**, 490.
- Sahal-Brechot S., Dimitrijević M. S., Moreau N. (2020) STARK-B database, [online]. Available: <http://stark-b.obspm.fr> [February 20, 2020]. Observatory of Paris, LERMA and Astronomical Observatory of Belgrade
- Tapalaga, I., Traparić, I., Trklja Boca N., Purić, J., Dojčinović, P. I. : 2022, *Neural Computing and Application*, **34**, 6349

TARGET SELECTION FOR LIBS STUDIES OF HYDROGEN ISOTOPE RETENTION

DRAGAN RANKOVIĆ¹ , BILJANA STANKOV² , IVAN TRAPARIĆ² ,
MIROSLAV KUZMANOVIĆ¹  and MILIVOJE IVKOVIĆ^{2*} 

¹Faculty of Physical Chemistry, University of Belgrade, 11158 Belgrade, Serbia

²Institute of Physics, University of Belgrade, Pregrevica 118, 11080 Belgrade, Serbia

*E-mail ivke@ipb.ac.rs,

Abstract. The study of the hydrogen's isotope retention in the first wall of the fusion reactors is the main task in diagnostics of plasma facing components (PFC). Laser Induced Breakdown Spectroscopy (LIBS) enables in-situ PFC diagnostics without any sample preparation making it a most promising technique for this purpose, see H.J. van der Meiden et al, 2021. The basis of this diagnostics is the measurement of the emission of hydrogen isotopes Balmer alpha lines. The most challenging task is the resolving of these lines. Therefore, the first task was the selection and preparation of the targets from which, due to the laser irradiation and consequent plasma formation, hydrogen and deuterium spectral lines will be emitted. Such targets should be substitutes of the hydrogen isotopes enriched components of PFC of future fusion reactors. The main idea was to use the heavy water D₂O embedded in various substrates that are good absorbers of water. For this purpose, following substrates were tested: NaCl - salt, copper sulfate pentahydrate CuSO₄•5H₂O - known as blue vitriol or blue stone, active coal - charcoal, microporous aluminosilicates - zeolites, calcium carbonate CaCO₃ - quicklime, CaSO₄•2H₂O – gypsum. Several forms of graphite were also considered: factory made graphite discs, electrodes with controlled amount of the D₂O on it and spectroscopically pure (or mixed with silica gel) graphite powder, which was doped with water before or after pressing it by hydraulic press. Testing was performed using a 6 ns Q – switched Nd:YAG and TEA CO₂ laser (having 80 ns pulse with 2 μs long tail) in low pressure argon or helium atmosphere. The best results are obtained using gypsum and graphite doped with silica gel, see Traparic et al 2024.

Acknowledgements. The research was funded by the Ministry of Science, Technological Development and Innovations of the Republic of Serbia, Contract numbers: 451-03-68/2022-14/200024 and 451-03-65/2024-03/200146, and supported by the Science Fund of the Republic Serbia, Grant no. 7753287 "NOVA2LIBS4fusion".

References

Van der Meiden, H.J. et al. : 2021, *Nucl. Fusion*. **61** 125001
Traparic, I et al.: 2024, submitted to *Spectrochimica Acta B*

APPLICATION OF MACHINE LEARNING AND ARTIFICIAL INTELLIGENCE IN PLASMA SPECTROSCOPY

IVAN TRAPARIĆ 

Institute of Physics Belgrade, Pregrevica 118, 11080, Serbia
E-mail traparic@ipb.ac.rs

Abstract. Plasma spectroscopy represents the non-contact and non-perturbative plasma diagnostics tool that is widely used. One such application, considered in this work, is the determination of electron density from Stark broadening of emitted spectral lines. The other, laser-induced breakdown spectroscopy (LIBS) is often used for quantitative analysis of sample constitution. Finally, to track impurity transport mechanisms, extreme ultraviolet (EUV) and vacuum ultraviolet (VUV) plasma spectroscopy are used in many fusion devices to monitor highly charged impurity ions. Over the years many approximative formulae and robust models were developed to simulate the shape of emitted spectral lines due to the Stark effect from which line width and shift can be determined. Since a lot of these codes request substantial computational resources, the application of machine learning (ML) for quick estimation of line width was considered (Tapalaga et al. 2022). Usually, the usage of ML in LIBS quantitative analysis is followed by the recording of a large enough database with enough variance in it for precise analysis. Therefore, the usage of an already recorded database for training of the ML model was investigated for additional acceleration of the procedure, and its potential was discussed (Traparic and Ivkovic. 2023). Last but not least, variational autoencoder (VAE) was employed to model the so-called Unresolved Transition Array (UTA) structure, that rises due to the emission from highly charged tungsten ions. The application considered here is the validation of collisional radiative models and estimation of plasma core temperature and electron temperature profile in devices that don't have advanced diagnostics for this purpose.

References

- Tapalaga, I., Traparić, I., Trklja Boca, N. *et al.*: 2022 *Neural Comput & Applic* **34**, 6349–6358
- Traparić, I., Ivković, M. : 2023 *Eur. Phys. J. D* **77**, 30.

DETECTION OF RHENIUM IN TUNGSTEN USING LIBS WITH ADDITIONAL FAST PULSE DISCHARGE

IVAN TRAPARIĆ , BILJANA STANKOV  and MILIVOJE IVKOVIĆ 

Institute of Physics Belgrade, Pregrevica 118, 11080, Belgrade

E-mail traparic@ipb.ac.rs

E-mail biljanas@ipb.ac.rs

Email ivke@ipb.ac.rs

Abstract. The diagnostics of the first wall of future fusion reactors represents a major source of information about the state of the machine and the expected lifetime of the first wall components. As the absorption of neutrons can cause induced radioactivity of the first wall tiles, it is of the essence to monitor the amount of absorbed neutrons. One possibility to monitor them is via nuclear transmutation reaction where tungsten absorbs neutron and create rhenium core [1]. Therefore by assessing the amount of rhenium present in the material, the number of absorbed neutrons can be deduced. In this work Laser Induced Breakdown Spectroscopy (LIBS) combined with fast pulse discharge was used to assess the concentration of rhenium. The main result is the amplification of line intensity and signal to noise ratio compared to the classical LIBS setup at reduced pressure. This results is of particular importance since only small amounts of rhenium are expected to be found, therefore making this approach suitable for this type of diagnostics. Additionally, univariate calibration method based on intensity ratio of W I 488.7 nm and Re I 488.9 nm spectral lines was proposed for determination of rhenium concentrations.

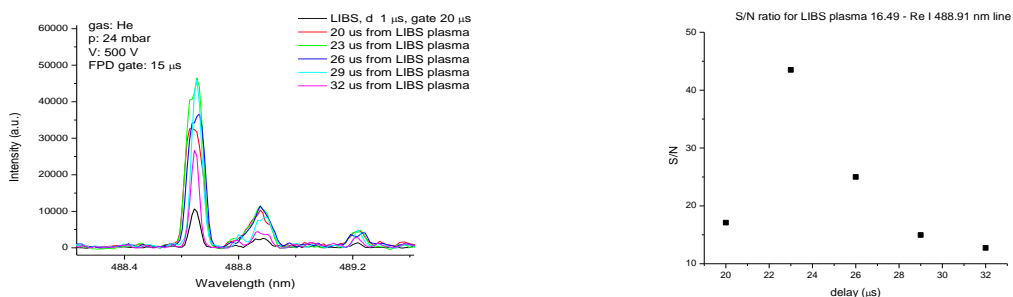


Figure 1: Amplification of Re I 488.9 nm line intensity with FPD (left) and resulting signal to noise ratio (right).

References

Ibano et al, *Journal of Nuclear Materials* **522** (2019) 324-328

INFLUENCE OF THE ABLATION ANGLE CHANGE ON SPECTRAL LINE INTENSITIES IN LIBS EXPERIMENTS

IVAN TRAPARIĆ* , BILJANA STANKOV , NIKOLA VUJADINOVIĆ ,
MILICA VINIĆ  and MILIVOJE IVKOVIĆ 

Institute of Physics Belgrade, Pregrevica 118, 11080, Belgrade

**Corresponding author: traparic@ipb.ac.rs*

Abstract. Laser Induced Breakdown Spectroscopy - LIBS is the most promising technique for the in-situ analysis of the plasma fusion reactor walls, see (Cong Li et al, 2016). The setup which is most frequently used in fusion reactors is so-called remote in-situ RIS LIBS, see (Cai et al, 2019). This configuration uses a scanning system which controls the Mo mirror to direct the laser beam to a different position inside the fusion reactor. In this study, it was investigated how changes in the ablation angles affect the intensity of the emitted spectral lines, considering that the incident beam is not always perpendicular to the PFCs. To this end, the classical LIBS setup at atmospheric pressure was employed. The angle of collection fiber with respect to the laser beam was fixed to 17 degrees. Chosen targets were tungsten-based alloys relevant to fusion research. The spectrum of the plasma was recorded with a Solar MS7504i spectrometer and a fast camera. Results show that there is a non-trivial dependence of the line intensity on the ablation angles, which was attributed to the change of laser focus and ablation surface as the angles were varied both in poloidal and toroidal directions. Additionally, the line intensity correction factor was calculated as the ratio of the intensity for the beam incident at an angle to that of the beam at normal incidence, and it exhibited a complex dependence on both angles.

Acknowledgements

The research was funded by the Ministry of Education, Science and Technological Development of the Republic of Serbia, Contract number: 451-03-68/2022-14/200024, and supported by the Science Fund of the Republic Serbia, Grant no. 7753287.

References

- Cong Li et al.: 2016, Front. Phys. **11**, 114214.
Laizhong Cai et al.: 2019, Rev. Sci. Instrum. **90**, 053503.

STARK BROADENING MODELING WITH ML AND AI ALGORITHMS

I. Traparić

Institute of Physics Belgrade, Pregrevica 118, 11080 Belgrade, Serbia

E-mail: traparic@ipb.ac.ac

During past 20 years many Stark broadening models were developed that can calculate spectral lineshape and estimate a line width that is extensively used in plasma diagnostics of both astrophysical and laboratory plasmas. Some of these calculations yield results relatively fast, some of them need a lot of computational time. Therefore, idea of creating a machine learning (ML) model emerged as a tool for fast estimation of Stark width without need of huge computational time. In our approach, out of three tested models, random forest (RF) algorithm showed the best predictive power after it has been trained, where the coefficient of determination $R^2 = 0.94$ was obtained. Model was trained on a database created by merging parameters from Stark B and NIST atomic databases, it had 14 input parameters that were used to predict final Stark width. Results were compared with experimental ones as well as with SCP theory. We also checked for regularities in Stark effect, and they were also confirmed and in agreement with previous findings.



32nd Summer School and
International Symposium on the Physics
of Ionized Gases

Dr Ivan Traparić

Belgrade, February 19th, 2024

Dear Dr Traparić,

On behalf of the Scientific and Organizing Committees, it is our pleasure to invite you to attend the 32nd *Summer School and International Symposium on the Physics of Ionized Gases* (SPIG 2024) and present a **Progress report**.

The SPIG 2024 will be held from August 26th to 30th, 2024 in Belgrade, Serbia. The details of the conference are available on the official website: <http://spig2024.ipb.ac.rs/>. Please note that due to the limited conference budget, the SPIG 2024 organizers will try to provide partial support to students and early stage researchers, as well as colleagues from economically less privileged countries. Thank you for your understanding and support.

We look forward to welcoming you in Belgrade.

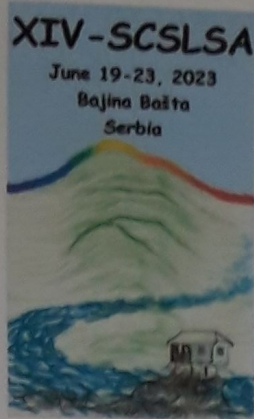
Yours sincerely,

Bratislav Obradović
Miroslav Kuzmanović
(Co-Chair of the Scientific Committee)

(Chair of the Loc. Org. Committee)

Jovan Cvetic
(Co-Chair of the Scientific Committee)

SPIG 2024 Organizers:
University of Belgrade - Faculty of Physical Chemistry
Serbian Academy of Science and Arts



Ivan Traparić
Institute of Physics,
Belgrade, Serbia

**14th Serbian Conference on Spectral Line Shapes in Astrophysics
Bajina Bašta, June 19-23, 2023, Serbia**

23.06.2023.

We certify that Ivan Traparić has presented a progress report "Strak Broadening Modeling with ML and AI algorithms" in the *14th Serbian Conference on Spectral Line Shapes in Astrophysics (14th SCSLSA)*, held in 19-23. June 2023. in Bajina Bašta, Serbia.

Sincerely,

A handwritten signature in black ink, appearing to read 'Luka Č. Popović'.

Luka. Č. Popović
(Chairman of the Scientific Committee)

A handwritten signature in black ink, appearing to read 'Nataša Bon'.

Nataša Bon
(Chairman of the Local Organizing Committee)



Број 0801-1691/1
Датум 08.11.2023

На основу члана 76. Закона о науци и истраживањима ("Службени гласник Републике Србије", број 49/2019), члана 32. Статута Института за физику и захтева који је поднео

ИВАН ТРАПАРИЋ

на редовној седници Научног већа Института за физику одржаној 07.11.2023. године,
донета је

**ОДЛУКА
О СТИЦАЊУ ИСТРАЖИВАЧКОГ ЗВАЊА**

ИВАН ТРАПАРИЋ

стиче истраживачко звање

Истраживач сарадник

ОБРАЗЛОЖЕЊЕ

Иван Трапарић је 08.08.2023. године поднео захтев за избор у истраживачко звање истраживач сарадник. Научно веће Института за физику је на седници одржаној 05.09.2023. године образовало Комисију за спровођење поступка у саставу: др Миливоје Ивковић, научни саветник, Институт за физику у Београду, др Биљана Станков, научни сарадник, Институт за физику у Београду и др Марија Гавриловић Божовић, доцент, Факултет инжењерских наука Универзитета у Крагујевцу. Научно веће је на редовној седници од 07.11.2023. године утврдило да именовани испуњава услове из члана 76. став 2. Закона о науци и истраживањима за избор у звање **истраживач сарадник**, па је одлучило као у изреци ове одлуке.

Одлуку доставити подносиоцу, архиви Института за физику, кадровској служби Института за физику и рачуноводственој служби Института за физику.

Председник Научног већа

ЗА: *Менко Врчић*
др Ненад Лазаревић

Директор Института за физику

Александар Богојевић
др Александар Богојевић





УНИВЕРЗИТЕТ У БЕОГРАДУ
ФИЗИЧКИ ФАКУЛТЕТ

Бр. 470/10

28. 10. 2024

БЕОГРАД СТУДЕНТСКИ ТРГ 12
П ОШТ БН

На основу члана 29 Закона о општем управном поступку («Службени гласник РС» број 18/2016 и 95/2018), и члана 149 Статута Универзитета у Београду - Физичког факултета, по захтеву ИВАНА ТРАПАРИЋА, дипломираног физичара, издаје се следеће

У В Е Р Е Њ Е

ИВАН ТРАПАРИЋ, дипломирани физичар, дана 18. октобра 2024. године, одбранио је докторску дисертацију под називом

"ПРИМЕНА МАШИНСКОГ УЧЕЊА И ВЕШТАЧКЕ ИНТЕЛИГЕНЦИЈЕ У СПЕКТРОСКОПИЈИ ПЛАЗМЕ"

пред Комисијом Универзитета у Београду - Физичког факултета и тиме испунио све услове за промоцију у ДОКТОРА НАУКА – ФИЗИЧКЕ НАУКЕ.

Уверење се издаје на лични захтев, а служи ради регулисања права из радног односа и важи до промоције, односно добијања докторске дипломе.

Уверење је ослобођено плаћања таксе.



ДЕКАН ФИЗИЧКОГ ФАКУЛТЕТА

Проф. др Воја Радовановић

ИНСТИТУТ ЗА ФИЗИКУ

ПРИМЉЕНО: 31-10-2024			
Рад.јед.	б р о ј	Арх.шифра	Прилог
0801-1972/2			

Мишљење руководиоца групе са предлогом чланова комисије за избор у звање научни сарадник – кандидат др Иван Трапарић

Др Иван Трапарић, рођен 14.9.1996. године у Требињу је 18.10.2024. године успешно одбранио своју докторску дисертацију под насловом „Примена машинског учења и вештачке интелигенције у спектроскопији плазме“ на Физичком факултету Универзитета у Београду. Ментори докторске дисертације су били доц. др Маријана Гавриловић Божовић са Факултета инжењерских наука и др Миливоје Ивковић, научни саветник Института за физику у Београду.


Поред тога, др Иван Трапарић је активни учесник пројекта NOVA2LIBS4fusion који се финансира у оквиру позива ИДЕЈЕ Фонда за науку Републике Србије. У Институту за физику је запослен од априла 2021. године прво у звању истраживач приправник, а од новембра 2023. године у звању истраживач сарадник. Током израде докторске дисертације, кандидат је објавио више научних радова у високо рангираним иностраним научним часописима. Из приложеног материјала, кандидат др Иван Трапарић испуњава све услове предвиђене Законом о науци и истраживањима и Правилником о стицању истраживачких и научних звања Министарства науке, технолошког развоја и иновација Републике Србије за избор у звање научни сарадник, те предлажем Научном већу Института за физику у Београду да покрене избор др Ивана Трапарића у поменуто звање.

За чланове комисије предлажем:

1. др Миливоје Ивковић, научни саветник Института за физику у Београду
2. др Биљана Станков, научни сарадник Института за физику у Београду
3. др Мирослав Кузмановић, редовни професор Факултета за физичку хемију Универзитета у Београду

У Београду,

30.10.2024.



др Миливоје Ивковић

Руководилац лабораторије за спектроскопију плазме и ласере